Hole Mobility and Effective Mass in SiGe Heterostructure-Based PMOS Devices

by

Corina E. Tanasa

B.A. Physics & Mathematics
Bard College, 2000

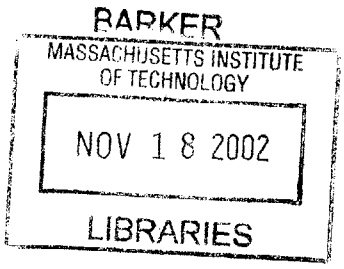

SUBMITTED TO THE DEPARTMENT OF
ELECTRICAL ENGINEERING AND COMPUTER SCIENCE
IN PARTIAL FULFILLMENT OF THE REQUIREMENTS FOR THE
DEGREE OF

MASTER OF SCIENCE
IN ELECTRICAL ENGINEERING AND COMPUTER SCIENCE
AT THE
MASSACHUSETTS INSTITUTE OF TECHNOLOGY

SEPTEMBER 2002

Signature of Author: _____
Department of Electrical Engineering and Computer Science
August 30, 2002

Certified by: _____
Dimitri A. Antoniadis
Professor of Electrical Engineering
Thesis Supervisor

Accepted by: _____
Arthur C. Smith
Professor of Electrical Engineering
Graduate Officer

Hole Mobility and Effective Mass in SiGe Heterostructure-Based PMOS Devices

by

Corina E. Tanasa

Submitted to the Department of Electrical Engineering and Computer Science
on August 30, 2002 in Partial Fulfillment of the
Requirements for the Degree of Master of Science in
Electrical Engineering and Computer Science

ABSTRACT

In this project, a theoretical and experimental study of hole mobility and effective masses was performed to determine the influence of strain on holes in SiGe heterostructure-based PMOS devices.

For that, the hole effective mass and the structure of the valence bands in relaxed silicon-germanium, strained silicon-germanium, and strained silicon under different strain conditions and at different temperatures were determined. The structure of the valence bands directly influences the drift mobility of holes. The effective mass directly influences the carrier concentration.

Also, the inversion mobility of holes in SiGe PMOS devices was measured at low temperatures. Together with the room-temperature mobility data available for these devices, the mechanisms of mobility degradation in strained silicon and strained SiGe layers were studied. Finally, from simulations and experimental mobility data, the values for inversion hole mobility in the individual strained silicon, relaxed SiGe and strained SiGe layers of buried-channel PMOS device were extracted.

Thesis Supervisor: Dimitri A. Antoniadis
Title: Professor of Electrical Engineering

Acknowledgements

I would like to thank my advisor Professor Dimitri Antoniadis, for his thorough guidance and support throughout the course of this project. I would also like to acknowledge and appreciate his superb technical advice and constructive criticism.

I would like to thank and dedicate this thesis to my parents and my sister, for always being there for me and supporting all my decisions, even though this meant me being an ocean away from them.

I would like to thank Indraneel for all his love and moral support throughout the making of this thesis.

Contents

Chapter 1

Introduction

1.1 MOTIVATION

High-performance digital circuits have been based on silicon technology due to the low cost of the material and to properties of silicon and its compounds, properties that have been exploited in a very efficient processing technology. The goal of industry has been to make faster and faster devices, however, the silicon-based MOSFETS are reaching a limit in the speed they can attain, as they are approaching their limit of scalability. To maintain the performance improvement predicted by Moore's Law, one needs to look into additional methods and materials to improve the performance of MOSFET devices, besides what silicon can offer at its best.

SiGe is one of the successful solutions to the silicon crisis. SiGe layer epitaxy is nowadays a well-developed method, which creates high-quality strained and relaxed SiGe layers. The strained SiGe layers exhibit high electron and hole mobilities, and herein lays the potential of SiGe to be incorporated in novel fast MOSFET devices. A plus to the SiGe alloys is that they are silicon-compatible. Their fabrication methods and conditions are similar to those of Silicon.

The fabrication of small-scale SiGe MOSFET is made easy by optimizing the properties of strained and relaxed SiGe layers in large-scale MOSFETS. Such large-scale MOSFETS have been studied in a number of papers, especially from the point of view of

mobility [40],[41],[44], [45], [46]. The electron mobility in SiGe alloys has been thoroughly studied. It is the hole mobility that still needed to be increased to a value proportional to the increase achieved in electron mobility, to make SiGe MOSFETS capable to create CMOS gates. The highest hole mobility values up to date in SiGe MOSFETS ($600cm^2/Vs$, much higher than in silicon MOSFETS) has been obtained by Leitz [40].

1.2 GOALS

This thesis furthers the knowledge of SiGe hole behavior, along two tracks. One track is theoretical, and it studies the valence bands of strained Si and SiGe alloys. The energy structure of the valence-bands determines the drift mobility, as well as the effective mass of the holes, which is an essential component in the intrinsic carrier concentration. In this thesis, I am determining the values for effective mass of holes in strained SiGe alloys versus strain, and in relaxed SiGe alloys. This mass is determined for room and for low temperatures.

The other track is experimental and studies the mobility of inversion holes in SiGe based PMOS at room and low temperatures. The mobility mechanisms in strained Si and strained SiGe are identified and the mobility laws are studied. This is done by using mobility data at room and low temperature, as well as associated simulation results

1.3 OUTLINE

Chapter 2 presents the theory of valence-band structure in SiGe alloys. From the theory, effective masses and energy structures are extracted using the Mathematica simulator.

Chapter 3 presents results for SiGe MOSFETS hole mobility at low temperatures. From low temperature and room temperature data, the mobility dependencies are studied and the mobility of the individual strained layers is determined.

Chapter 4 summarizes the contributions of this thesis.

Appendix A presents data and graphs related to Chapter 2.

Appendix B presents data and graphs related to Chapter 3.

Chapter 2

Band Structure, DOS and Carrier Concentration Mass in SiGe Alloys

2.1 OVERVIEW

The band structure and the density of states effective masses have been studied for unstrained silicon and germanium [2], [3], [5], [10],[12],[13],[26], [28], for strained silicon and germanium only under certain conditions [1], [4], [6], [7], [8], [9],[11],[16], [17],[27], and some strained $Si_{1-x}Ge_x$ alloys on silicon [4], [14], [15]. These studies have been incomplete however, because, for example, the density of states effective mass for holes has not been determined for all valence band energies. Also, carrier concentration masses have not been determined except for unstrained silicon and a few strained $Si_{1-x}Ge_x$ percentages on silicon. The decrease of the carrier concentration mass at low temperatures and the effect on carrier concentration has not been investigated. In this chapter I will be studying the density of states effective masses and the carrier concentration masses of relaxed $Si_{1-x}Ge_x$ and strained $Si_{1-x}Ge_x$ on relaxed $Si_{1-y}Ge_y$, for any percentages x and y of germanium. This study focuses on the hole masses, which are much harder to obtain than electron masses. The temperature dependence of these masses will be thoroughly investigated.

2.2 INTRODUCTION TO DENSITY OF STATES MASSES

The *Density Of States (DOS) Effective Masses* of electrons and holes are important parameters in the evaluation of carrier distribution functions in semiconductors. The intrinsic carrier concentration in a semiconductor is

$$n_i = \sqrt{N_c N_v}\exp(-\frac{E_g}{2k_B T}) \qquad (1)$$

where

E_g is the energy gap of the semiconductor,

$$N_c = 2\left(\frac{2\pi m_{cce} k_B T}{h^2}\right)^{3/2} \qquad (2)$$

$$N_v = 2\left(\frac{2\pi m_{cch} k_B T}{h^2}\right)^{3/2}, \qquad (3)$$

k_B is Boltzmann constant, T is temperature, h is Planck's constant, and m_{cce} and m_{cch} are the carrier density effective masses for electron and holes respectively. These masses are called DOS Effective Masses, but as we will see later, this is a misnomer.

m_{cce} and m_{cch} represent the carrier concentration masses in research literatures, [4], [25]. The correct description of *DOS effective Masses (mdos)* and their relation to the carrier concentration masses m_{cce} and m_{cch} will be explained later on in this document.

Density of states masses *mdos* of carriers have different characteristics for a spherical-parabolic band and for a nonspherical-nonparabolic band. *mdos* for a spherical-parabolic band does not depend on energy (as explained in a later section). This type of

constant *mdos* is due to the curvature of the band, and is often called *band-edge curvature mass*.

It will now be shown how *mdos* for a spherical-parabolic band is different from the *mdos* for a nonspherical-nonparabolic band, and what this difference means for the density of states and for the carrier concentration of the spherical band versus the nonspherical band.

2.3 ENERGY BAND STRUCTURE

For a **nonspherical-nonparabolic band**, the band structure is given by

$$f(E,\theta,\phi) = \frac{\hbar^2 k^2}{2m_0} \tag{4}$$

where

m_0 is the electron mass

$f(E,\theta,\phi)$ is an energy function depending upon band energy and the spherical coordinate angles θ and ϕ.

k is the wave-vector of the electron or holes concerned.

For a **spherical-parabolic band**, k is independent of spherical coordinate angles. Hence, expression (4) holds true, but now the energy function $f(E,\theta,\phi)$ has the simple form

$$f(E,\theta,\phi) = \frac{Em_{dos}}{m_0} \tag{5}$$

where m_{dos} is a constant and is the same as *mdos* explained earlier.

Consequently, the band structure for a spherical-parabolic band is

$$E = \frac{\hbar^2 k^2}{2m_{dos}}. \tag{6}$$

2.4 DENSITY OF STATES OF AN ENERGY BAND

For the general **nonspherical-nonparabolic band**, the density of states of the band has the expression

$$g(E) = \frac{1}{8\pi^3}\left(\frac{2m_0}{\hbar^2}\right)^{3/2} \int_0^{\pi}\int_0^{2\pi} \sqrt{f(E,\theta,\phi)}\, f'(E,\theta,\phi)\sin(\theta)\, d\theta d\phi \tag{7}$$

where

$$f'(E,\theta,\phi) = \frac{\partial f(E,\theta,\phi)}{\partial E}. \tag{8}$$

For the special case of **spherical-parabolic band**, since

$$f(E,\theta,\phi) = \frac{E m_{dos}}{m_0} \tag{9}$$

and

$$f'(E,\theta,\phi) = \frac{\partial}{\partial E}\left(\frac{E m_{dos}}{m_0}\right) = \frac{m_{dos}}{m_0}, \tag{10}$$

the density of states becomes:

$$g(E) = \frac{1}{8\pi^3}\left(\frac{2m_0}{\hbar^2}\right)^{3/2} \int_0^{\pi}\int_0^{2\pi} \sqrt{\frac{E m_{dos}}{m_0}}\, \frac{m_{dos}}{m_0}\sin(\theta)\, d\theta d\phi \tag{11}$$

which reduces to expression (12):

$$g(E) = \frac{1}{8\pi^3}\left(\frac{2m_0}{\hbar^2}\right)^{3/2} \sqrt{\frac{E m_{dos}}{m_0}}\, \frac{m_{dos}}{m_0} \int_0^{\pi}\int_0^{2\pi} \sin(\theta)\, d\theta d\phi = \frac{1}{8\pi^3}\left(\frac{2m_0}{\hbar^2}\right)^{3/2} \sqrt{\frac{E m_{dos}}{m_0}}\, \frac{m_{dos}}{m_0} 4\pi =$$

$$= \frac{1}{2\pi^2}\left(\frac{2m_{dos}}{\hbar^2}\right)^{3/2} \sqrt{E}$$

Comparing the density of states $g(E)$ for spherical (eqn 12) and nonspherical (eqn 7) bands, we choose ***mdos* for a nonspherical-nonparabolic mass** as:

$$m_{dos}(E) = m_0 \left(\frac{\int_0^{\pi} \int_0^{2\pi} \sqrt{f(E,\theta,\phi)} f'(E,\theta,\phi) \sin(\theta) d\theta d\phi}{4\pi\sqrt{E}} \right)^{2/3} \qquad (13)$$

and with this value of *mdos*, the density of states for the nonspherical band becomes

$$g(E) = \frac{1}{2\pi^2} \left(\frac{2m_{dos}(E)}{\hbar^2} \right)^{3/2} \sqrt{E} \ , \qquad (14)$$

similar to the density of states of the spherical band. Clearly, for the nonspherical-nonparabolic band, the density of states effective mass $m_{dos}(E)$ is not a constant anymore, because it depends on the energy E in the band.

2.5 CARRIER CONCENTRATION OF AN ENERGY BAND

The carrier concentration for an energy band is defined as

$$n = \int_0^{\infty} g(E) F(E) dE \qquad (15)$$

where

$F(E)$ is the Fermi-Dirac distribution function.

For the **spherical parabolic band**, such as the conduction band of silicon, the carrier concentration is

$$n_0 = \frac{1}{2\pi^2} \left(\frac{2m_{dos}}{\hbar^2} \right)^{3/2} \int_0^{\infty} \frac{\sqrt{E}}{1 + \exp(\frac{E - E_F}{k_B T})} dE \, , \qquad (16)$$

while for a **nonspherical-nonparabolic band**, such as the valence band of silicon, the carrier concentration is

$$p_0 = \int_0^{\infty}\int_0^{\pi}\int_0^{2\pi} \frac{1}{8\pi^3}\left(\frac{2m_0}{\hbar^2}\right)^{3/2} \frac{\sqrt{f(E,\theta,\phi)}f'(E,\theta,\phi)}{1+\exp(\frac{E-E_F}{k_BT})} dE\sin(\theta)d\theta d\phi \,. \qquad (17)$$

Comparing the carrier concentrations for spherical (eqn 16) and non-spherical (eqn 17) bands, we can choose the **value of carrier concentration mass m_{CC} for the non-spherical band** as

$$m_{CC}^{3/2} = \frac{m_0^{3/2}}{4\pi} \frac{\int_0^{\infty}\int_0^{\pi}\int_0^{2\pi} \frac{\sqrt{f(E,\theta,\phi)}f'(E,\theta,\phi)}{1+\exp(\frac{E-E_F}{k_BT})} dE\sin(\theta)d\theta d\phi}{\int_0^{\infty} \frac{\sqrt{E}}{1+\exp(\frac{E-E_F}{k_BT})} dE}, \qquad (18)$$

Using the density of states mass $m_{dos}(E)$ for non-spherical bands chosen above, we finally obtain

$$m_{CC}^{3/2} = \frac{1}{(k_BT)^{3/2}F_{1/2}(\frac{E_F}{k_BT})} \int_0^{\infty} \frac{m_{dos}^{3/2}(E)\sqrt{E}dE}{1+\exp(\frac{E-E_F}{k_BT})} \qquad (19)$$

where $F_{1/2}$ is the Fermi integral of order $1/2$. Using this carrier concentration mass, the carrier density for the nonspherical band is written as

$$p_0 = \frac{1}{2\pi^2}\left(\frac{2m_{CC}}{\hbar^2}\right)^{3/2} \int_0^{\infty} \frac{\sqrt{E}}{1+\exp(\frac{E-E_F}{k_BT})} dE \qquad (20)$$

similarly in form to the carrier concentration n_0 of the spherical band.

For spherical parabolic bands,

$$n_0 = \frac{1}{2\pi^2}\left(\frac{2m_{dos}}{\hbar^2}\right)^{3/2}\int_0^{\infty}\frac{\sqrt{E}}{1+\exp(\frac{E-E_F}{k_BT})}dE \qquad (21)$$

For spherical-parabolic bands, *mdos* has a constant value that is the same as m_{cc}. It is a constant value because the mass in the spherical-parabolic bands has no energy dependence. On the other hand, for a nonspherical-nonparabolic band, the mass that appears in the density of states $g(E)$ is different from the mass that appears in the carrier concentration. *mdos* is dependent on energy , and, by integrating it over energy weighted by the Fermi-Dirac distribution we obtain the carrier concentration mass which, finally, has no energy dependence.

Another interesting observation is that for spherical-parabolic bands the carrier concentration mass has no temperature dependence, while for nonspherical-nonparabolic bands the carrier concentration mass clearly depends on temperature T.

2.6 *mdos* AND m_{cc} OF ELECTRONS

Since the conduction band is spherical-parabolic for silicon, germanium, and their strained and unstrained alloys $Si_{1-x}Ge_x$, the density of states/carrier concentration mass of electrons does not depend on energy. Fischetti and Laux [4] have calculated and plotted the electron longitudinal and transverse *mdos*.

In **silicon** the conduction band minima are along the [100] directions, and there are 6 symmetry equivalent minima leading to 6 equivalent ellipsoids in k-space. Fig. 2.1 below shows the geometry of the conduction and valence bands of silicon.

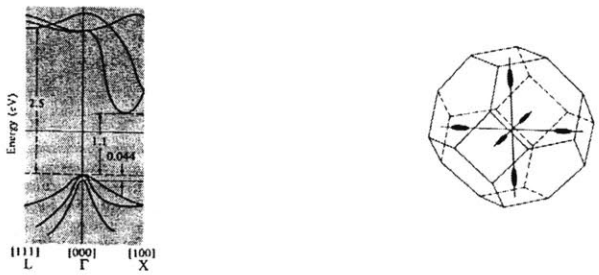

(a) (b)

Fig . 2.1. (a) Band structure and (b) conduction band minima, in silicon.

Therefore, the longitudinal and transverse masses correspond to the three ellipsoid axes (each axis having 2 of the 6 ellipsoids of the conduction band minima), and the total mass that enters in the carrier concentration formula is a composite of these longitudinal and transverse masses, by the formula

$$m_{dos}^{3/2} = 6\sqrt{m_L m_T m_T} \qquad (22)$$

This formula is derived from a solid-state calculation of the total density of states due to all three masses.

In **germanium** the situation is somewhat different. The conduction band minimum is along the [111] direction at the zone boundary (boundary of the first Brouillon Zone), and there are 8 symmetry-equivalent [111] directions. However, the ellipsoids are cut in half by the zone boundary, and this leads to 4 conduction band minima in Ge.

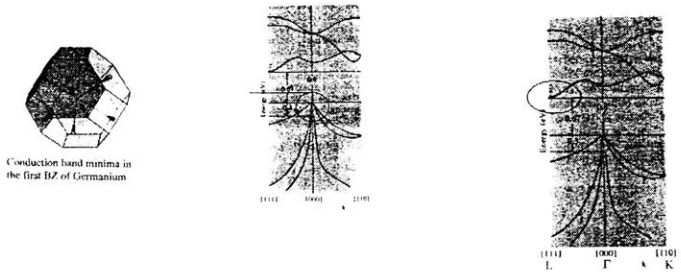

Fig . 2.2. Band structure and conduction band minima in germanium.

The total mass that enters in the carrier concentration formula is a composite of these longitudinal and transverse masses, by considering the 4 equivalent ellipsoids, and the expression is

$$m_{dos}^{3/2} = 4\sqrt{m_L m_T m_T} \qquad (23)$$

To the best knowledge of the author, no literature is available about strained $Si_{1-x}Ge_x$ on relaxed $Si_{1-y}Ge_y$. Only strained $Si_{1-x}Ge_x$ on Si and $Si_{1-x}Ge_x$ on Ge has been studied to date by contemporary researchers [4]. By using the data in [4] for strained $Si_{1-x}Ge_x$ on Si and on Ge and interpolating between the two, effective electron masses for strained $Si_{1-x}Ge_x$ for various strains can be obtained.

2.7 *mdos* AND m_{cc} OF HOLES

The situation is much more complicated for holes, because the valence band is nonspherical-nonparabolic. Therefore the energy dependent $m_{dos}(E)$ is needed in order to obtain the carrier concentration mass $m_{CC}(T)$, where T is temperature.

2.7.1 RELATED WORK

To my best knowledge, the work by Fischetti and Laux [4] is the best compilation to date of available density of states masses for holes in SiGe. Their paper has only one $m_{dos}(E)$ value, namely the value at thermal energy, 25mcV is plotted by them for

1. Relaxed $Si_{1-x}Ge_x$ for x between 0 and 1.
2. For strained Si and strained Ge submitted to various stresses.
3. For strained $Si_{1-x}Ge_x$ on Si and strained $Si_{1-x}Ge_x$ on Ge.

Their data thus does not allow to find the carrier concentration mass $m_{CC}(T)$ and its dependence of temperature for these SiGe alloys, because $m_{dos}(E)$ is calculated only for one energy value (25meV).

Two papers by Manku and Nathan [15], [20] find $m_{dos}(E)$ for the entire energy spectrum for strained $Si_{1-x}Ge_x$ on Si for only four values of x (0.05, 0.1, 0.2, 0.3). However, they also have not covered relaxed $Si_{1-x}Ge_x$ or strained $Si_{1-x}Ge_x$ on relaxed $Si_{1-y}Ge_y$.

A survey of the literature shows that $m_{dos}(E)$ for the entire energy spectrum and $m_{CC}(T)$ have never been determined for relaxed $Si_{1-x}Ge_x$ and for strained $Si_{1-x}Ge_x$ on relaxed $Si_{1-y}Ge_y$.

2.7.2 CALCULATION OF *mdos* FOR ENTIRE SPECTRUM FOR RELAXED SiGe AND STRAINED SiGe OVER RELAXED SiGe.

In this section, I will show

1. The formal methodology for the calculation of aforementioned masses.

2. Results for $m_{dos}(E)$ for the entire energy spectrum for relaxed $Si_{1-x}Ge_x$ for any value of x between 0 and 1.
3. Results for strained $Si_{1-x}Ge_x$ on relaxed $Si_{1-y}Ge_y$ for any values of x between 0 and 1 and of y between 0 and 1.
4. $m_{CC}(T)$ for all the above-mentioned combinations of SiGe.
5. Plots of Energy spectra capturing the correspondence between valence band structure changes and the percentage of Ge .
6. Constant energy surface plots to capture the relation between valence band structure changes and the amount of strain (deformation energy).

The implementation for this project has been on Mathematica, which is a well-known engineering tool.

2.7.3 OBTAINING BAND STRUCTURE BY THE KP METHOD

The band structure of a semiconductor can be obtained by using various methods, of which a few are listed here:

1. The pseudopotential method
2. The LCAO (linear coupled atomical orbital) method
3. The free-electron approximation method
4. The **kp** perturbation method.

I will use the **kp** method developed by Pikus and Bir [23], [24], in my approach. In this method, one starts by writing the one-electron Schrodinger equation for a periodic lattice

$$\left(\frac{\vec{p}^2}{2m_0}+V(\vec{r})+\frac{\hbar}{m_0}(\vec{k}\cdot\vec{p})\right)u_{n,\vec{k}}(\vec{r})=\left(E_{n,\vec{k}}-\frac{\hbar^2\vec{k}^2}{2m_0}\right)u_{n,\vec{k}}(\vec{r}) \qquad (24)$$

where

$V(\vec{r})$ is the potential of the unstrained unit cell

$E_{\vec{k}}$ is the energy spectrum of the unstrained material at $\vec{k}$

$u_{\vec{k}}(\vec{r})$ is the unstrained electron Bloch wave function which is cell-periodic

m_0 is the electron mass.

At $\vec{k}_0 = 0$, the above Schrodinger equation is

$$\left(\frac{\vec{p}^2}{2m_0} + V(\vec{r})\right) u_{n,\vec{0}}(\vec{r}) = E_{n,\vec{0}} u_{n,\vec{0}}(\vec{r}) \qquad (25)$$

The essence of the **kp** method lies in treating the term $\frac{\hbar}{m_0}(\vec{k}\cdot\vec{p})$ as a perturbation, for $\vec{k} \neq 0$. From perturbation theory, the energy at $\vec{k}$ (that is, including the perturbation effects) is

$$E_{n,\vec{k}} = E_{n,\vec{0}} + \frac{\hbar^2 k^2}{2m_0} + \frac{\hbar}{m_0^2}\sum_{j\neq n} \frac{\left|\left\langle u_{n,\vec{0}}(\vec{r}) \,|\, \vec{k}\cdot\vec{p} \,|\, u_{j,\vec{0}}(\vec{r})\right\rangle\right|^2}{E_{n,\vec{0}} - E_{j,\vec{0}}}. \qquad (26)$$

The easiest way of finding $E_{n,\vec{k}}$ for a given semiconductor is to solve the perturbation eigenvalue equation directly, rather than applying the above formula. The eigenvalues we want to find are

$$E'_{\vec{k}} = E_{\vec{k}} - \frac{\hbar^2 \vec{k}^2}{2m_0}. \qquad (27)$$

These eigenvalues are all we need in order to determine effective masses. The solution has three energy eigenvalues that correspond to three types of holes, the heavy-holes, light-holes and split-off holes. For silicon and germanium which have lattices where inversion is a symmetry operation (diamond lattices), the first order matrix elements of

the $\vec{k} \cdot \vec{p}$ perturbation vanish at $k = 0$ [10]. For a complete orthonormal finite set $|u_{i,J}\rangle$ of cell-periodic wave functions at $k = 0$, where J indexes different energies and i refers to degenerate functions for a given energy, any vector in the vector space of one given energy (a given J) can be expressed as a linear combination of $|u_{i,J}\rangle$, that is, it can be expressed as $c_1 u_{1,J} + c_2 u_{2,J} + ... + c_n u_{n,J}$. The first order matrix elements of the $\vec{k} \cdot \vec{p}$ perturbation vanish as explained above. The second order effects will have influence, and will manifest themselves in energy. The energies are found by determining the eigenvalues of the finite matrix equation

$$H_{kp} \begin{pmatrix} c_1 \\ c_2 \\ . \\ . \\ c_n \end{pmatrix} = E_k' \begin{pmatrix} c_1 \\ c_2 \\ . \\ . \\ c_n \end{pmatrix}. \tag{28}$$

H_{kp} is the perturbation term due to the $\frac{\hbar}{m_0}(\vec{k} \cdot \vec{p})$ term in the Schrodinger equation. H_{kp} can be expressed in matrix form, with elements having the units of energy. The form of the H_{kp} matrix has been determined for cubic and diamond lattices. For the silicon and germanium lattices, H_{kp} is a 3×3 matrix written as below:

$$H_{kp} = \begin{bmatrix} Lk_x^2 + M(k_y^2 + k_z^2) & Nk_x k_y & Nk_x k_z \\ Nk_x k_y & Lk_y^2 + M(k_x^2 + k_z^2) & Nk_y k_z \\ Nk_x k_z & Nk_y k_z & Lk_z^2 + M(k_y^2 + k_x^2) \end{bmatrix} \tag{29}$$

The L, M, N parameters are called valence band parameters. They are the essential data needed to obtain the valence-band structure for a material. The full details about L, M, and N would be provided shortly.

Both Si and Ge have three valence bands. Two are degenerate but have different curvatures. The third band is split-off from the other two bands by the spin-orbit coupling, and is called the split-off band. It is located below the two degenerate bands, by 44meV for Si and by 296meV for Ge. The $k_0 = 0$ for the valence bands is at the Γ-point, center of the Brouillon zone. The valence bands are atomic p-like near the Γ-point. Because of this, the three valence bands are often classified according to their angular momenta. As in an atom, the p-orbitals are classified according to j, and $j = \frac{1}{2}, \frac{3}{2}$ are the resulting angular momenta. The $j = \frac{3}{2}$ states form the heavy hole and light hole bands, and the $j = \frac{1}{2}$ state forms the split-off band. The three states for heavy, light, and split-off bands are called ε_1^+, ε_2^+, ε_3^+. They form our degenerate basis functions.

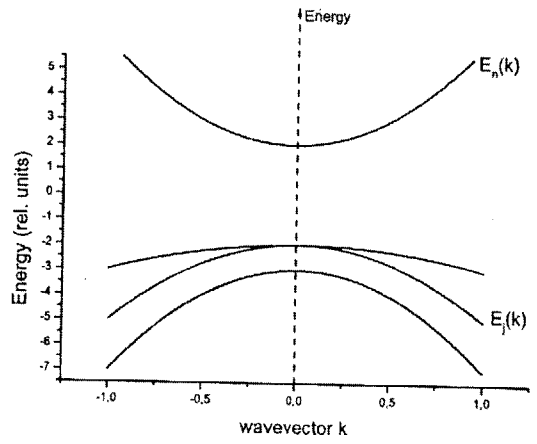

Fig . 2.3. The valence bands of Si and Ge.

The matrix elements L, M, N are determined by the coupling of the valence bands to all other energy bands (usually, the conduction bands). The coupling is mainly

determined by the interaction between the valence bands and the first 3 conduction bands. Denoting these three conduction bands involved in the coupling with α_i where $i = 1,2,3$, the terms L, M, N are:

$$L = \frac{\hbar^2}{m_0} \sum_i \frac{\langle 1+ | p_x | \alpha_i \rangle \langle \alpha_i | p_x | 1+ \rangle}{E_0 - E_{\alpha_i}} \tag{30}$$

$$M = \frac{\hbar^2}{m_0} \sum_i \frac{\langle 1+ | p_y | \alpha_i \rangle \langle \alpha_i | p_y | 1+ \rangle}{E_0 - E_{\alpha_i}} \tag{31}$$

$$N = \frac{\hbar^2}{m_0} \sum_i \frac{\langle 1+ | p_x | \alpha_i \rangle \langle \alpha_i | p_y | 2+ \rangle + \langle 1+ | p_y | \alpha_i \rangle \langle \alpha_i | p_x | 2+ \rangle}{E_0 - E_{\alpha_i}} \tag{32}$$

where p_x , p_y, 1+ and 2+ operators refer to the valence bands (p_x and p_y refer to the momentum operator **p**), E_0 is the valence band energy that we seek, and E_{α_i} are the energies of the conduction bands α_i where $i = 1,2,3$. The theoretical expressions of L, M and N are complicated. Luckily, these coefficients have been calculated and plotted for relaxed $Si_{1-x}Ge_x$. For Si the coefficients are L= -6.53, M= -4.64 , N= -8.75 and for Ge L= -31.53, M= -5.64, N=-33.64, in units of $\frac{\hbar^2}{2m_0}$. Rieger and Vogl [25] have calculated from theory the L, M and N coefficients, but their data does not fit the Ge values.

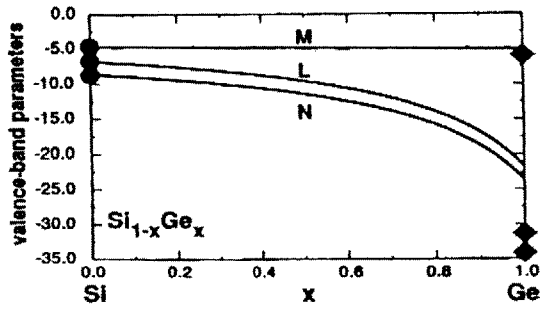

Fig . 2.4. Calculated valence-band parameters in an unstrained $Si_{1-x}Ge_x$ alloy by Rieger and Vogl [25]. For pure Si and Ge the experimental results are shown for comparison. The valence-band parameters are given in units of $\frac{\hbar^2}{2m_0}$.

Merkler has corrected the theory and obtained the L, M, N dependence on Ge percentage correctly, theoretically fitting both the Si and the Ge values. Below is the graph of Merkler.

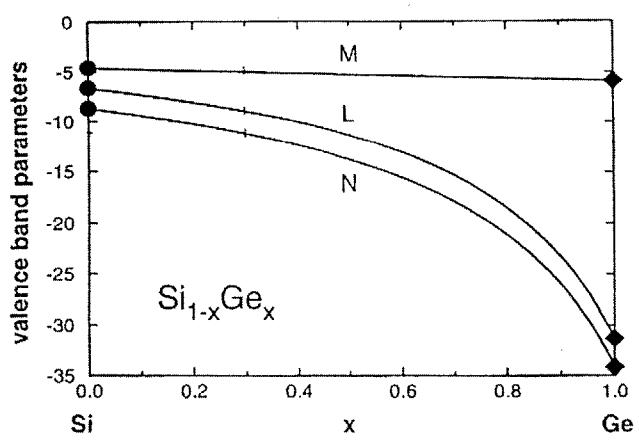

Fig . 2.6. Calculated valence-band parameters in an unstrained $Si_{1-x}Ge_x$ alloy by Merkler [29]. For pure Si and Ge the experimental results are shown for comparison. The valence-band parameters are given in units of $\frac{\hbar^2}{2m_0}$. The calculation is a non-linear interpolation following the scheme of Lawaetz [12].

I will describe now how, using the coefficients L, M and N, we can find the band structure of the valence band, namely, the eigenvalues $E_{\vec{k}} = E(k)$. Once we have the dependence $E(k)$, or, reciprocally, $k(E)$, we can find the function

$$f(E,\theta,\phi) = \frac{\hbar^2 k^2}{2m_0} \qquad (4)$$

and from that the effective masses that we are looking for. The H_{kp} matrix is written below [19]. I will rename the H_{kp} matrix as S:

$$S=H_{kp}=\begin{bmatrix} Lk_x^2+M(k_y^2+k_z^2) & Nk_xk_y & Nk_xk_z \\ Nk_xk_y & Lk_y^2+M(k_x^2+k_z^2) & Nk_yk_z \\ Nk_xk_z & Nk_yk_z & Lk_z^2+M(k_y^2+k_x^2) \end{bmatrix} \tag{33}$$

By solving the eigenvalue equation $S\vec{v}=E_k^{'}\vec{v}$ we obtain the band structure of the unstrained valence bands, without including any spin-orbit interaction.

In case of strained $Si_{1-x}Ge_x$ we must include the effect of strain. This effect is easy to quantize by the deformation matrix whose general form is:

$$D=\begin{bmatrix} l\varepsilon_{xx}+m(\varepsilon_{yy}+\varepsilon_{zz}) & n\varepsilon_{xy} & n\varepsilon_{xz} \\ n\varepsilon_{xy} & l\varepsilon_{yy}+m(\varepsilon_{xx}+\varepsilon_{zz}) & n\varepsilon_{yz} \\ n\varepsilon_{xz} & n\varepsilon_{yz} & l\varepsilon_{zz}+m(\varepsilon_{xx}+\varepsilon_{yy}) \end{bmatrix}. \tag{34}$$

The deformation matrix D is the first-order correction that arises due to straining effects. We will describe now what the terms that enter the deformation matrix are for our particular case of strained of $Si_{1-x}Ge_x$ grown on relaxed $\langle 001\rangle$ $Si_{1-y}Ge_y$. This growth results in biaxial in-plane compression of the strained SiGe, and consequently in the straining of SiGe both parallel and perpendicular to the growth direction. With the z axis along the direction of growth, the strained components of SiGe are easy to deduce [22]. The strain is in-plane, so there are no shear strain components:

$$0=\varepsilon_{xy}=\varepsilon_{yz}=\varepsilon_{zx}. \tag{35}$$

The other three strain components are, as follows from People's paper [22]:

$$\varepsilon_{xx}=\varepsilon_{yy}=\frac{a_s(y)-b(x)}{b(x)} \tag{36}$$

$$\varepsilon_{zz} = \varepsilon_{xx} + \left[\frac{1+\upsilon}{1-\upsilon}\right]\left[\frac{b(x)-a_s(y)}{a_s(y)}\right] \tag{37}$$

where

$a_s(y)$ is the lattice constant of the $Si_{1-y}Ge_y$ substrate

$b(x)$ is the unstrained lattice constant of $Si_{1-x}Ge_x$.

υ is the Poisson ratio.

So $Si_{1-x}Ge_x$ has a lattice of $b(x)$ when by itself, but it will assume a lattice of $a_s(y)$ when strained, that is, when grown on the $Si_{1-y}Ge_y$ substrate.

Now we have the ε_{xx}, ε_{yy}, ε_{zz}, ε_{xy}, ε_{yz} and ε_{zx} terms in the deformation matrix D above, we also need the l, m, n values to be able to compute the matrix D. It does not matter what n is since $0 = \varepsilon_{xy} = \varepsilon_{yz} = \varepsilon_{zx}$. For uniaxial strain, $m = \frac{2}{3}D_d + \frac{2}{3}D_u$, and $l = \frac{2}{3}D_d - \frac{4}{3}D_u$, where D_u is the band splitting deformation potential and D_d is the volume deformation potential [8] [9] [15].

The deformation matrix therefore becomes:

$$\mathrm{D}=\frac{2}{3}D_d(2\varepsilon_{xx}+\varepsilon_{zz})\begin{bmatrix}1&0&0\\0&1&0\\0&0&1\end{bmatrix}+\begin{bmatrix}\frac{2}{3}D_u(\varepsilon_{zz}-\varepsilon_{xx})&0&0\\0&\frac{2}{3}D_u(\varepsilon_{zz}-\varepsilon_{xx})&0\\0&0&-\frac{4}{3}D_u(\varepsilon_{zz}-\varepsilon_{xx})\end{bmatrix} \tag{38}$$

Denoting

$$\varepsilon_{un} = \frac{2}{3}D_d(2\varepsilon_{xx}+\varepsilon_{zz}) \tag{39}$$

and

$$\varepsilon_{def} = \frac{2}{3} D_u (\varepsilon_{zz} - \varepsilon_{xx}) \tag{40}$$

the matrix D becomes

$$\mathrm{D} = \varepsilon_{un} \begin{bmatrix} 1 & 0 & 0 \\ 0 & 1 & 0 \\ 0 & 0 & 1 \end{bmatrix} + \begin{bmatrix} \varepsilon_{def} & 0 & 0 \\ 0 & \varepsilon_{def} & 0 \\ 0 & 0 & -2\varepsilon_{def} \end{bmatrix} \tag{41}$$

The parameters involved in the deformation coefficients above are summarized below [7], [8], [9]:

Parameters	Si	Ge
a $(\mathring{A})$	5.4309	5.646
υ	0.280	0.273
D_u (eV)	2.04	3.32

Table 1. Parameters that enter the deformation coefficients

For a given $Si_{1-x}Ge_x$ alloy, the values of the lattice constant, Poisson ratio and D_u potential are found by a linear interpolation of values for Si and Ge. The value of D_d is not known exactly, but, as we will see, we do not need the D_d value to determine the density of states masses or the energy spectrum.

The effect of strain is included by using the matrix S+D instead of S in the eigenvalue equation:

$$(S + D)\vec{v} = E_k^{'}\vec{v}\,. \tag{42}$$

We have yet to include the spin-orbit coupling effect. When spin-orbit effects are included, we take as our degenerate basis functions $\varepsilon_1^+ \uparrow$, $\varepsilon_2^+ \uparrow$, $\varepsilon_3^+ \uparrow$, $\varepsilon_1^+ \downarrow$, $\varepsilon_2^+ \downarrow$,

$\varepsilon_3^+ \downarrow$, where $\uparrow$ and $\downarrow$ designate the spin functions spin-up and spin-down, or $\begin{pmatrix} 1 \\ 0 \end{pmatrix}$ and $\begin{pmatrix} 0 \\ 1 \end{pmatrix}$. In this representation, the k-independent spin-orbit perturbation has the form:

$$H_{so} = -\frac{\Delta}{3}\begin{bmatrix} 0 & i & 0 & 0 & 0 & -1 \\ -i & 0 & 0 & 0 & 0 & i \\ 0 & 0 & 0 & 1 & -i & 0 \\ 0 & 0 & 1 & 0 & -i & 0 \\ 0 & 0 & i & i & 0 & 0 \\ -1 & -i & 0 & 0 & 0 & 0 \end{bmatrix} \tag{43}$$

where Δ is the spin-orbit splitting energy. Δ is 44meV for Si and 296meV for Ge. For a given $Si_{1-x}Ge_x$ alloy, the value of the spin-orbit splitting is found by a linear interpolation of values for Si and Ge [4], [22]. The spin-orbit interaction depends only on the constant Δ, that is, only on the lattice spacing. This happens because of the symmetry properties of the diamond-lattice crystal.

Also, in this representation, the Hamiltonian S from the eigenvalue equation, which was a 3×3 matrix, becomes a 6×6 matrix which may be written schematically $\begin{pmatrix} S & 0 \\ 0 & S \end{pmatrix}$. We call this new matrix S_1.

$S_1 =$ (44)

$$\begin{matrix} {}^{2}_{\kappa} + M(k_y^2 + k_z^2) & Nk_xk_y & Nk_xk_z & 0 & 0 & 0 \\ Nk_xk_y & Lk_y^2 + M(k_x^2 + k_z^2) & Nk_yk_z & 0 & 0 & 0 \\ Nk_xk_z & Nk_yk_z & Lk_z^2 + M(k_y^2 + k_x^2) & 0 & 0 & 0 \\ 0 & 0 & 0 & Lk_x^2 + M(k_y^2 + k_z^2) & Nk_xk_y & Nk_xk_z \\ 0 & 0 & 0 & Nk_xk_y & Lk_y^2 + M(k_x^2 + k_z^2) & Nk_yk_z \\ 0 & 0 & 0 & Nk_xk_z & Nk_yk_z & Lk_z^2 + M(k_y^2 + k_x^2) \end{matrix}$$

The deformation matrix D from the eigenvalue equation also becomes a 6×6 matrix which may be written schematically $\begin{pmatrix} D & 0 \\ 0 & D \end{pmatrix}$ and will be called D_1

$$D_1 = \begin{bmatrix} \varepsilon_{un} & 0 & 0 & 0 & 0 & 0 \\ 0 & \varepsilon_{un} & 0 & 0 & 0 & 0 \\ 0 & 0 & \varepsilon_{un} & 0 & 0 & 0 \\ 0 & 0 & 0 & \varepsilon_{un} & 0 & 0 \\ 0 & 0 & 0 & 0 & \varepsilon_{un} & 0 \\ 0 & 0 & 0 & 0 & 0 & \varepsilon_{un} \end{bmatrix} + \begin{bmatrix} \varepsilon_{def} & 0 & 0 & 0 & 0 & 0 \\ 0 & \varepsilon_{def} & 0 & 0 & 0 & 0 \\ 0 & 0 & -2\varepsilon_{def} & 0 & 0 & 0 \\ 0 & 0 & 0 & \varepsilon_{def} & 0 & 0 \\ 0 & 0 & 0 & 0 & \varepsilon_{def} & 0 \\ 0 & 0 & 0 & 0 & 0 & -2\varepsilon_{def} \end{bmatrix} \tag{45}$$

It is important to say here that the diagonal identity matrix-like in ε_{un} above will only contribute to a relative shift in energy and not to the curvature of the band. Therefore the ε_{un} part of the matrix above will not influence the effective mass and energy band structure calculation and will be ignored, so the matrix D_1 we will work with (the deformation that influences the curvature of the band) will be only

$$D_1 = \begin{bmatrix} \varepsilon_{def} & 0 & 0 & 0 & 0 & 0 \\ 0 & \varepsilon_{def} & 0 & 0 & 0 & 0 \\ 0 & 0 & -2\varepsilon_{def} & 0 & 0 & 0 \\ 0 & 0 & 0 & \varepsilon_{def} & 0 & 0 \\ 0 & 0 & 0 & 0 & \varepsilon_{def} & 0 \\ 0 & 0 & 0 & 0 & 0 & -2\varepsilon_{def} \end{bmatrix}. \tag{46}$$

Now all three matrices H_{so}, S_1 and D_1, which are all 6×6 matrices, have to be added together and the eigenvalue equation becomes

$$(H_{so} + S_1 + D_1)\vec{v} = E_k^{'}\vec{v}\,. \tag{47}$$

We could go ahead and solve this equation for its eigenvalues, but this task would prove very difficult. The reason for this difficulty is that the matrix $H_{so} + S_1 + D_1$ is not symmetrical across the diagonal (because, although $S_1 + D_1$ is symmetrical across diagonal, the matrix H_{so} is not).

The way to circumvent this difficulty is to try to diagonalize the matrix H_{so}. This is done by finding a unitary matrix U, which has the property that it makes $U^{-1}H_{so}U$ be diagonal. (The eigenvalues of a matrix do not change when the matrix is multiplied by a unitary matrix in this way.) The matrix U that does the trick is

$$U = \begin{bmatrix} -\frac{1}{\sqrt{2}} & 0 & 0 & 0 & \frac{1}{\sqrt{6}} & \frac{1}{\sqrt{3}} \\ -\frac{i}{\sqrt{2}} & 0 & 0 & 0 & -\frac{i}{\sqrt{6}} & -\frac{i}{\sqrt{3}} \\ 0 & \frac{2}{\sqrt{6}} & -\frac{1}{\sqrt{3}} & 0 & 0 & 0 \\ 0 & -\frac{1}{\sqrt{6}} & -\frac{1}{\sqrt{3}} & -\frac{1}{\sqrt{2}} & 0 & 0 \\ 0 & -\frac{i}{\sqrt{6}} & -\frac{i}{\sqrt{3}} & \frac{i}{\sqrt{2}} & 0 & 0 \\ 0 & 0 & 0 & 0 & \frac{2}{\sqrt{6}} & -\frac{1}{\sqrt{3}} \end{bmatrix} \tag{48}$$

This matrix is in fact the unitary transformation matrix of the JM_J quantum mechanical representation.

The transformed $H_{so}^{'}$ matrix will be

$$H_{so}^{'} = U^{-1}H_{so}U = \begin{bmatrix} \Delta/3 & 0 & 0 & 0 & 0 & 0 \\ 0 & \Delta/3 & 0 & 0 & 0 & 0 \\ 0 & 0 & -2\Delta/3 & 0 & 0 & 0 \\ 0 & 0 & 0 & \Delta/3 & 0 & 0 \\ 0 & 0 & 0 & 0 & \Delta/3 & 0 \\ 0 & 0 & 0 & 0 & 0 & -2\Delta/3 \end{bmatrix} \tag{49}$$

The final matrix whose eigenvalues we will find is

$$H_{tot} = H_{so}^{'} + U^{-1}(S_1 + D_1)U = U^{-1}(S_1 + D_1 + H_{so})U \tag{50}$$

and the eigenvalue equation is:

$$H_{tot}\left|J;M_J\right\rangle = \lambda(\vec{k})\left|J;M_J\right\rangle \tag{51}$$

where $\lambda(\vec{k})$ are the eigenvalues of H_{tot}, and they depend on $\vec{k}$ that is on k_x, k_y, and k_z, and $\left|J;M_J\right\rangle$ are the eigenvectors. The energy-band structure of the valence band for each eigenvalue is obtained in the following way:

$$E(\vec{k}) = \frac{\hbar^2 \vec{k}^2}{2m} + \lambda(\vec{k}) \tag{52}$$

The matrix H_{tot} is a 6×6 matrix. To find the eigenvalues of a matrix we must solve the determinant equation:

$$\det(H_{tot} - \begin{bmatrix} \lambda(\vec{k}) & 0 & 0 & 0 & 0 & 0 \\ 0 & \lambda(\vec{k}) & 0 & 0 & 0 & 0 \\ 0 & 0 & \lambda(\vec{k}) & 0 & 0 & 0 \\ 0 & 0 & 0 & \lambda(\vec{k}) & 0 & 0 \\ 0 & 0 & 0 & 0 & \lambda(\vec{k}) & 0 \\ 0 & 0 & 0 & 0 & 0 & \lambda(\vec{k}) \end{bmatrix}) = 0 \tag{53}$$

This is clearly a 6^{th} order equation, so we would expect it to have 6 eigenvalues solutions $\lambda(\vec{k})$. In fact, it turns out that the determinant 6^{th} order eigenvalue equation above is actually the square of a 3^{rd} order equation: $Y(order6) = (Z(order3))^2 = 0$

This fact is due to the matrix H_{tot} being block-diagonal. The 3^{rd} order equation $Z(order3) = 0$ has 3 different eigenvalues $\lambda(\vec{k})$ and consequently 3 energy-band

structures, which will correspond to the heavy-hole band, light-hole band, and spin-off hole band.

Since

$$E = \frac{\hbar^2 \vec{k}^2}{2m} + \lambda(\vec{k}), \text{ then } \lambda(\vec{k}) = E - \frac{\hbar^2 \vec{k}^2}{2m}. \tag{54}$$

We replace $\lambda(\vec{k})$ by $E - \frac{\hbar^2 \vec{k}^2}{2m}$ in the eigenvalue equation $Z(order3) = 0$ and we obtain the 3rd order equation in E and $\vec{k}^2$. The 3rd order equation, as derived by Kane, or as derived by Maple formula manipulation, is:

$$h_{11}' h_{22}' h_{33}' + 2h_{12} h_{23} h_{31} - h_{11}' h_{23}^2 - h_{22}' h_{13}^2 - h_{33}' h_{12}^2 - \frac{\Delta}{3}(h_{11}' h_{22}' + h_{11}' h_{33}' + h_{22}' h_{33}' - h_{12}^2 - h_{23}^2 - h_{31}^2) = 0 \tag{55}$$

where

$h_{ij} = S_{ij} + D_{ij}$

S_{ij} and D_{ij} are the matrix elements of the initial 3×3 matrices S and D

$$h_{ii}' = h_{ii} + \frac{\hbar^2 \vec{k}^2}{2m} - E \tag{56}$$

where $\vec{k} = \hat{i}_1 k_x + \hat{i}_2 k_y + \hat{i}_3 k_z = \hat{i}_1 k \sin\theta \cos\phi + \hat{i}_2 k \sin\theta \sin\phi + \hat{i}_3 k \cos\theta$ in polar coordinates. This is a third order equation in k^2. We would like to solve it and obtain k^2 versus E. There will be three solutions, $k_{HH}^2(E_{HH})$, $k_{LH}^2(E_{LH})$, $k_{SO}^2(E_{SO})$. Once we have $k^2(E)$ for each band we can find the density of states effective mass, the carrier concentration effective mass, the energy-spectrum for each band and the constant energy surfaces for each band.

Luckily, it is possible to find the solutions of a third order equation by a closed formula.

Our eigenvalue 3rd order equation is of the form

$$ak^6 + bk^4 + ck^2 + d = 0 \tag{57}$$

(where a, b, c and d depend on E); it is proved that the three solutions of any 3rd order equation like above are as follows [28]:

1. $k_{HH}^2 = 2\sqrt{-\frac{p}{3}}\cos(\alpha) - \frac{b}{3a}$ for heavy hole band

2. $k_{LH}^2 = 2\sqrt{-\frac{p}{3}}\cos(\alpha + \frac{4\pi}{3}) - \frac{b}{3a}$ for light hole band

3. $k_{SO}^2 = 2\sqrt{-\frac{p}{3}}\cos(\alpha + \frac{2\pi}{3}) - \frac{b}{3a}$ for split-off band (58)

where

$$p = \frac{c}{a} - 3\left(\frac{b}{3a}\right)^2$$

$$q = \frac{d}{a} - \frac{c}{a}\left(\frac{b}{3a}\right) + 2\left(\frac{b}{3a}\right)^3$$

$$\alpha = \frac{1}{3}\arccos\left(\frac{-q}{2\sqrt{-(p/3)^3}}\right).$$

We have now finished our analysis of the solutions to the 3rd order equation, and we must say what a, b, c and d are in terms of S_{ij}, D_{ij}, E, Δ etc. (all the parameters that enter in the h_{ij} terms of the equation written above).

It can be shown, that the a, b, c and d parameters are as below:

- $a = -(A+2B)(A-B)^2 + 3(A-B)C^2u - (N-3B)^2(2N+3B)v$

- $b = 3[(A^2 - B^2) - C^2 u](E + \frac{\Delta}{3}) - g_3$
- $c = -3AE(E + \frac{2\Delta}{3}) + \frac{\Delta}{3} g_1 - g_2 + g_1 E$
- $d = E^2(E + \Delta) + \frac{\Delta}{3}(pq + pr + qr) - pqr - E\frac{2\Delta}{3}(p + q + r) + E(pq + pr + qr) - E^2(p + q + r)$

(59)

where the various letters appearing in the expressions above are:

E is the negative hole energy taken from the top of the valence band downwards;

$$A = \frac{1}{3}(L + 2M) + \frac{\hbar^2}{2m_0}$$

$$B = \frac{1}{3}(L - M)$$

$$C^2 = \frac{1}{3}[(N^2 - (L - M)^2)]$$

where

L, M, N are the valence band parameters;

$u = \sin^2\theta(\sin^2\theta\cos^2\phi\sin^2\phi + \cos^2\theta)$

$v = \sin^4\theta\cos^2\theta\cos^2\phi\sin^2\phi$ where θ and ϕ are the polar coordinates angles;

$$p = \varepsilon_{def} = \frac{2}{3} D_u(\varepsilon_{zz} - \varepsilon_{xx})$$

$$q = p = \frac{2}{3} D_u(\varepsilon_{zz} - \varepsilon_{xx})$$

$$r = -2\varepsilon_{def} = -\frac{4}{3} D_u(\varepsilon_{zz} - \varepsilon_{xx})$$

$g_1 = \cos^2\theta[(p + q)(M + L) + 2rM] + \sin^2\theta[(p + q)M] + \sin^2\theta\cos^2\phi[M(p + r) + L(q + r)] +$
$+ \sin^2\theta\sin^2\phi[M(q + r) + L(p + r)] + (\hbar^2 / m)(p + q + r)$

$$g_2 = \cos^2\theta[pqL + rM(p+q)] + \sin^2\theta(pqM) + \sin^2\theta\cos^2\phi(prM + qrL) +$$
$$+ \sin^2\theta\sin^2\phi(qrM + prL) + (\hbar^2/2m)(pq + pr + qr)$$

$$g_3 = \sin^2\theta\cos^2\theta\cos^2\phi[ML(p+r) + rM^2 + q(L^2 - N^2)] +$$
$$+ \sin^2\theta\cos^2\theta\sin^2\phi[ML(q+r) + rM^2 + p(L^2 - N^2)] +$$
$$+ \sin^2\theta\cos^2\theta[M^2(p+q-r) - ML(p+q+r)] +$$
$$+ \sin^2\theta\cos^2\phi\frac{\hbar^2[M(p+r) + L(q+r)]}{2m_0} + \sin^2\theta\sin^2\phi\frac{\hbar^2[M(q+r) + L(p+r)]}{2m_0} +$$
$$+ \sin^2\theta\left[\frac{\hbar^2M(p+q)}{2m_0} + rML\right] - 3rC^2\sin^4\theta\sin^2\phi\cos^2\phi + \sin^4\theta\sin^2\phi(M^2q + MLp) +$$
$$+ \sin^4\theta\cos^2\phi(M^2p + MLq) + \cos^2\theta\left[\frac{\hbar^2M(p+q+2r)}{2m_0} + \frac{\hbar^2L(p+q)}{2m_0} + ML(p+q) + M^2r\right] +$$
$$+ \left(\frac{\hbar^2}{2m_0}\right)^2(p+q+r)$$

where the p, q, r, g_1, g_2, g_3 parameters are due solely to strain.

Once we have ${k_{HH}}^2(E)$, ${k_{LH}}^2(E)$, ${k_{SO}}^2(E)$, we can look at the energy spectrum, by plotting energy E versus k-vector, for the k-vector in the [010] and [001] directions. We can also look at the constant energy surfaces for any given energy, by plotting kz versus ky for that particular energy. And finally, we can calculate the density of states effective mass *mdos* and the carrier density effective mass which depends on temperature.

Based on the analysis done at the beginning of this chapter when we discussed effective masses, we first calculate:

$$V(E) = \frac{1}{3}\int_0^{\pi} d\theta \int_0^{2\pi} d\phi k^3(E,\theta,\phi)\sin(\theta) \qquad (60)$$

Then we obtain the density of states effective mass from:

$$mdos = \left(\frac{1}{2\pi\sqrt{E}} \frac{dV}{dE} \right)^{2/3} \left(\frac{\hbar^2}{2m_0} \right) \tag{61}$$

The carrier concentration effective mass is found from the integral

$$m_{CC}^{3/2}(\mu,T) = \frac{\beta^{3/2}}{F_{1/2}(\beta\mu)} \int_0^\infty \frac{mdos^{3/2}(E)E^{1/2}}{1+\exp[\beta(E-E_F)]} dE \tag{62}$$

where $\beta = \frac{1}{k_B T}$. The expression reduces to

$$m_{CC}^{3/2}(T) = \frac{2}{\sqrt{\pi}} \beta^{3/2} \int_0^\infty E^{1/2} mdos^{3/2}(E) \exp(-\beta E) dE \tag{63}$$

for the Fermi level sufficiently negative, that is, for $E_F < -3k_B T$.

This study is done for the heavy Hole, light hole and spin-off hole bands, and the total carrier concentration effective mass is a composite of all the masses, by the formula:

$$m_{CC,total} = (m_{CC,HH}^{3/2} + m_{CC,LH}^{3/2} + m_{CC,SO}^{3/2})^{2/3} \tag{64}$$

2.7.4 Implementation and Results

The main difficulty in implementing the study above in a computer language is given by the double integral in equation above. I tried to use Matlab, Maple, and Mathematica. Matlab can do simple double integrals, but it has problems with complicated integrals (it can not do them correctly and, in an effort to still do them it makes overrated approximations which give an erroneous result to the integral at the end), especially the ones that can not be expressed in closed form but only calculated numerically, such as our integral is.

Maple, while great for manipulating mathematical formulae, opening parenthesis and simplifying formulas, takes a computationally infeasible amount of time

in evaluating a double integral of the kind we have. The problem is exacerbated by the fact that we need to evaluate this double integral for many values of E.

Mathematica was the only one of the programs that worked. This is probably because Mathematica is geared towards numerical computation, while Matlab is geared more towards linear algebra and vector calculations, and Maple is rather good for symbolic (analytic) formula manipulation.

Running one program in Mathematica took between half an hour to 5 hours, depending on the complexity of the program.

The first study was of relaxed $Si_{1-x}Ge_x$. I used the L, M, N parameters from the Merkler graph (Fig.2.6). Since in relaxed SiGe there is no deformation matrix, the terms p, q, r, g_1, g_2, g_3, are all 0. We implement $k^2(E)$ by one of the expressions in formula 58, depending what types of holes are studied, then we implement $V(E)$ by formula 60 for energies E between $1meV$ and $70meV$ in steps of $1meV$, $mdos$ by formula 61 for the same energy range and finally m_{CC} versus temperature T by formula 63.

Fig.2.7. shows the heavy hole dos mass versus energy for Si, $Si_{90\%}Ge_{10\%}$, $Si_{70\%}Ge_{30\%}$, $Si_{50\%}Ge_{50\%}$, $Si_{30\%}Ge_{70\%}$, $Si_{10\%}Ge_{90\%}$, Ge. The highest effective masses are for silicon. To check the correctness of my calculations, I have compared the silicon effective mass curve I obtained to the silicon one obtained by Manku and Nathan [20], and the one obtained by Zukotinski [28], and they are identical. The values for the density of states effective mass at 25meV of Fischetti and Laux [4] (the only one they have calculated), are identical to my values at 25meV.

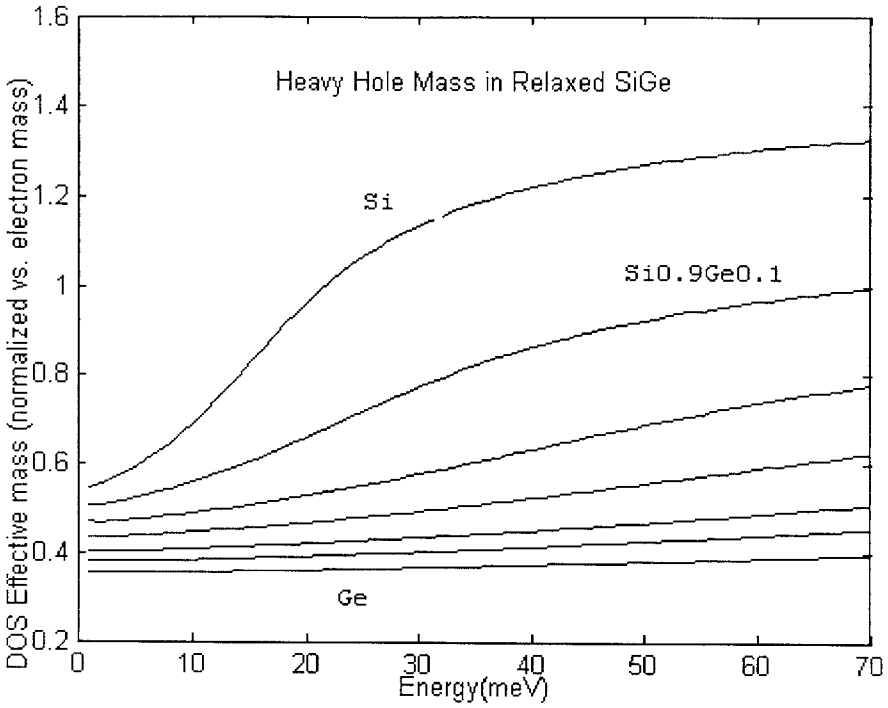

Fig . 2.7. Heavy Hole Mass in relaxed Si, $Si_{90\%}Ge_{10\%}$, $Si_{70\%}Ge_{30\%}$, $Si_{50\%}Ge_{50\%}$, $Si_{30\%}Ge_{70\%}$, $Si_{10\%}Ge_{90\%}$, Ge. Si is the highest graph and Ge is the lowest, with SiGe in between, $Si_{90\%}Ge_{10\%}$ closest to silicon, $Si_{10\%}Ge_{90\%}$ closest to germanium.

Fig.2.8. shows the values of the carrier concentration mass $m_{cc}(T)$ for relaxed Si, $Si_{90\%}Ge_{10\%}$, $Si_{70\%}Ge_{30\%}$, $Si_{50\%}Ge_{50\%}$, $Si_{30\%}Ge_{70\%}$, $Si_{10\%}Ge_{90\%}$, Ge. The graph is correct down to about 50K. This is due to the fact that the integration has been calculated as a sum and this would make formula blow up at very low temperature.

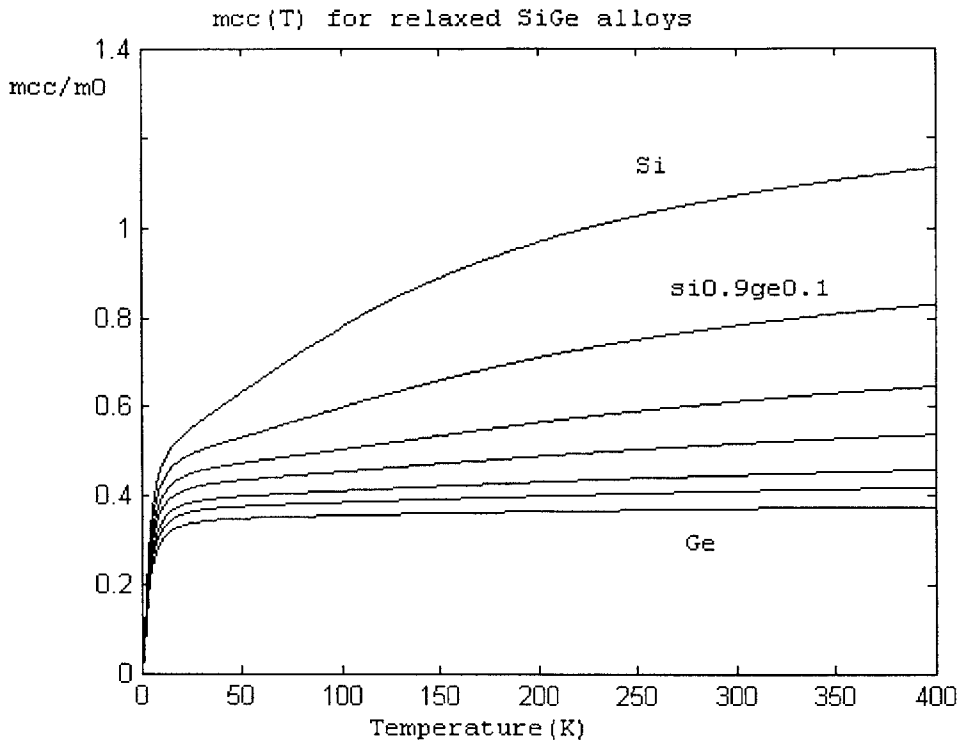

Fig . 2.8. Heavy Hole m_{CC} versus temperature in relaxed Si, $Si_{90\%}Ge_{10\%}$, $Si_{70\%}Ge_{30\%}$, $Si_{50\%}Ge_{50\%}$, $Si_{30\%}Ge_{70\%}$, $Si_{10\%}Ge_{90\%}$, Ge. The order of the graphs is the same as in Fig.2.7.

Fig2.9. shows the energy spectra for Si, $Si_{90\%}Ge_{10\%}$, $Si_{70\%}Ge_{30\%}$, $Si_{50\%}Ge_{50\%}$, $Si_{30\%}Ge_{70\%}$, $Si_{10\%}Ge_{90\%}$, Ge. This is basically the plot of $E(k)$, which can be easily done once one has the function $k^2(E)$.

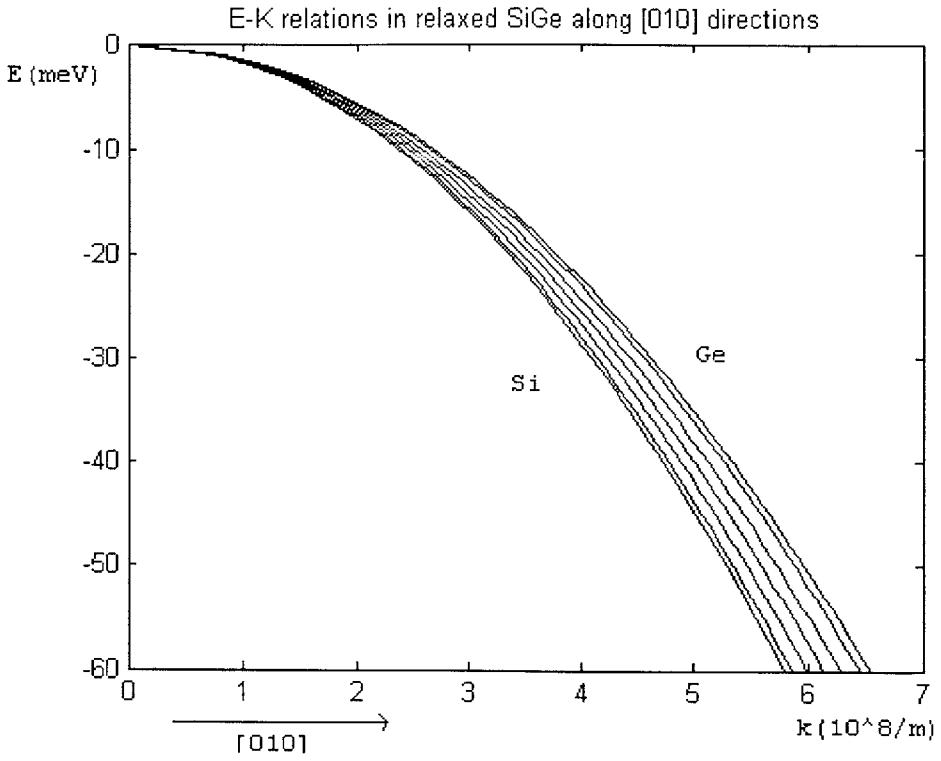

Fig . 2.9. Energy spectrum for heavy holes in relaxed Si, $Si_{90\%}Ge_{10\%}$, $Si_{70\%}Ge_{30\%}$, $Si_{50\%}Ge_{50\%}$, $Si_{30\%}Ge_{70\%}$, $Si_{10\%}Ge_{90\%}$, Ge. As before, $Si_{90\%}Ge_{10\%}$ is closest to silicon, $Si_{10\%}Ge_{90\%}$ is closest to germanium.

Fig.2.10. shows the direct p-s energy gap for Si, $Si_{90\%}Ge_{10\%}$, $Si_{70\%}Ge_{30\%}$, $Si_{50\%}Ge_{50\%}$, $Si_{30\%}Ge_{70\%}$, $Si_{10\%}Ge_{90\%}$, Ge.

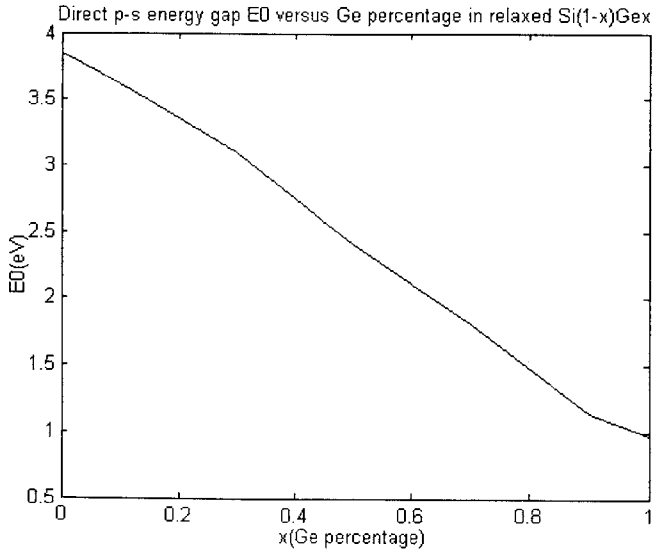

Fig.2.10. Direct p-s energy gap for relaxed Si, $Si_{90\%}Ge_{10\%}$, $Si_{70\%}Ge_{30\%}$, $Si_{50\%}Ge_{50\%}$, $Si_{30\%}Ge_{70\%}$, $Si_{10\%}Ge_{90\%}$, Ge.

Fig.2.11. shows the sigma factor of relaxed Si, $Si_{90\%}Ge_{10\%}$, $Si_{70\%}Ge_{30\%}$, $Si_{50\%}Ge_{50\%}$, $Si_{30\%}Ge_{70\%}$, $Si_{10\%}Ge_{90\%}$, Ge. Sigma factor is $\frac{N}{4}$ where N is the number of electrons that participate in covalent bonding. It can be seen that silicon has about $N = 4$, while germanium has about $N = 5.6$. The deviation from the usual number of 4 covalent electrons, for germanium, is due to the interaction of the existing 4 covalent electrons with other energy bands, which creates the apparent number $N = 5.6$ for covalence.

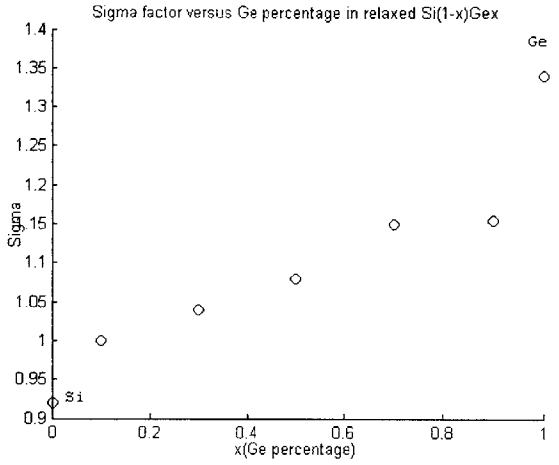

Fig . 2.11. Number of electrons that participate in covalent bonding in relaxed Si, $Si_{90\%}Ge_{10\%}$, $Si_{70\%}Ge_{30\%}$, $Si_{50\%}Ge_{50\%}$, $Si_{30\%}Ge_{70\%}$, $Si_{10\%}Ge_{90\%}$, Ge.

Finally, Fig.2.12. shows the constant energy surfaces for $E = -25meV$. The most outer one is silicon , the most inner one germanium. We can see that even 10% germanium in the SiGe alloy drastically deforms the energy surface from that of silicon.

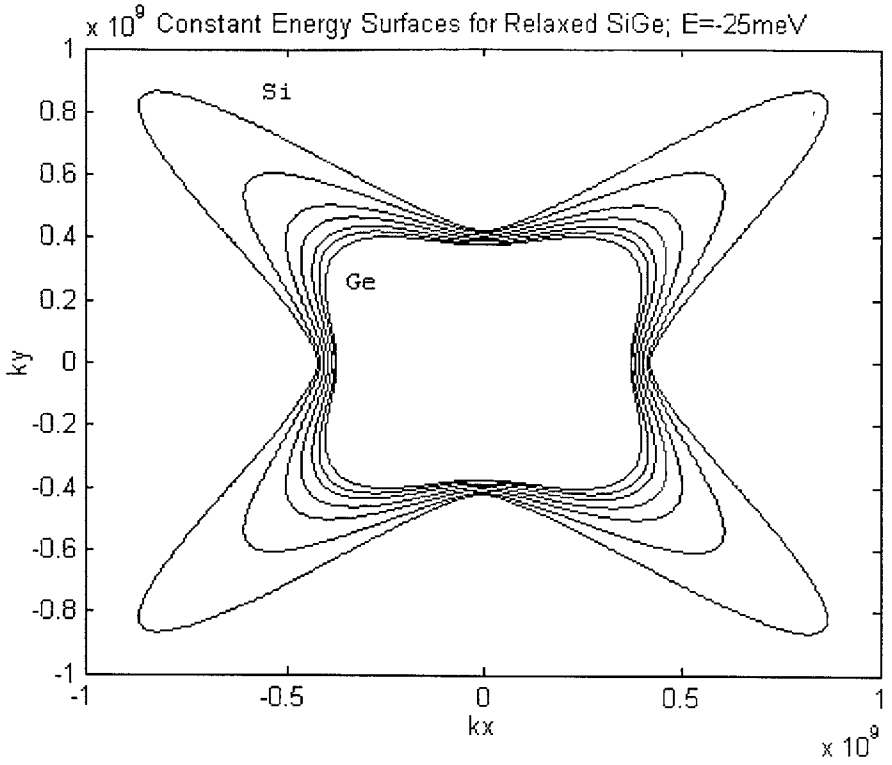

Fig . 2.12. Constant heavy holes energy surfaces ($E = -25meV$) for relaxed Si, $Si_{90\%}Ge_{10\%}$, $Si_{70\%}Ge_{30\%}$, $Si_{50\%}Ge_{50\%}$, $Si_{30\%}Ge_{70\%}$, $Si_{10\%}Ge_{90\%}$, Ge. The relaxed SiGe alloys are in between the Si and Ge energy surfaces, with $Si_{90\%}Ge_{10\%}$ closest to silicon and $Si_{10\%}Ge_{90\%}$ closest to germanium.

The next study is that of strained SiGe. For strained $Si_{1-x}Ge_x$ I used the L, M, N parameters of the relaxed $Si_{1-x}Ge_x$ alloy from the Merkler graph. This was justified by papers [8] and [9], where the L, M, N of strained Si and Ge were experimentally obtained and it turned out they equaled the values for the relaxed Si and Ge respectively, and by the use of L, M, N in paper [4], for example.

Fig.2.13 shows the heavy hole dos mass of strained silicon, where the strained silicon lattice is 1.008 times higher that the unstrained silicon lattice. The value for 25 meV agrees with the 25meV value of Fischetti and Laux [4]. Please compare this graph

with the topmost in Fig.2.7 (unstrained silicon dos mass). Strain always makes the effective mass decrease.

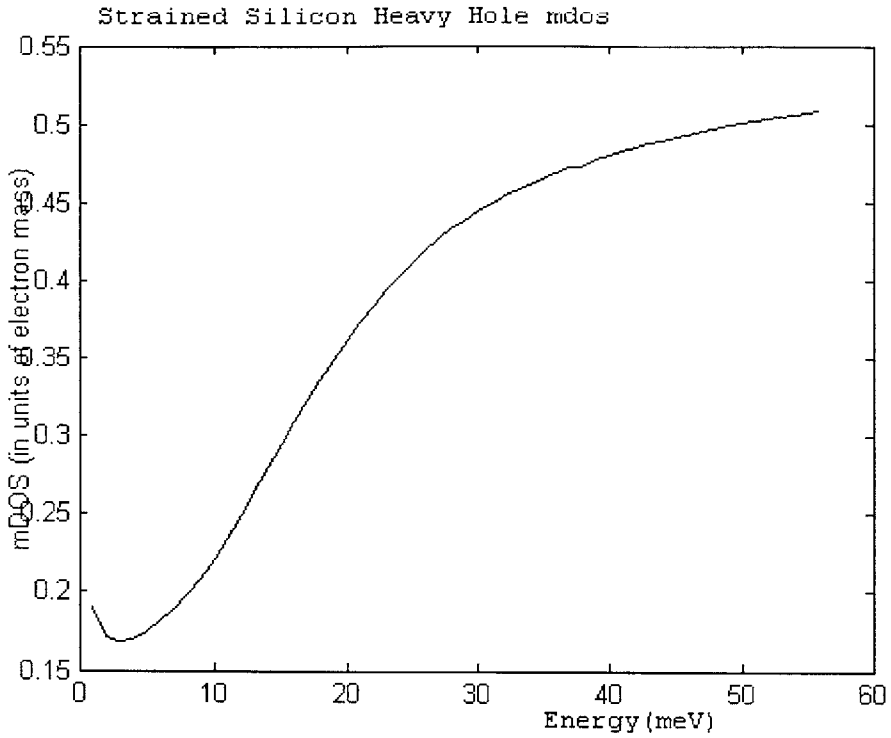

Fig . 2.13. Heavy Hole *mdos* for strained silicon, when grown on a lattice with lattice constant 1.008 times larger than the unstrained silicon lattice.

Fig.2.14. shows the *mdos* at 25meV for various stresses applied to $Si_{50\%}Ge_{50\%}$ At stress 0 the mass is the one for 25meV for $Si_{50\%}Ge_{50\%}$ in Fig.2.7. . We see that as the stress increases (compressive stress), the effective mass drastically decreases until it levels off at a very low value for any higher stress value.

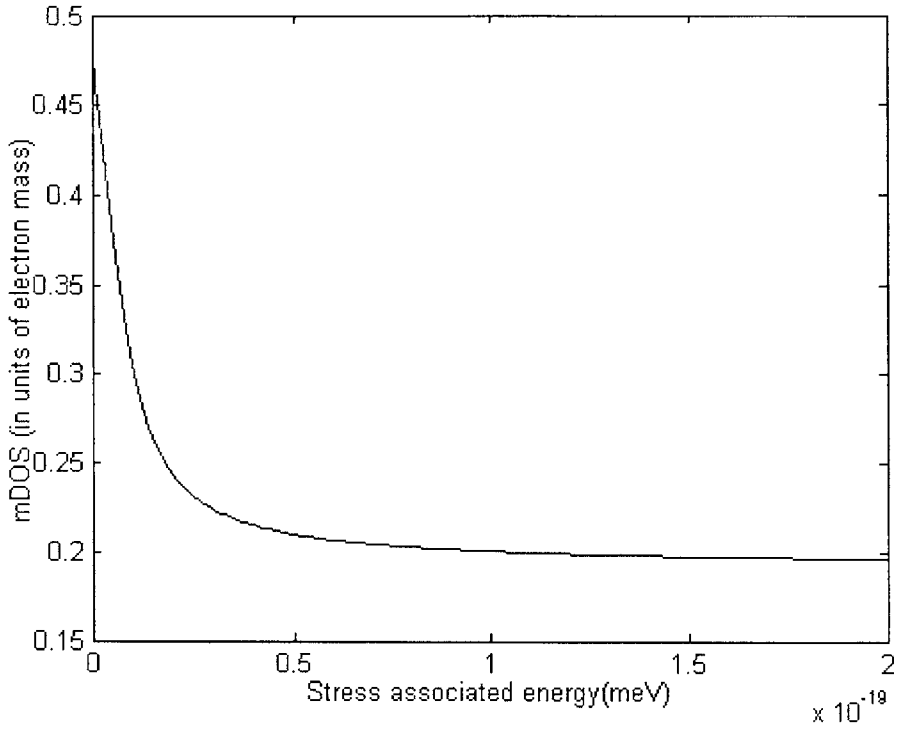

Fig . 2.14. Heavy Hole *mdos* at 25meV for $Si_{50\%}Ge_{50\%}$ for various strains.

Fig.2.15 is very interesting. It shows $mdos(E)$ for relaxed $Si_{50\%}Ge_{50\%}$, for strained $Si_{50\%}Ge_{50\%}$ on relaxed $Si_{70\%}Ge_{30\%}$ (stress 1), for strained $Si_{50\%}Ge_{50\%}$ on relaxed Si (stress2), and for strained $Si_{50\%}Ge_{50\%}$ under a stress 10 times smaller than that on relaxed $Si_{70\%}Ge_{30\%}$ (stress 3, very small stress). It is seen that at low energy the density of states mass approaches the same low value, very different from the unstressed value.

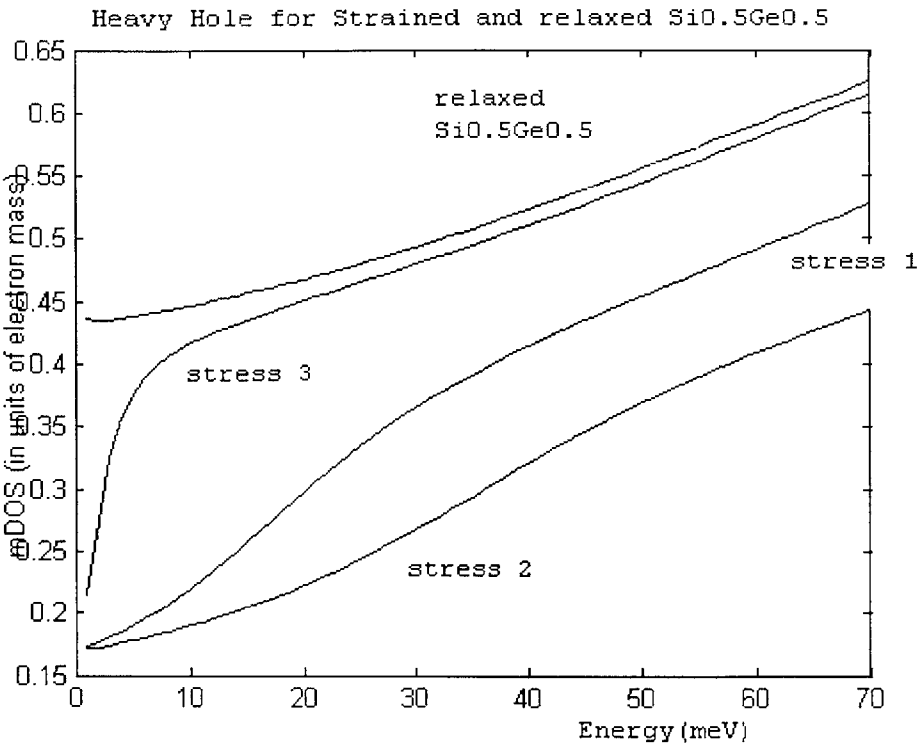

Fig . 2.15. Heavy Hole *mdos(E)* for relaxed $Si_{50\%}Ge_{50\%}$, for strained $Si_{50\%}Ge_{50\%}$ on relaxed $Si_{70\%}Ge_{30\%}$, for strained $Si_{50\%}Ge_{50\%}$ on relaxed Si, and for strained $Si_{50\%}Ge_{50\%}$ under a stress 10 times smaller than that on relaxed $Si_{70\%}Ge_{30\%}$.

Fig.2.16. shows the constant energy surfaces at 25meV for relaxed $Si_{50\%}Ge_{50\%}$, for strained $Si_{50\%}Ge_{50\%}$ on relaxed $Si_{70\%}Ge_{30\%}$, and for strained $Si_{50\%}Ge_{50\%}$ on relaxed Si. The strain is applied along *kz*. We can see that the energy bands retain their unstrained shape in the plane perpendicular to the strain (*ky*), but change drastically in the plane parallel to strain (*kz*).

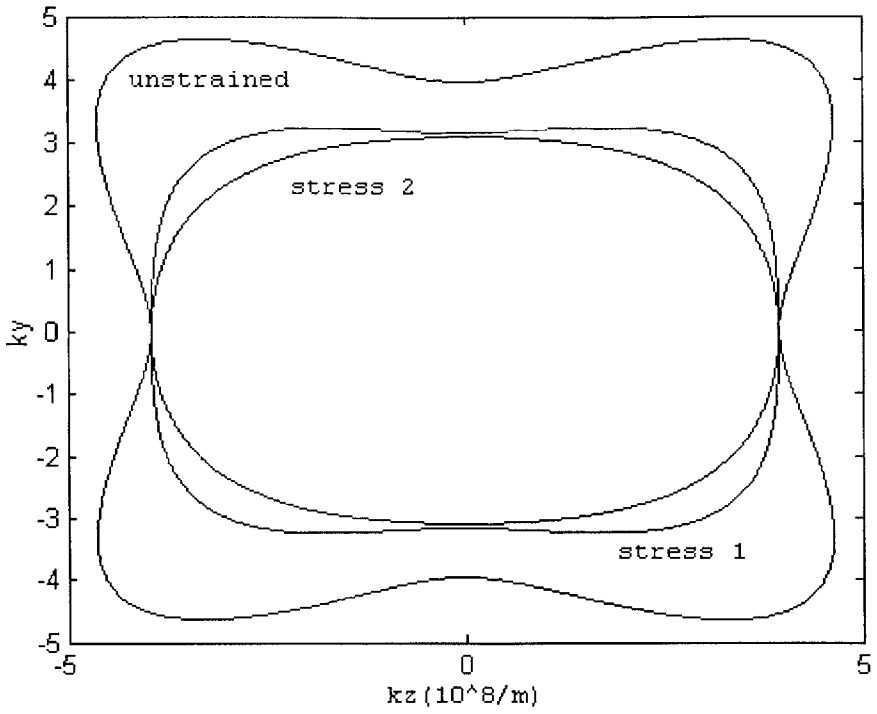

Fig . 2.16. Constant energy surfaces (E=25meV) for heavy hole in relaxed $Si_{50\%}Ge_{50\%}$, for strained $Si_{50\%}Ge_{50\%}$ on relaxed $Si_{70\%}Ge_{30\%}$ (stress1), and for strained $Si_{50\%}Ge_{50\%}$ on relaxed Si (stress 2).

Fig.2.17 is the same as Fig.2.16, but with the unstrained Si and Ge energy surfaces added for comparison.

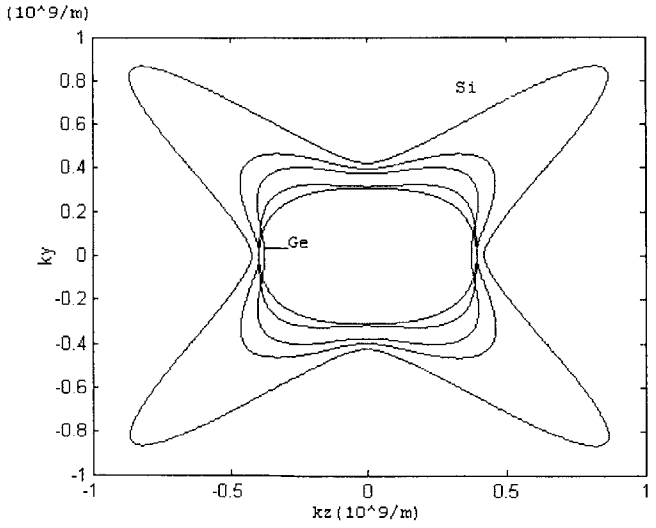

Fig . 2.17. Comparison of the heavy hole constant energy surfaces (E=25meV) for relaxed $Si_{50\%}Ge_{50\%}$, for strained $Si_{50\%}Ge_{50\%}$ on relaxed $Si_{70\%}Ge_{30\%}$, and for strained $Si_{50\%}Ge_{50\%}$ on relaxed Si, with unstrained silicon and germanium energy surfaces.

Appendix A at the end of this work, contains more analysis and graphs related to **Heavy Holes** in relaxed and strained SiGe. Appendix A also contains the similar study as the one done here but for **Light Holes** and for **Split-Off Holes.** The influence of strain on energy band structure and effective masses in Light Holes and Split-Off Holes is thouroughly investigated in **Appendix A.**

Having determined the energy spectrum E(k) of the valence band of each type of hole, the drift mobility can be determined. The formula for drift mobility is [30]:

$$\mu_{ij} = \frac{\frac{q}{\hbar^2}\int d^3k\tau(E)\frac{\partial E}{\partial k_i}\frac{\partial E}{\partial k_j}\frac{\partial f}{\partial E}}{\int d^3k f(E,E_F,T)}$$

where f is the Boltzmann distribution, E_F is the Fermi level, T is the temperature, $\tau(E)$ is the total relaxation time of the holes, and $E(k)$ is the energy spectrum of holes. In the formula above, μ_{ij} are the tensorial components of the mobility tensor.

2.7.5 Conclusion

A general observation is that with more stress, the masses decrease. The effective masses decrease very much the higher the stress, (the effective masses of a crystal can decrease even by a factor of 5 due to stress). It is interesting to notice that the density of states effective masses *mdos* do not depend on temperature. They depend only on energy. The temperature dependence comes in only when the carrier concentration mass is calculated. It is very important to realize then that, when calculating the carrier concentration at other temperatures than the room temperature, we must use a different

mcc and consequently a different Nv in the calculation of p_i. The intrinsic hole carrier concentration p_i will thus decrease significantly due to temperature. However, for electrons, *mcc* does not vary with temperature, and therefore the electron mass that enters Nc in the intrinsic electron carrier concentration n_i is the same at all temperatures.

Chapter 3

Inversion Hole Mobility in Si/SiGe Strained-Layers

3.1 INTRODUCTION

In this chapter strained silicon and strained buried-channel SiGe PMOS devices are studied. These devices were fabricated by Leitz [40],[45], who also measured their mobility at room temperature. I measured the low-temperature mobility of these devices. This chapter presents this data and compares it to the room-temperature data.

Mobility degradation at high effective fields can be observed both at room and low temperatures. The mechanisms that lead to mobility degradation are studied qualitatively and quantitatively. Simulations of these devices in Medici shed new light on the behavior of mobility and permit the determination of individual mobility values for each of the strained layers in the buried-channel PMOS.

3.2 DEVICE TOPOGRAPHY

The devices of Leitz [40] are PMOS ring devices with gate oxide thickness of about 300nm and the topography shown below.

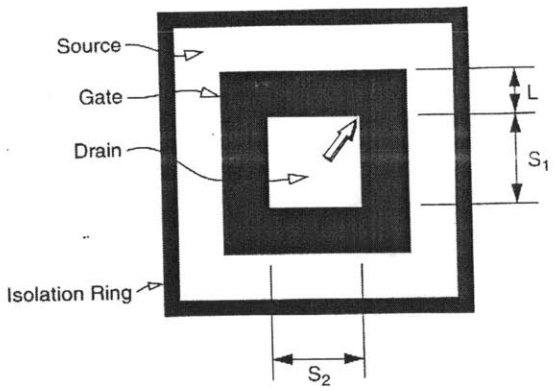

Fig . 3.1. Ring MOSFET mask layout.

The vertical topography of these devices is also shown here.

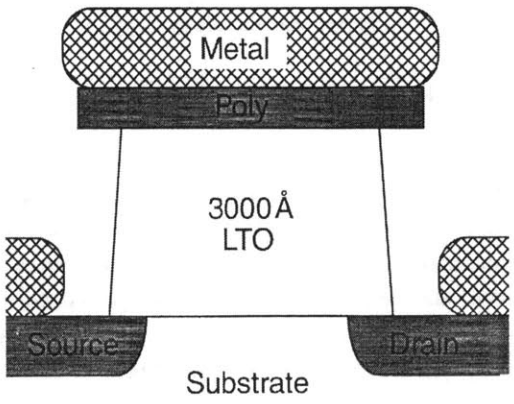

Fig . 3.2. Schematic cross-section of the MOSFET.

Since the only isolation between source/drain and gate is air, high vertical fields (very high voltages) cannot be applied, since they would produce electrical arcs, which would connect the gate to the source/drain.

Device operation is similar to the conventional rectangular FET, with the exception that the channel length is variable along the gate length. The channel is longer

in the corners than on the sides. The dimensions of the devices are $L = 200\mu m$, $S_1 = 250\mu m$, $S_2 = 250\mu m$.

By approximating the inversion layer as a region of uniform sheet resistance bounded by ideal contacts at the source and drains, the resistance between the contacts being given by $R = R_\Delta G$ where R_Δ is the sheet resistance and G is a geometry-dependent value, or "geometry factor". Values for G have been deduced by Matt Currie [41]. For the device with the dimensions given above, the geometry factor is $G = 0.138$.

The current in the linear region of the MOSFET is given by the formula:

$$I_D = \frac{1}{G}\mu_{eff} C_{ox}(V_{GS} - V_T)V_{DS}$$

The composition of the MOSFETS measured was of strained *Si* on relaxed *SiGe* and of strained *Si* on strained *SiGe* on relaxed *SiGe*. The relaxed *SiGe* buffers were grown at 10% $Ge/\mu m$ and capped with a 1.5 μm uniform composition cap. All wafers were grown on 1-20 $\Omega - cm$ n-type substrates and doped $\sim 10^{16} cm^{-3}$ n-type during run. As will be shown later, the actual doping is quite lower than this, due to the low temperature activation of the dopants (*SiGe* relaxes at high temperatures, so low temperatures must be used when processing), and due to uncertainties in the initial doping itself.

The I-V measurements were performed with the following parameters:

- VS= -70V,
- VD= -69.9V,
- VB= -70V,
- VG=100 to -100V.

The biasing of the source, drain and body at –70V is necessary because the HP4145 analyzer only goes to 100V, but our range of interest is larger than that due to the high oxide thickness of the devices. By biasing the body, source and drain negative, VGS is swinging from 30 to –170V, which is the range we need for inversion (negative VGS) in these devices.

3.3 COLD STATION SETUP

The low-temperature current and capacitance characteristics of the devices were measured in a liquid nitrogen cold station. The cold station used in these low-temperature experiments contains four essential system modules:

1. **Purging nitrogen line:** Purging eliminates any impurities and humidity that may be present inside the cold-station.
2. **Liquid nitrogen line:** This serves to cool the wafers.
3. **Vacuum pumps for the probes:** This vacuum pump creates the vacuum necessary to stabilize the probes onto the stage.
4. **Vacuum pump for the chuck:** This vacuum pump creates the vacuum necessary to hold the wafers onto the chuck, for stability during measurements and good backside contact.

3.3.1 Experimental Details

The wafers with the devices to be measured are introduced inside the drybox of the cold-station. These are let to purge overnight by leaving the purging nitrogen line open. The next day the measuring process takes place. The vacuum pumps for the cold-station and the probes are turned on. The devices to be measured are identified on each wafer by row and column.

The liquid nitrogen is let to flow. The liquid nitrogen line runs parallel to the purging nitrogen line, thus cooling the purging nitrogen line, which reaches the chuck and thus cools the chuck. The temperature set point and feedback is provided by a standard temperature controller and a voltage controller. The system works in the following way: when the temperature is still higher than the set-point we want, the heater is inactive and cooling takes place due to the liquid nitrogen which continually flows and cools the chuck. When temperature becomes less that the desired set point, the heater ramps up and heats just enough to bring the temperature back to the set point. An equilibrium is thus established where the temperature is at set point. The wafers need to be taken off the chuck at low temperature to vaporize the nitrogen ice collected on them.

It takes about 20 minutes to reach the temperature of 100K. When the temperature is at about 200K, ice crystals (seen as black points in the microscope) will appear on the surface of the wafer. As the temperature keeps decreasing, the whole surface of the wafer will become covered in ice, making it difficult to see the devices anymore and probe them.

When the desired temperature is reached, the wafer is taken off the chuck and the ice is again blown off it with the house nitrogen gun located inside the drybox. The wafer is then put on the chuck, left there for a few minutes to reach the cold temperature back, and them immediately measured, before ice formation occurs again. If more measurements are necessary, the wafer needs to be lifted every time and the ice blown off it. Ice will tend to form back in about 6 minutes.

3.3.2 Measurement Details

CV and IV measurements are taken with caution by following the right grounding procedure of each. Lack of correct grounding for each type of measurement will lead to a great amount of noise due to the fact that the drybox is not grounded.

3.4 FREEZE-OUT EFFECT

This subchapter discusses the freeze-out effect observed on the C-V curves that were taken for the devices at low temperatures. The figure below shows this effect in the C-V curves of a PMOS device which has a stack of 85 $\mathring{A}$ strained Si / 90 $\mathring{A}$ strained $Si_{0.2}Ge_{0.8}$ on relaxed $Si_{0.5}Ge_{0.5}$. The G_P / ω -V curves corresponding to the C-V curves are also shown.

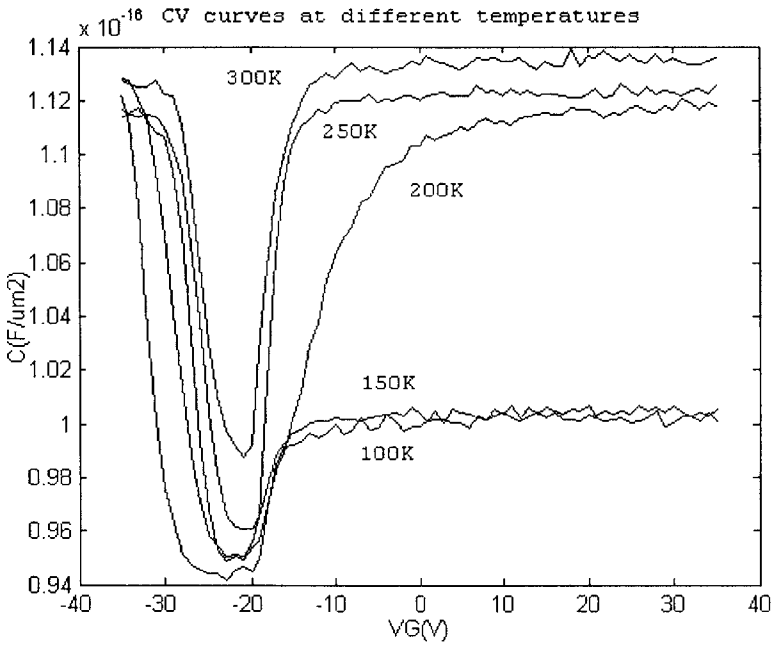

(a)

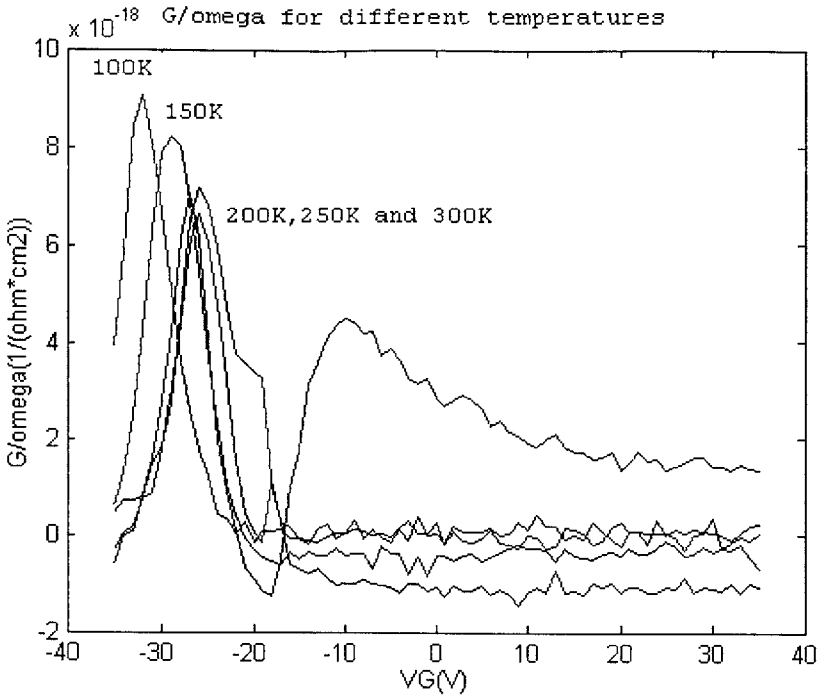

(b)

Fig. 3.3. (a) Full C-V curves at different temperatures for one buried-channel SiGe PMOS device and (b) G_P/ω -V curves corresponding to the C-V curves.

The explanation of the effect seen in the C-V curves is given below.

The response of semiconductor devices to externally applied time-varying voltages is limited by the slow formation of the accumulation region at low temperatures. The time taken for the formation of the accumulation region at low temperatures can be influenced by two time constants [31], [34],[33]:

1. The emission time constant of the dopant atoms[32].
2. The RC time constant of the substrate resistance R_{sub} and capacitances such as the substrate capacitance C_{sub}, the depletion region capacitance C_d and the oxide capacitance C_{ox}, [36].

The slow formation of the accumulation region gives rise to dispersion in the capacitance-voltage (CV) and the conductance-voltage (G-V) characteristics. This

dispersion extends to the accumulation region. Basically, the capacitance in accumulation does not reach C_{ox} but a lower value. This effect decreases with increasing temperature and the constant accumulation capacitance approaches C_{ox} as the temperature approaches 200K.

Since this effect happens in accumulation, we have to look at the flow of carriers in the low-temperature region. In accumulation, it is the majority carriers that flow, and their flow in and out of the semiconductor at room temperature happens with the dielectric relaxation time constant. Since the source and drain are doped with the opposite charge of the majority carriers, the majority carriers get in and out of the semiconductor through the substrate. At low temperatures when freeze-out effects set in, the resistance of the substrate increases. The time constant of the substrate resistance and substrate capacitor is no longer negligible and hence influences the rapidity with which majority carriers flow in and out of the substrate. Similarly the emission time constant of the dopant atoms becomes longer at low temperatures and hence the time taken for the majority carriers to be emitted by the dopant atoms becomes large. Therefore the gate accumulation charge in the surface of the substrate of the MOS device will respond slowly to varying gate voltages at low temperatures due to the fact that majority carriers are not able to flow out readily in and out of the substrate.

The equivalent circuit of the device at temperatures at which freeze-out effects set in is shown below.

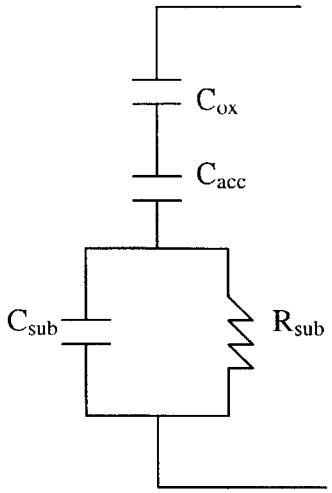

Fig. 3.4. Equivalent circuit of PMOS device at low temperatures.

Freeze-out effects in silicon devices are observed usually at temperatures lower than 100K. Also, the higher the doping, the lower the temperature at which freeze-out effects set in. In SiGe devices, the higher temperatures at which these freeze-out effects are observed (100K, 150K) could be due to the small percentage of dopants that were activated during processing, and to an interaction (absorption) of dopant carriers by the silicon-germanium alloy.

3.5 MOBILITY RESULTS AT LOW TEMPERATURE

C-V and I-V curves were taken for devices at 250K, 200K, 150K and 100K. We did not go much lower than 100K because it was not safe for the machine, as the cooling agent is liquid nitrogen whose temperature is 77K.

3.5.1 Experimental Issues

The IV curves were relatively easy to obtain. Taking C-V's was a more complex matter, as the station has a lot of electrical noise. At small C_{ox} for large oxide thickness, the noise of the cold station is overwhelming. The full C-V at room temperature was

taken at 100kHz with a step voltage of 25mV. It was observed that except for the dummy control silicon wafers, all the other wafers (the *SiGe* wafers) had extremely noisy C-Vs at 100kHz with a step voltage of 25mV. The frequency and the voltage step were varied within limits in which we still have a high frequency measurement and a small enough step voltage.

It was determined that the combination of 25kHz and 200mV voltage step gave the least noisy C-V's. The C-V may still look noisy compared to standard silicon dummy C-V's, but they are fully correct and readable.

3.5.2 Methodology and Results

By applying the simplified mobility extraction algorithm used by Armstrong, Currie and Leitz [39],[41],[40], effective mobility vs. effective field curves for wafers at low temperatures has been obtained. This algorithm is described in Section 3.7.

Below are a few graphs for some of the *SiGe* wafers measured. Additional relevant graphs can be found in Appendix B.

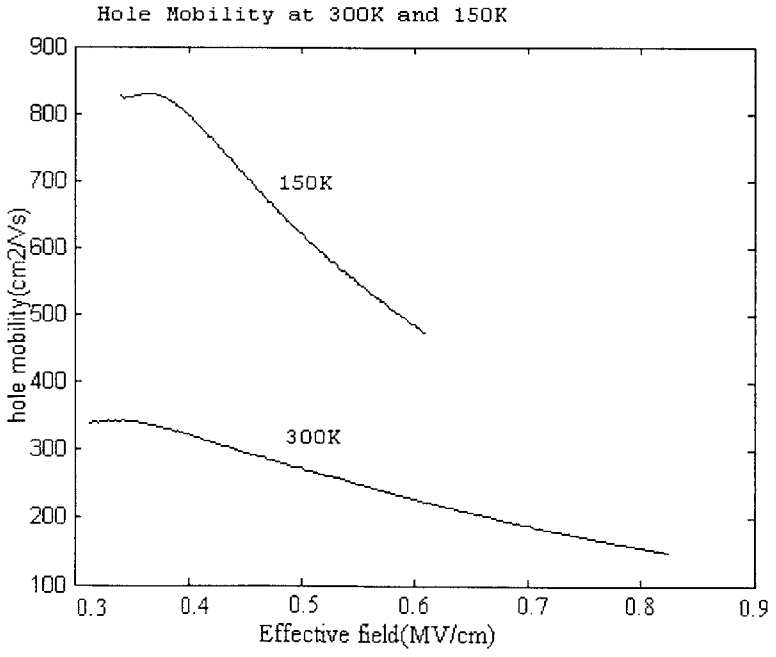

(a)

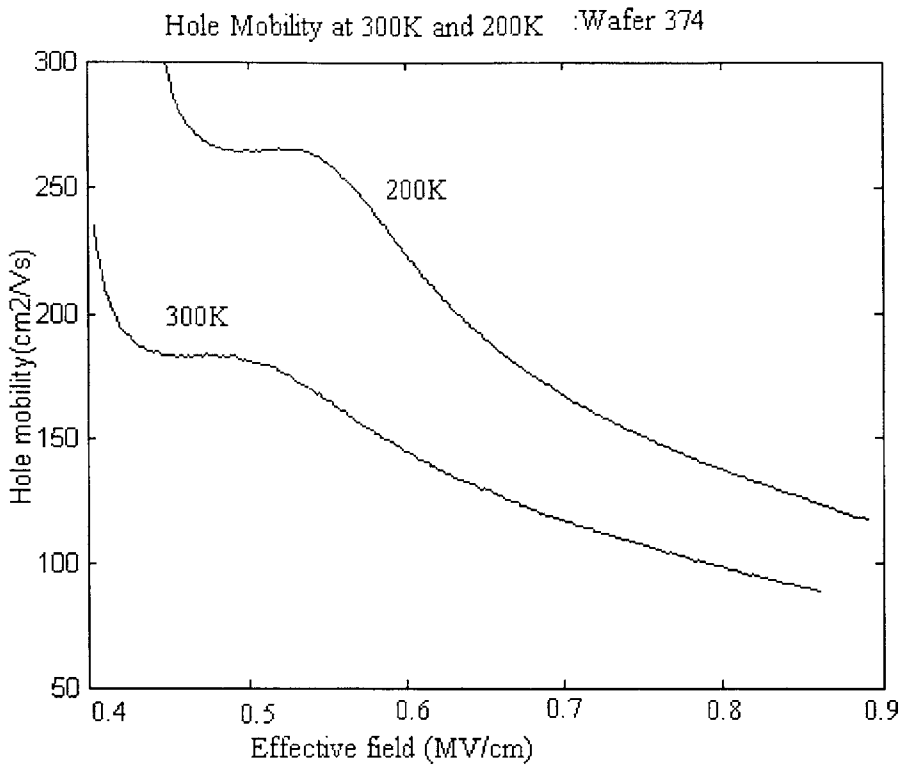

(b)

Fig . 3.5. (a) Mobility at 300K and 150K, of a PMOS device containing a stack of 40 $\mathring{A}$ strained Si / 85 $\mathring{A}$ strained $Si_{0.4}Ge_{0.6}$ on relaxed $Si_{0.7}Ge_{0.3}$. (b) Mobility at 300K and 200K, of a PMOS device containing a stack of 85 $\mathring{A}$ strained Si / 50 $\mathring{A}$ strained $Si_{0.2}Ge_{0.8}$ on relaxed $Si_{0.7}Ge_{0.3}$.

The graphs show the expected result that mobility at low temperature goes up as compared to room temperature. The enhancement factor of mobility is dependent upon temperature.

3.6 EFFECTIVE FIELD DEPENDENCIES FOR MOBILITY IN BURIED CHANNEL SIGE PMOS

The wafers discussed in this section are numbered 370, 371, 372, 374, 391, and have the following compositions:

Wafer# 370 40 $\mathring{A}$ strained Si / 85 $\mathring{A}$ strained $Si_{0.4}Ge_{0.6}$ on relaxed $Si_{0.7}Ge_{0.3}$

Wafer# 371 85 $\mathring{A}$ strained Si / 40 $\mathring{A}$ strained $Si_{0.4}Ge_{0.6}$ on relaxed $Si_{0.7}Ge_{0.3}$

Wafer# 372 40 $\mathring{A}$ strained Si / 40 $\mathring{A}$ strained $Si_{0.4}Ge_{0.6}$ on relaxed $Si_{0.7}Ge_{0.3}$

Wafer# 374 85 $\mathring{A}$ strained Si / 50 $\mathring{A}$ strained $Si_{0.2}Ge_{0.8}$ on relaxed $Si_{0.7}Ge_{0.3}$

Wafer# 391 85 $\mathring{A}$ strained Si / 85 $\mathring{A}$ strained $Si_{0.2}Ge_{0.8}$ on relaxed $Si_{0.5}Ge_{0.5}$

The stack of layers for these PMOS devices is shown in the figure below. The strained silicon region is called *the cap* , the strained SiGe layer is called the *buried channel.*

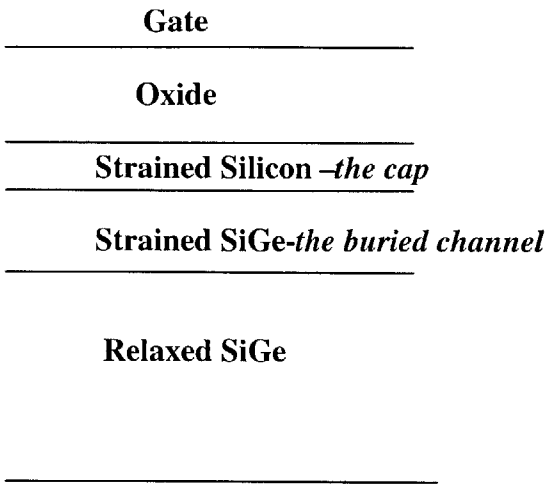

Fig .3.6. Buried-channel SiGe PMOS structure.

Three more wafers have been analyzed, which have only strained Si on relaxed $Si_{0.7}Ge_{0.3}$:

Wafer# 329 40 $\mathring{A}$ strained Si on relaxed $Si_{0.7}Ge_{0.3}$

Wafer# 342 85 $\mathring{A}$ strained Si on relaxed $Si_{0.7}Ge_{0.3}$

Wafer# 346 100 $\mathring{A}$ strained Si on relaxed $Si_{0.5}Ge_{0.5}$

The figure below shows the architecture of these PMOS devices.

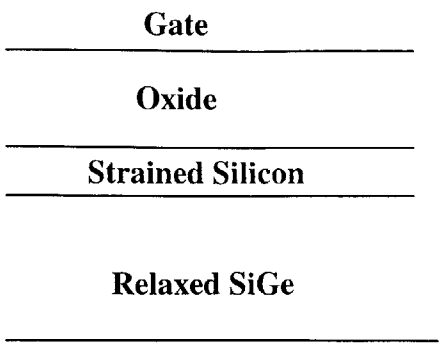

Fig . 3.7. Strained Si PMOS structure.

3.6.1 Effective Mobility at 300K.

Below is a graph of mobility of all five strained *SiGe* wafers (wafer# 370, 371, 372, 374 and 391) at room temperature (300K).

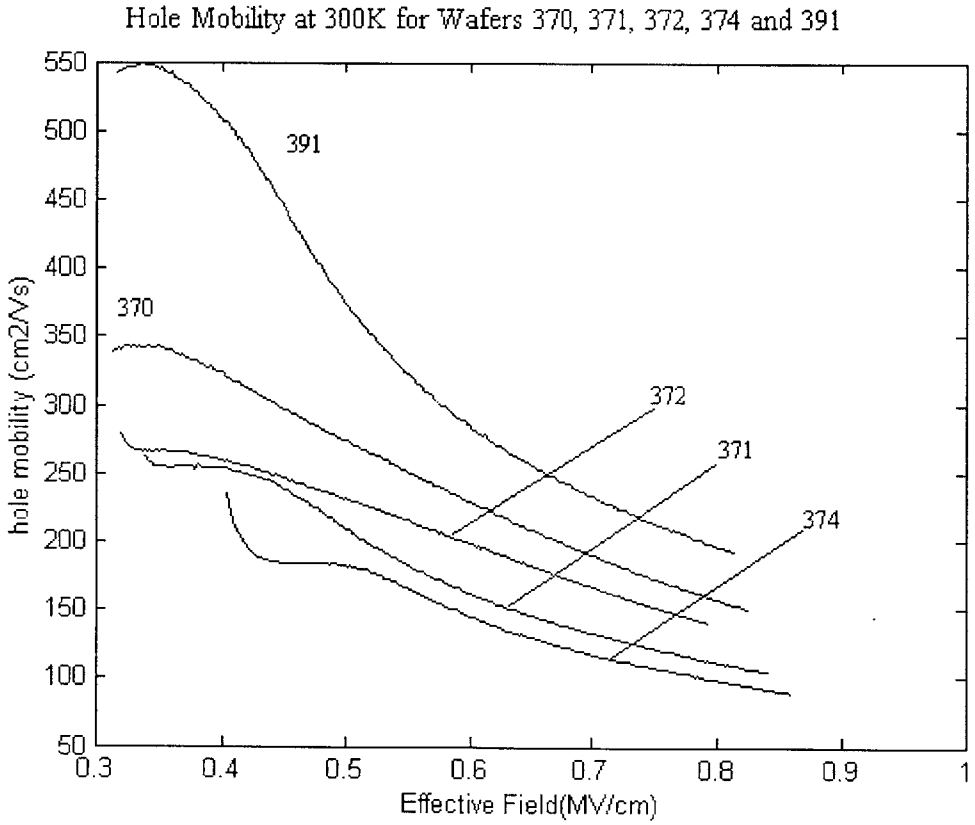

Fig . 3.8. Room-temperature hole mobility versus effective field for buried-channel PMOS devices 370, 371, 372, 374, 391.

We observe the following:

1. The wafer with the largest mobility overall is 391, which has a thick channel and the highest concentration of Germanium in its strained channel ($Si_{0.2}Ge_{0.8}$) among the five wafers.
2. Among the 3 strained $Si_{0.4}Ge_{0.6}$ channel wafers (370, 371, 372), the highest mobility of holes is found on the wafer with the *thickest channel and the thinnest cap* (370).
3. The lowest mobility among these 3 $Si_{0.4}Ge_{0.6}$ buried channel wafers is found in the one with the *thinnest strained channel and thickest cap*, namely wafer#371. Wafer#372 has a higher mobility than wafer# 371 because its cap thickness is smaller than the cap of wafer# 371. Wafer# 372 is lower than wafer# 370 because although their caps are the same thickness, the channel of wafer# 372 is thinner than the channel of wafer# 370.
4. It is clear that the high mobility of the wafers is due to the strained *SiGe* channel. This is because wafer# 329, 342 and 346 have hole mobility much lower than any of the buried channel devices, while having strained *Si* caps of the same thickness as the buried channel devices. To restate, wafers# 329, 342 and 346 have surface channel devices in which no strained *SiGe* is present. Plots of mobilities of these three wafers can be found later in this chapter.

DEDUCED MOBILITY RULES:

The above analysis, leads to the inference of the following mobility rules:

1. ***In the strained SiGe channel, the Ge concentration is directly proportional to hole-mobility. The higher the Ge concentration of the channel, the higher the intrinsic mobility of holes in the channel.***

2. ***The thickness of the strained SiGe channel dictates favorably the number of channel holes. These two are directly proportional to hole mobility. The thicker the channel, the more hole carriers there are in the channel. Similarly, the thicker the strained Si cap, the more hole carriers are in the cap.***
3. ***The strained Si cap always has lower mobility to contribute to the aggregate hole mobility than the strained SiGe channel. Thus the ratio of carriers in the strained Si cap to the number of carriers in the strained SiGe channel (this translates into the ratio of thickness of the two layers), is inversely proportional to mobility.***

Finally, wafer# 374 was found to have the lowest mobility. This is not explained by just the above three laws. Comparing, wafer# 371 and wafer# 374 compositions.

Wafer#371 85 $\mathring{A}$ strained Si / 40 $\mathring{A}$ strained $Si_{0.4}Ge_{0.6}$ on relaxed $Si_{0.7}Ge_{0.3}$

Wafer#374 85 $\mathring{A}$ strained Si / 50 $\mathring{A}$ strained $Si_{0.2}Ge_{0.8}$ on relaxed $Si_{0.7}Ge_{0.3}$

the two wafers have the same Si cap thickness and the same relaxed buffer composition. Wafer# 374 however has higher Ge composition in the strained channel and thicker channel layer! By the above three laws, wafer# 374 should have higher mobility that wafer# 371. Careful and repeated measurements on a number of devices on wafers# 371 and 374 and then the plots of effective mobility versus gate voltage and of mobility versus VGS-VT always show that wafer#371 has higher mobility than wafer#374. This shows that the phenomenon is real. The explanation is that in wafer# 374 the strained $Si_{0.2}Ge_{0.8}$ channel has started to relax. This would degrade the mobility. A natural question arises regarding why wafer# 374 started to relax, and not wafer#391, which also

has a $Si_{0.2}Ge_{0.8}$ channel? The reason probably lies in the relaxed buffer composition. Wafer#391 has a $Si_{0.5}Ge_{0.5}$ relaxed buffer, while wafer#374 has a $Si_{0.7}Ge_{0.3}$ relaxed layer. ***The strain the channel material*** $Si_{0.2}Ge_{0.8}$ ***is subjected to becomes larger with the difference between the Ge percentage of the strained and relaxed layers (which comes from larger difference in lattices),*** and therefore wafer# 374 $Si_{0.2}Ge_{0.8}$ is much more strained that wafer# 391 $Si_{0.2}Ge_{0.8}$.

3.6.2 Effective Mobility at 150K

Below is the effective mobility of wafers# 391, 370, 372, and 371 at 150K. The mobility of the wafers preserves the expected order. Wafer# 391>370>372>371.

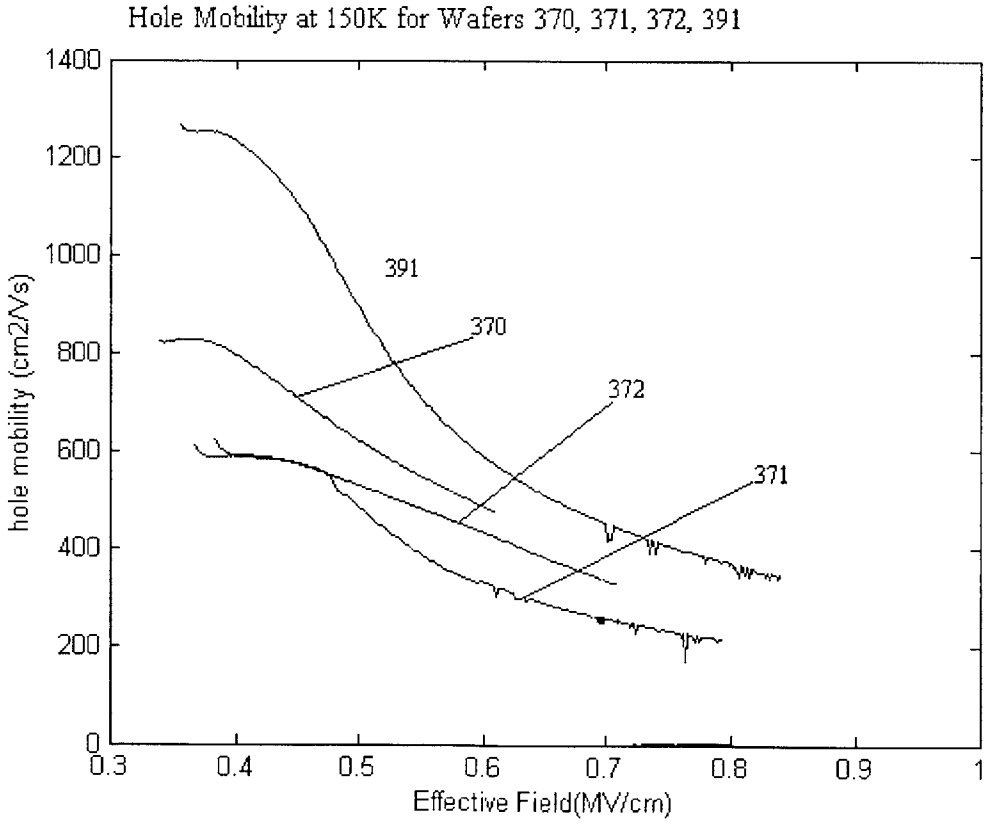

Fig . 3.9. 150K hole mobility versus effective field for buried-channel PMOS devices 370, 371, 372, 391.

The only difference between 371 and 372 wafers is the cap thickness. Everything else is identical. As we will see in a future section, the inversion hole carriers first appear in the buried channel, and later in the strained *Si* cap. After that, the charge in the *Si* cap will start screening the charge in the buried channel, and the charge in the buried channel does not increase anymore. The mobility quickly decreases because it is dominated by carriers in the strained Si cap. This is confirmed by the fact that hole-mobility of wafer#371 and 372 are nearly identical at 300 K with low Effective Fields (when the buried channels, which are identical, dominate), but clearly diverge at higher fields where the higher ratio of cap carriers to channel carriers in the thicker cap of wafer#371 affects stronger that the relatively lower ratio found in wafer# 372. (Rule 3) Hence, the mobility of wafer# 371 decreases a lot compared to wafer#372. At 150K, this phenomenon is even more pronounced. The mobility of wafers is identical at low effective fields, and diverges sharply at higher fields. ***For the buried channel carriers, there is no surface scattering. At room temperature phonon scattering influences the buried channel carriers, but at low temperatures phonon scattering decreases and the mobility of buried channel carriers becomes virtually constant. Thus, at low temperatures the mobility is influenced mainly by surface scattering for the cap carriers.*** The difference in hole-mobility between wafers# 372 and 371 becomes larger at low temperatures and high effective fields. This is because at high effective field mobility is dominated by carriers in the *Si* cap. At room temperature they are influenced by both surface roughness and phonon scattering. However at low temperature only surface roughness matters, and wafer# 372 has fewer strained Si holes to be slowed down by surface scattering (only 40A thickness) than that in wafer#371 (85 A thickness). Also, since wafer#372 has less

screening effect than wafer#371, there will be more buried channel carriers in 372 than in 371. The difference in the hole-mobility of wafers# 371 and 372 at high effective fields and low temperature is starker due to simply the difference in number of carriers in the respective buried channels.

Another observation is that, since at low temperatures the mobility of buried carriers is virtually constant (and equal to each other in the two wafers considered here), the difference in mobility between the two wafers is given solely by the cap carriers. Since the caps are of different thickness, the difference will be very sharp. At room temperature the same difference in cap carrier mobilities apply, but the buried channel carriers contribute by smoothing out the difference due to their also slowly decreasing mobility due to room temperature phonon scattering.

371 85 $\mathring{A}$ strained Si / 40 $\mathring{A}$ strained $Si_{0.4}Ge_{0.6}$ on relaxed $Si_{0.7}Ge_{0.3}$

372 40 $\mathring{A}$ strained Si / 40 $\mathring{A}$ strained $Si_{0.4}Ge_{0.6}$ on relaxed $Si_{0.7}Ge_{0.3}$

Basically, low temperatures will only make the differences in mobility between wafers starker. This is clear also if we look at the difference in mobility between any 2 wafers at 300K and 150K (the difference is always larger at 150K).

3.6.3 Comparison of Mobility at Room and Low Temperatures

For individual wafer comparison at room and low temperatures, below is the graph of hole-mobility of wafer# 372. All the other graphs (for wafers# 370, 371, 374 and 391) are in Appendix B .

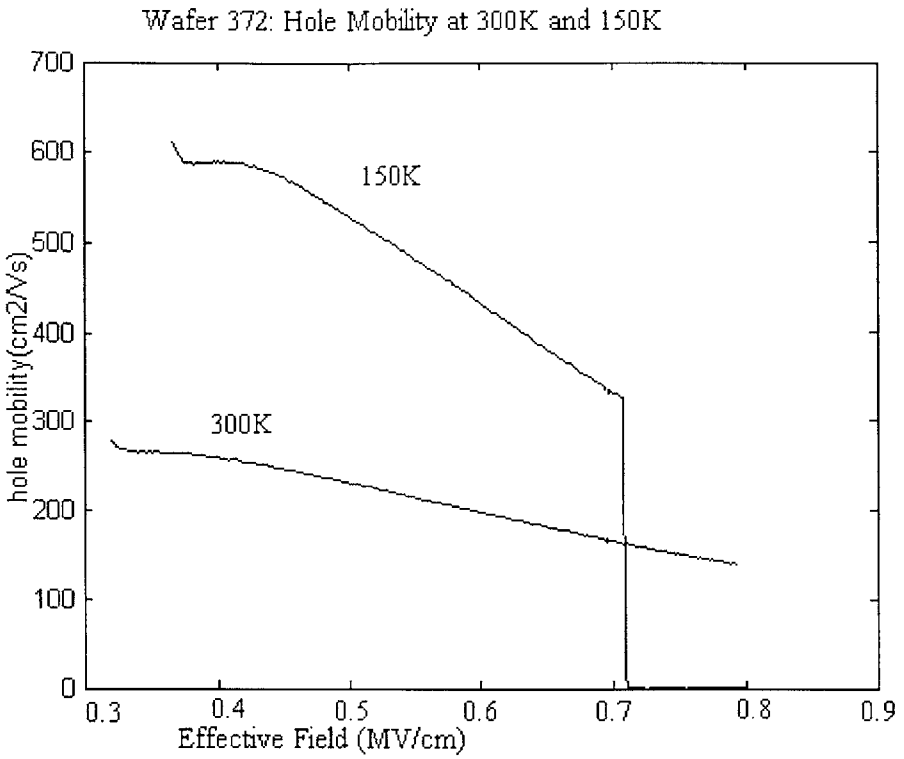

Fig . 3.10. Comparison of hole mobility at room and low temperature for buried-channel device 372. At 150K the device broke down at high effective field.

It is observed that there seems to be a sharp change of slope for mobility at about 0.4MV/cm , due to probably the point where cap carriers start to overwhelm the buried carriers. Doing simulations on Medici for a buried channel PMOS, and plotting the inversion carriers, we obtain the graph below.

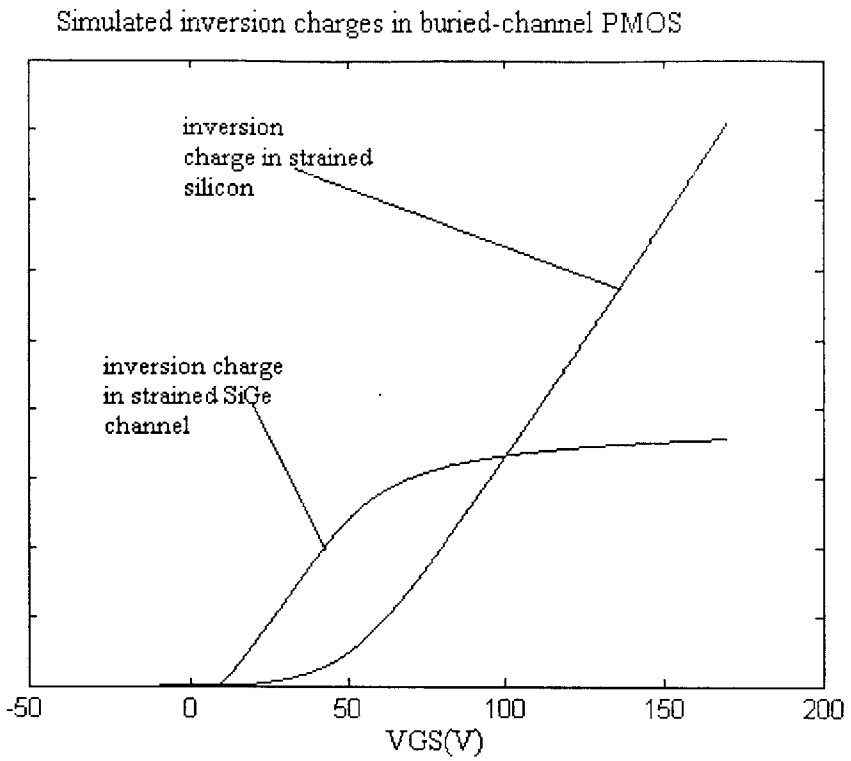

Fig . 3.11. Medici simulation of Inversion charges in buried channel and cap versus gate voltage.

The value of the effective field at the point where the strained silicon carriers start overwhelming the buried channel carriers (about 100V on the graph above) is calculated using the Armstrong formula (described in the next section) and taking into consideration the fixed oxide charge that must be present on order to have the threshold voltage at about 20V as the measured Leitz devices have.

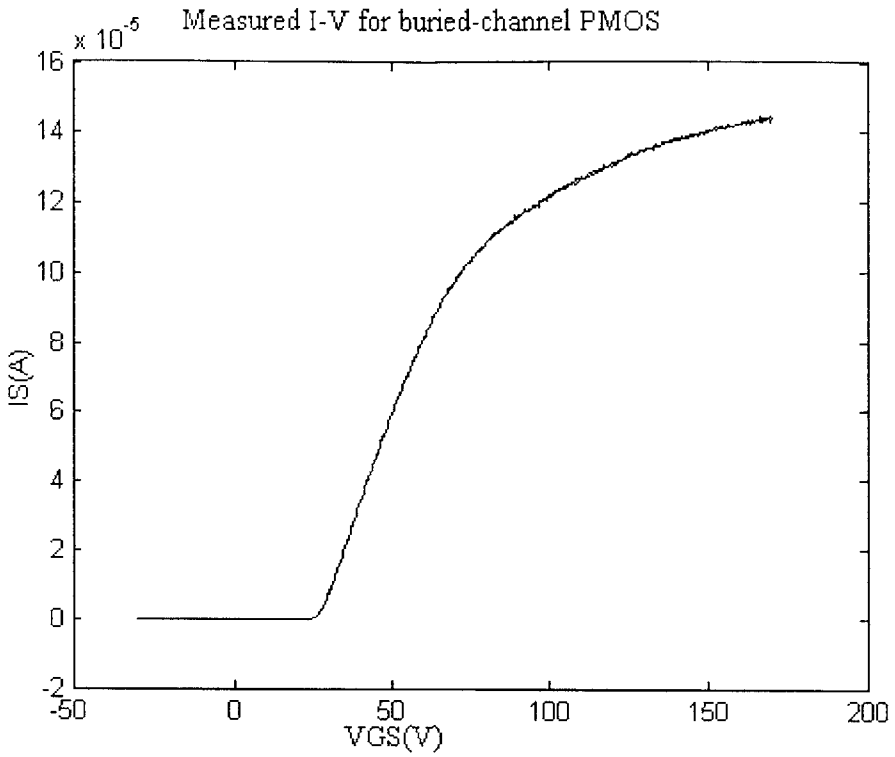

Fig . 3.12. I-V curve of one of the buried channel PMOS devices of Leitz [40].

The value obtained for effective field from this calculation is 0.48MV/cm. Thus we confirm that the change in slope on the mobility graphs does correspond to the cap carriers starting to overwhelm and screen the buried carriers.

3.6.4 Comparison of Buried Channel SiGe PMOS Mobility with Surface Channel Strained Si PMOS Mobility

The following graph shows the hole-mobility of wafers# 370 and 372

370 40 $\mathring{A}$ strained Si / 85 $\mathring{A}$ strained $Si_{0.4}Ge_{0.6}$ on relaxed $Si_{0.7}Ge_{0.3}$

372 40 $\mathring{A}$ strained Si / 40 $\mathring{A}$ strained $Si_{0.4}Ge_{0.6}$ on relaxed $Si_{0.7}Ge_{0.3}$

along with the strained silicon on relaxed $SiGe$ wafer

329 40 $\mathring{A}$ strained Si on relaxed $Si_{0.7}Ge_{0.3}$

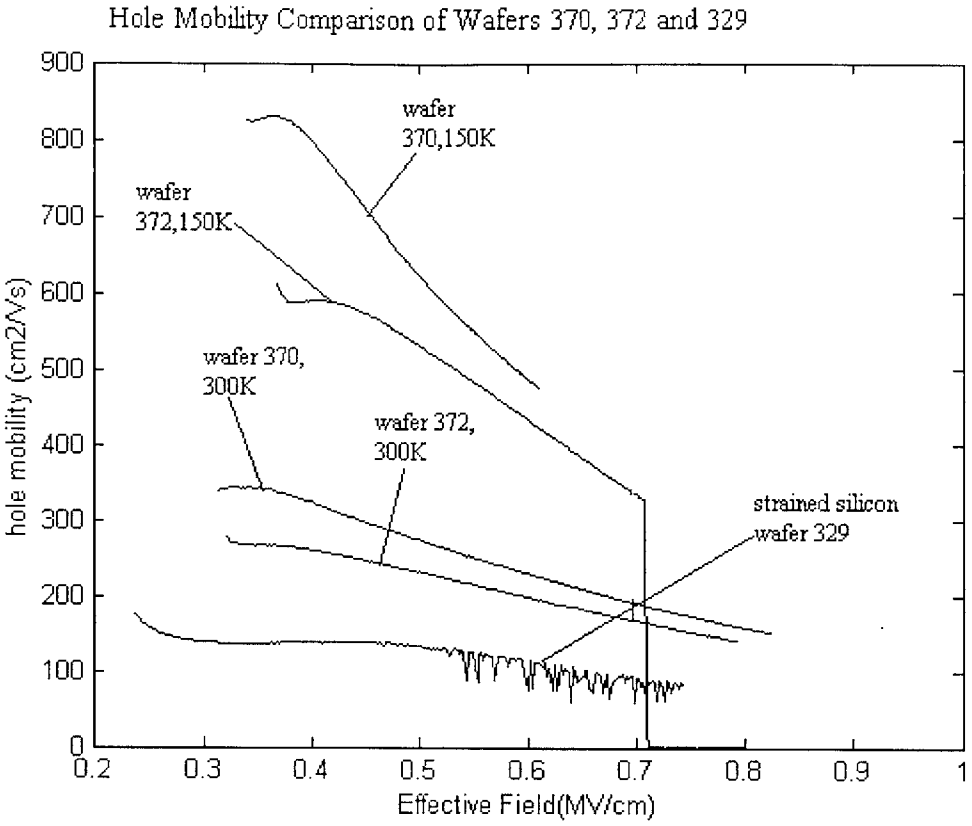

Fig . 3.13. Hole Mobility of devices 370, 372 and 329.

As we can see, these three wafers have the same strained silicon cap thickness. At large effective fields, that is, at large VGS, when the holes in strained *Si* dominate the effective mobility in wafers# 370 and 372, we would expect the mobilities of wafers#370 and 372 to approach the mobility of wafer#329. However this does not happen, and the fact that this does not happen indicates that ***the buried SiGe channel holes in wafers#372 and 370 still have an important influence on the overall mobility, even if they are screened by the cap charge.***

In the following two graphs we see the mobility of wafers# 371 and 374 plotted together with wafer:

342 85 $\mathring{A}$ strained *Si* on relaxed $Si_{0.7}Ge_{0.3}$

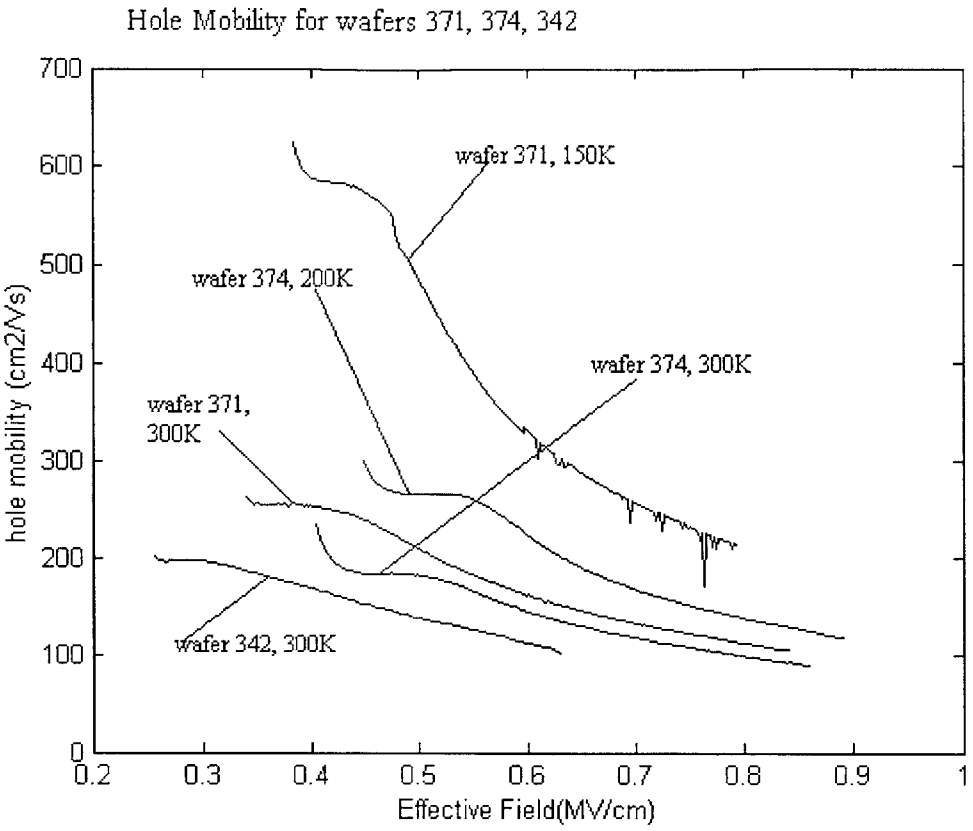

Fig . 3.14. Hole mobility of devices 374, 371 and 342.

Again, the cap thickness of all three wafers is the same. ***It seems that the mobilities of the buried channel devices 371 and 374 approach the mobility of 342 at high fields much more than in the previous graph, which means that the influence of holes from the buried layer is less, which is due to the thicker cap and the thinner buried channel.***

Same discussion applies to the following graph where wafer# 346 mobility is plotted with the mobility of wafer 391 at 300K and 150K.

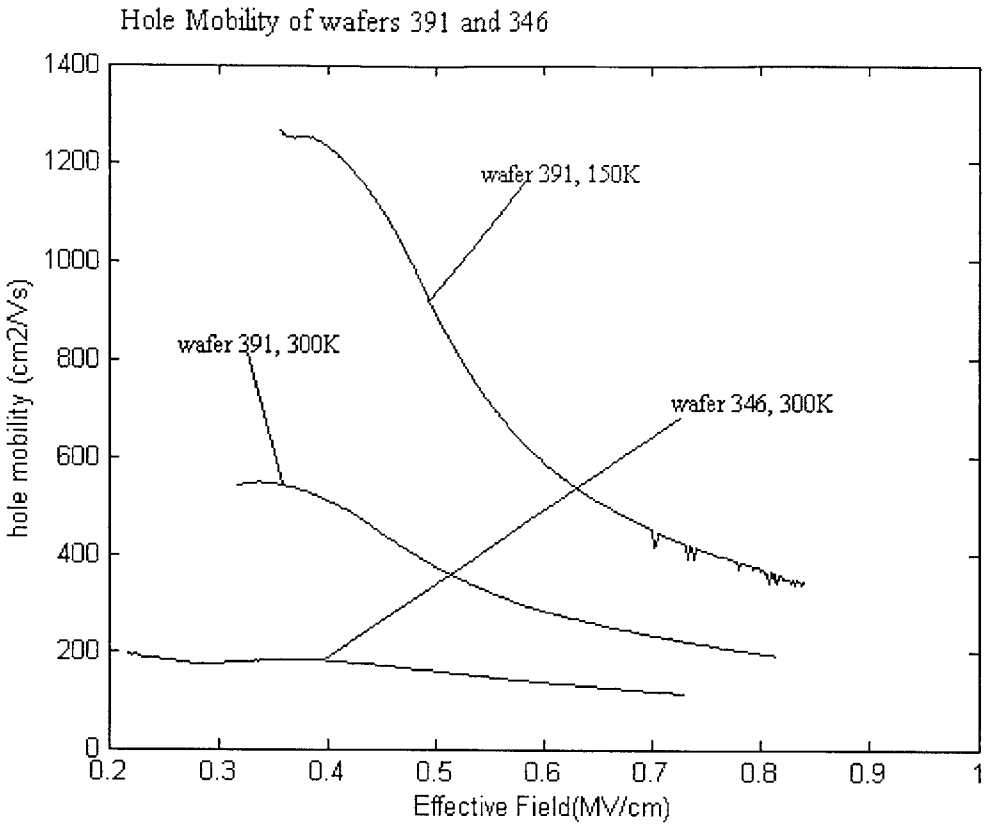

Fig . 3.15. Hole mobility of devices 391 and 346.

3.6.5 Slopes of Mobility Graphs

Great insight into the mechanics of mobility mechanisms is provided by the slope of the mobility/effective field graph. By plotting effective mobility versus effective field in the log-log scale, the slope is obtained. The log-log plots are in Appendix B, and they all have a linear region at higher effective fields. The slopes are taken in this linear regions of the log-log plots, and, also, in cases when the graph is more nonlinear, at a lower effective field in the middle of the nonlinear region.

Below is the list of the slopes obtained. Where there are two values for the same wafer at one temperature, it means that the mobility curve has two regions of different

slopes. Also in the table is the slope of inversion holes in silicon PMOS , from the seminal papers by Takagi [42],[43].

TABLE 3.1

Slopes of mobility curves of PMOS devices

Wafer	Slope at 300K, Holes	Slope at 200K, Holes	Slope at 150K, Holes
370	low field -0.72 high field -1.2		-1.33
371	-1.33		-2.22
372	low field -0.6 high field -1.33		-1.6
374	-1.42	-1.6	
391	-1.42		-2
Silicon	➢ No single power law ➢ Somewhat stronger than –0.3 ➢ Not so abrupt change in slope at high Eeff	Shifts towards -1	Shifts towards -1

3.6.6 Inference from the Results

A few important inferences can be made in the above table. For ease of reference, the compositions of the 5 wafers are listed here below again.

370 40 $\mathring{A}$ strained Si / 85 $\mathring{A}$ strained $Si_{0.4}Ge_{0.6}$ on relaxed $Si_{0.7}Ge_{0.3}$

371 85 $\mathring{A}$ strained Si / 40 $\mathring{A}$ strained $Si_{0.4}Ge_{0.6}$ on relaxed $Si_{0.7}Ge_{0.3}$

372 40 $\mathring{A}$ strained Si / 40 $\mathring{A}$ strained $Si_{0.4}Ge_{0.6}$ on relaxed $Si_{0.7}Ge_{0.3}$

374 85 $\mathring{A}$ strained Si / 50 $\mathring{A}$ strained $Si_{0.2}Ge_{0.8}$ on relaxed $Si_{0.7}Ge_{0.3}$

391 85 $\mathring{A}$ strained Si / 85 $\mathring{A}$ strained $Si_{0.2}Ge_{0.8}$ on relaxed $Si_{0.5}Ge_{0.5}$

The observations are summarized below:

- Wafers #371, 374, 391 all have a reasonably straight graph which has one unique slope; what these three wafers have in common is the thicker 85 $\mathring{A}$ strained silicon cap. We conclude that the unique slope must be related to holes in strained silicon. The slopes of these three wafers are similar: about –1.3 at room temperature and about –2 at 150K. The wafer# 374 slope is in fact at 200K and its value is –1.6, while the 150K slope of the other two wafers is about –2. It seems that the slope of these wafers decreases with temperature, from about –1.3 at room temperature to –1.6 at 200K and further –2 at 150K.
- Wafers 370 and 372 have slopes similar to each other, on regions. These are the two wafers among the 5 studied, which have a thin cap, of thickness 40 $\mathring{A}$. The thinner the cap the lesser the influence from the surface channel there is and the higher the effective field at which the buried channel will be screened. Two kinds of holes have now significant influence, the strained silicon holes and the strained *SiGe* holes. The slope of about –0.7 is related to the buried channel holes, since it applied to lower effective fields, and –1,2 is related to the surface channel.

• The slope of approximately -1.4 (-1.4 or –1.33 , -1.2) , is common to all 5 wafers! This further endorses the fact that the slope of –1.4 is related to the surface strained silicon holes, because this slope always applies to higher fields (and for 3 of the wafers, to lower fields as well).

• We conclude that when only one slope appears in the mobility graph, the influence of only one kind of holes is important (the cap holes); when two slopes appear, the influence of buried channel carriers is felt at low fields and of surface channel carriers at high fields.

The table below summarizes the behavior of each type of holes and the mechanisms that influence it.

TABLE 3.2

Mechanisms that degrade mobility in SiGe PMOS devices

Mobility Component	Surface Channel (strained Si) Holes Mobility Slope	Buried Channel (strained SiGe) Holes Mobility Slope
300K	-1.4 (due to phonon scattering)	-0.7 (due to phonon scattering)
150K	-2 (due to surface scattering)	should be just about constant
Phonon scattering, 300K	strong	strong
Phonon scattering, 150K	Weak	Weak
Surface scattering, 300K	weak at low Eeff strong at high Eeff	Absent
Surface scattering, 150K	weak at low Eeff strong at high Eeff	absent

The decrease in mobility at low temperatures is due to the holes in the strained silicon cap which are subjected to surface scattering (phonon scattering is weak at low temperatures). The power of the surface scattering for the strained silicon holes

should then be about –2, which is what we see for the slope of wafer# 371 and 391 with thick caps (85A) where the cap carriers dominate.

The reason the slope at low temperatures for wafer# 370 and 372 wafers is not –2 is because in these wafers, the cap is thin (40A), so the buried channel carriers have a stronger influence, so the slope we see is a strong mix of buried and surface channel mobilities. This is also confirmed by the fact that at low temperatures, the smallest absolute slope (the least degradation of mobility with effective field) is seen for wafer# 370 where the channel is the thickest and the cap is the thinnest, so the buried holes strongly sustain the mobility at the initial higher value. The slope get larger for wafer# 372 (-1.6) because more degradation starts occurring (less channel thickness), and finally the slope gets really large (a lot of degradation) for wafer# 371 and 391 (-2) where the buried channel holes are overwhelmed by the many carriers in the thick silicon cap whose mobility degrades fast due to surface scattering. We can even see that wafer#371 (slope –2.2) degrades more that wafer#391 (slope –2), because 391 has a thicker and more strained channel, so the buried carriers have more of an influence that they do in 371.

371 85 $\mathring{A}$ strained Si / 40 $\mathring{A}$ strained $Si_{0.4}Ge_{0.6}$ on relaxed $Si_{0.7}Ge_{0.3}$

391 85 $\mathring{A}$ strained Si / 85 $\mathring{A}$ strained $Si_{0.2}Ge_{0.8}$ on relaxed $Si_{0.5}Ge_{0.5}$

So, in conclusion, strong degradation of mobility with effective field signals the effect of surface channel carriers. Less degradation of mobility with effective field signals the effect of buried channel carriers.

3.7 MOBILITY EXTRACTION BY ARMSTRONG METHOD

This method for extracting mobility has been described by Armstrong [39]. The effective mobility was extracted from the I-V and the C-V experimental data by a simplified analysis. As described before, the drain current of the ring MOS device is

$$I_D = G^{-1}\mu_{eff}C_{ox}(V_{GS} - V_T)V_{DS}$$

where

G is the geometry factor.

To obtain μ_{eff} form the above equation one needs the oxide thickness and the threshold voltage. The threshold voltage is found from the I-V curve at the point where the conductance $\frac{\partial I_D}{\partial V_{GS}}$ is has the maximum value. The oxide thickness is found from the accumulation capacitance in the C-V measurement.

$$\mu_{eff} = \frac{I_D G}{C_{ox}(V_{GS} - V_T)V_{DS}}$$

The effective field is also, in a simplified formula that treats the device as a one-inversion layer device:

$$E_{eff} = \frac{Q_b + \frac{1}{3}Q_{inv}}{\varepsilon_S}$$

Because the doping of the substrate is not accurately known, $N_d x_{d,\max}$ approximation for Q_b is not appropriate. Instead, dielectric continuity at the semiconductor/oxide interface is used to express bulk charge:

$$Q_b + Q_{inv} = E_s\varepsilon_s = E_{ox}\varepsilon_{ox} = \frac{V_{GS}}{t_{ox}}\varepsilon_{ox} = V_{GS}C_{ox}$$

because

$$E_{ox} = \frac{V_{GS}}{t_{ox}} \text{ when } V_{DS} << V_{GS},$$

which is true in our case of $V_{DS} = 100mV$ and V_{GS} from 0 to 170V.

Since $Q_{inv} = C_{ox}(V_{GS} - V_T)$, from the above expression the bulk charge is extracted

$$Q_b = V_T C_{ox}.$$

Therefore, the effective field will be:

$$E_{eff} = \frac{C_{ox}(V_T + \frac{1}{3}(V_{GS} - V_T))}{\varepsilon_S}$$

To obtain mobility graphs, μ_{eff} is plotted vs. E_{eff}.

3.8 EFFECTIVE FIELD THEORY IN HETEROSTRUCTURES

We will now show how to calculate the effective fields for holes in each of the inversion layers formed in the strained *Si* devices and the buried channel devices.

3.8.1 Strained Silicon PMOS

Consider the device below which has a strained layer of silicon grown on a relaxed SiGe buffer.

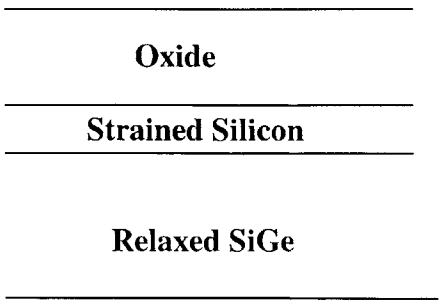

Fig . 3.16. Gate stack of Strained Si on Relaxed SiGe PMOS. The Silicon is strained by the relaxed SiGe layer below.

The band offsets of the hetero-structure are as drawn below.

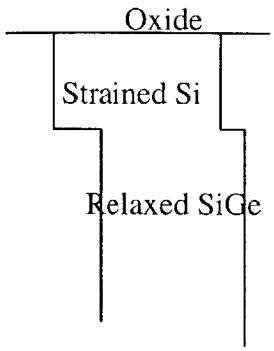

Fig . 3.17. Band offsets of the Strained silicon on Relaxed SiGe shown above at V_G=0Volts.

Because of the band offsets arrangement, inversion holes will first appear in the relaxed SiGe. At sufficiently high gate voltages, inversion holes will appear in the strained *Si* as well. We will then have two layers of inversion charge , one in strained Si and another in relaxed SiGe. Electrostatically, the situation is shown below.

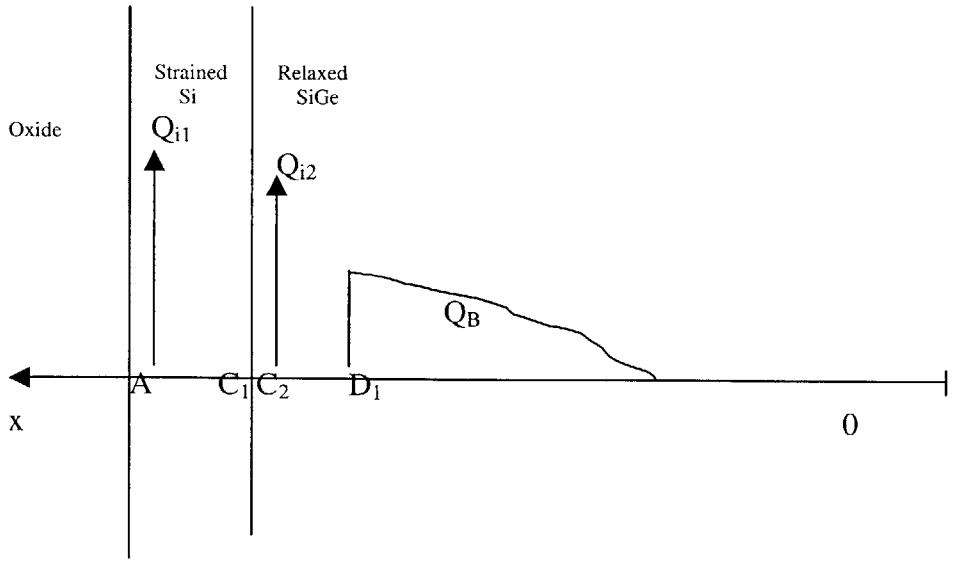

Fig . 3.18. Electrostatic situation in the strained Si on relaxed SiGe PMOS.

Q_{i1} and Q_{i2} are the inversion charges in the strained silicon and relaxed *SiGe* respectively, and Q_B is the bulk charge.

We want to find out formulas for effective fields for holes in each of the inversion layers. By writing Gauss law, and taking into consideration that the electric field is zero x=0, we have:

$$\varepsilon_{si} E_A = Q_B + Q_{i1} + Q_{i2} \text{ which gives } E_A = \frac{Q_B + Q_{i1} + Q_{i2}}{\varepsilon_{si}}$$

and,

$$\varepsilon_{si} E_{C1} = Q_B + Q_{i2} \text{ which gives } E_{C1} = \frac{Q_B + Q_{i2}}{\varepsilon_{si}}$$

$E_A \& E_{C1}$ are the electric fields just above and just below the strained silicon inversion layer, and ε_{si} is the permittivity of the strained silicon layer.

The effective field to which the strained silicon inversion layer is subjected is [Tsividis, ref. 47] the average of these two fields:

$$E_{eff1} = \frac{E_A + E_{C1}}{2},$$

so

$$E_{eff1} = \frac{E_A + E_{C1}}{2} = \frac{1}{2} \frac{2Q_B + 2Q_{i2} + Q_{i1}}{\varepsilon_{si}} = \frac{Q_B + Q_{i2} + \frac{1}{2} Q_{i1}}{\varepsilon_{si}}$$

The $\frac{1}{2}$ coefficient applies to electrons, and to obtain the final hole formula $\frac{1}{2}$ must be replaced by $\frac{1}{3}$ [6].

$$E_{eff1} = \frac{Q_B + Q_{i2} + \frac{1}{3}Q_{i1}}{\varepsilon_{si}}$$

The same analysis is done for the inversion charge in the relaxed layer:

$$\varepsilon_{sige} E_{C2} = Q_B + Q_{i2} \text{ which gives } E_{C2} = \frac{Q_B + Q_{i2}}{\varepsilon_{sige}}$$

and

$$\varepsilon_{sige} E_{D1} = Q_B \text{ which gives } E_{D1} = \frac{Q_B}{\varepsilon_{sige}}$$

E_{C2} and E_{D1} are the electric fields just above and just below the relaxed *SiGe* inversion layer,

ε_{sige} is the permittivity of the relaxed *SiGe* layer.

The effective field to which the strained silicon inversion layer is subjected is the average of these two fields:

$$E_{eff2} = \frac{E_{C2} + E_{D1}}{2} = \frac{1}{2}\frac{2Q_B + Q_{i2}}{\varepsilon_{sige}} = \frac{Q_B + \frac{1}{2}Q_{i2}}{\varepsilon_{sige}}$$

This formula applies to electrons. The hole formula has $\frac{1}{2}$ replaced by $\frac{1}{3}$ [6].

$$E_{eff2} = \frac{Q_B + \frac{1}{3}Q_{i2}}{\varepsilon_{sige}}$$

To obtain the bulk charge Q_B we use dielectric continuity at semiconductor/oxide interface:

$$Q_B + Q_{i1} + Q_{i2} = E_s \varepsilon_{si} = E_A \varepsilon_{si} = E_{ox} \varepsilon_{ox} = \frac{V_{GS}}{t_{ox}} \varepsilon_{ox} = V_{GS} C_{ox}$$

Consequently $Q_B = V_{GS}C_{ox} - Q_{i1} - Q_{i2}$. Plugging this in the expressions for E_{eff1} and E_{eff2}, we obtain finally

$$E_{eff1} = \frac{Q_B + Q_{i2} + \frac{1}{3}Q_{i1}}{\varepsilon_{si}} = \frac{(V_{GS}C_{ox} - Q_{i1} - Q_{i2}) + Q_{i2} + \frac{1}{3}Q_{i1}}{\varepsilon_{si}} = \frac{V_{GS}C_{ox} - Q_{i1} + \frac{1}{3}Q_{i1}}{\varepsilon_{si}} = \frac{V_{GS}C_{ox} - \frac{2}{3}Q_{i1}}{\varepsilon_{si}}$$

$$E_{eff2} = \frac{Q_B + \frac{1}{3}Q_{i2}}{\varepsilon_{sige}} = \frac{(V_{GS}C_{ox} - Q_{i1} - Q_{i2}) + \frac{1}{3}Q_{i2}}{\varepsilon_{sige}} = \frac{V_{GS}C_{ox} - Q_{i1} - \frac{2}{3}Q_{i2}}{\varepsilon_{sige}}$$

In conclusion:

$$E_{eff1} = \frac{V_{GS}C_{ox} - \frac{2}{3}Q_{i1}}{\varepsilon_{si}}$$

$$E_{eff2} = \frac{V_{GS}C_{ox} - Q_{i1} - \frac{2}{3}Q_{i2}}{\varepsilon_{sige}}$$

3.8.2 Buried-Channel PMOS

By the same analysis, in the case of a buried channel device, where the band offsets are as below and thus give rise to three inversion layers at sufficiently high gate voltages, the respective effective fields are:

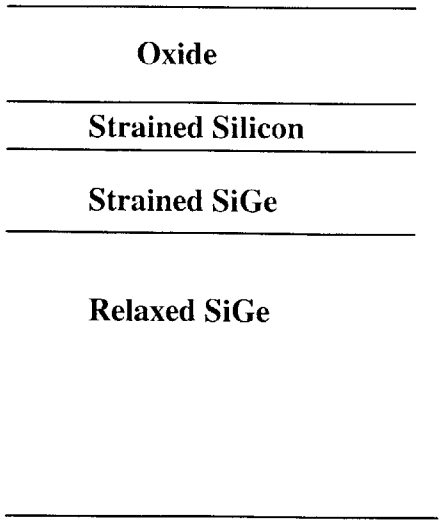

(a)

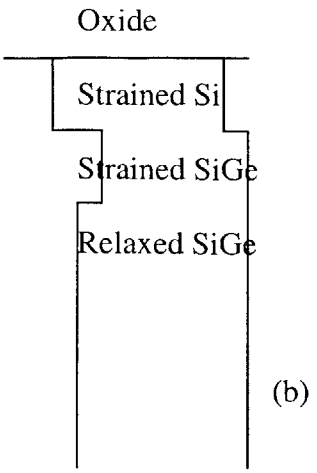

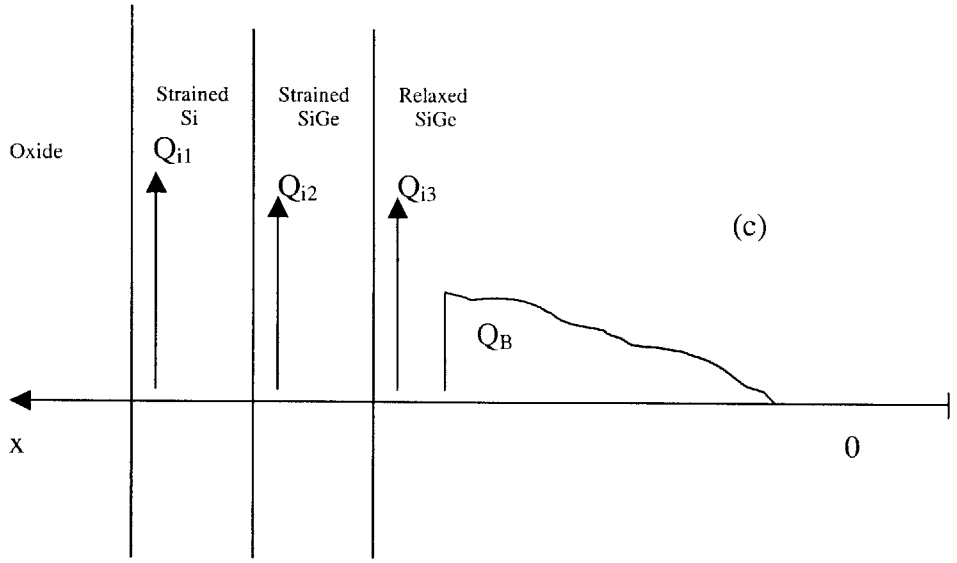

Fig . 3.19. (a) Gate stack of Strained Si/Strained SiGe/Relaxed SiGe PMOS. The very thin layers of silicon and strained SiGe are strained by the relaxed SiGe layer below.(b) Band offsets of Strained Si/Strained SiGe/Relaxed SiGe PMOS at V_G=0Volts (c) Electrostatic situation in the Strained Si/Strained SiGe/Relaxed SiGe PMOS.

$$E_{eff1} = \frac{Q_B + Q_{i2} + Q_{i3} + \frac{1}{3}Q_{i1}}{\varepsilon_{si}} = \frac{(V_{gs}C_{ox} - Q_{i1} - Q_{i2} - Q_{i3}) + Q_{i2} + Q_{i3} + \frac{1}{3}Q_{i1}}{\varepsilon_{si}} =$$

$$= \frac{V_{gs}C_{ox} - \frac{2}{3}Q_{i1}}{\varepsilon_{si}}$$

$$E_{eff2} = \frac{Q_B + Q_{i3} + \frac{1}{3}Q_{i2}}{\varepsilon_{sigestrained}} = \frac{(V_{gs}C_{ox} - Q_{i1} - Q_{i2} - Q_{i3}) + Q_{i3} + \frac{1}{3}Q_{i2}}{\varepsilon_{sigestrained}} =$$

$$= \frac{V_{gs}C_{ox} - Q_{i1} - \frac{2}{3}Q_{i2}}{\varepsilon_{sigestrained}}$$

$$E_{eff3} = \frac{Q_B + \frac{1}{3}Q_{i3}}{\varepsilon_{sigerelaxed}} = \frac{(V_{gs}C_{ox} - Q_{i1} - Q_{i2} - Q_{i3}) + \frac{1}{3}Q_{i3}}{\varepsilon_{sigerelaxed}} =$$

$$= \frac{V_{gs}C_{ox} - Q_{i1} - Q_{i2} - \frac{2}{3}Q_{i3}}{\varepsilon_{sigerelaxed}}$$

3.8.3 The Influence of Fixed Oxide Charge

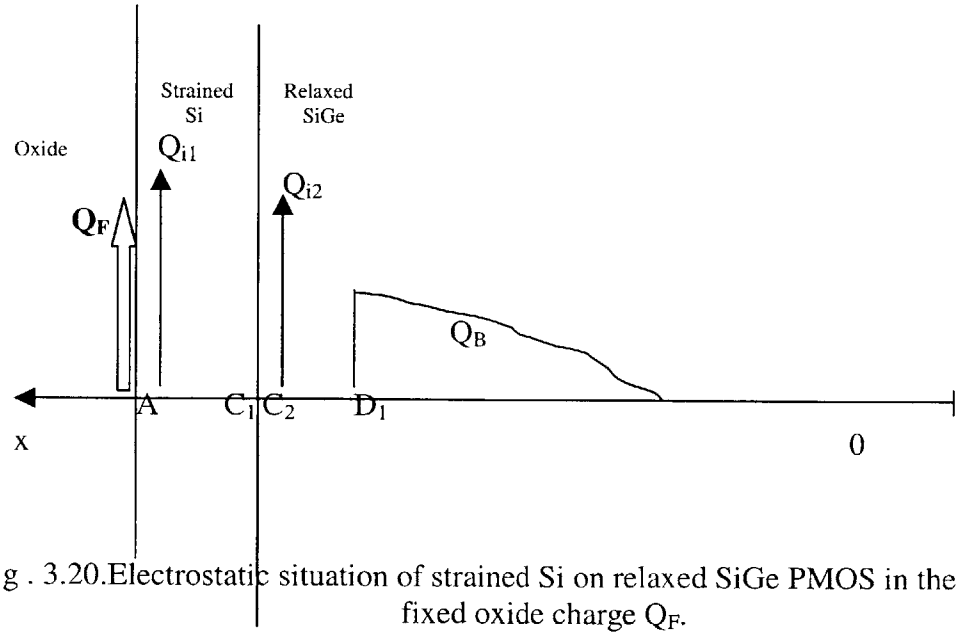

Fig . 3.20.Electrostatic situation of strained Si on relaxed SiGe PMOS in the presence of fixed oxide charge Q_F.

If fixed oxide charge is present at the oxide/semiconductor interface, then

$$Q_B + Q_{i1} + Q_{i2} = E_s\varepsilon_{si}$$

$$E_{ox}\varepsilon_{ox} = \frac{V_{GS}}{t_{ox}}\varepsilon_{ox} = V_{GS}C_{ox} \text{ for low } V_{DS}$$

$$E_s\varepsilon_{si} = E_{ox}\varepsilon_{ox} - Q_F$$

Therefore

$$Q_B = E_s \varepsilon_{si} - Q_{i1} - Q_{i2} = (E_{ox}\varepsilon_{ox} - Q_F) - Q_{i1} - Q_{i2} = V_{GS}C_{ox} - Q_F - Q_{i1} - Q_{i2}$$

and that makes the effective fields :

$$E_{eff1} = \frac{V_{GS}C_{ox} - \frac{2}{3}Q_{i1}}{\varepsilon_{si}} - \frac{Q_F}{\varepsilon_{si}}$$

$$E_{eff2} = \frac{V_{GS}C_{ox} - Q_{i1} - \frac{2}{3}Q_{i2}}{\varepsilon_{sige}} - \frac{Q_F}{\varepsilon_{sige}}$$

The term $\frac{Q_F}{\varepsilon_{layer}}$ *must be subtracted to obtain the correct effective fields.*

3.9 CURRENT THEORY IN HETEROSTRUCTURES

The total drift current density when two layers of inversion charge are present is:

$$J = q(\mu_1 p_1 + \mu_2 p_2)E(y) = (\mu_1 Q_{i1}(y) + \mu_2 Q_{i2}(y))\frac{dV(y)}{dy}$$

Here $Q_1 = qp_1$ and $Q_2 = qp_2$ are the inversion charges per unit area in each of the two inversion layers.

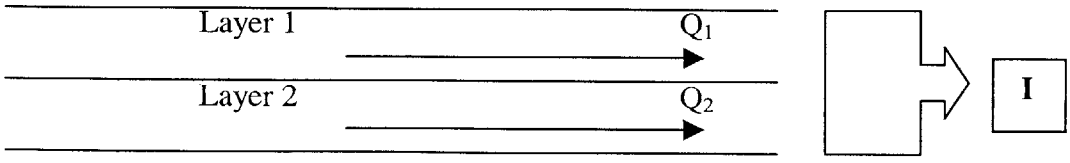

Fig . 3.21. Current generated by two parallel inversion layers.

From the MOSFET theory of inversion we know the inversion charge in an inversion layer has the expression:

$$Q_1(y) = C_{ox}(V_{GS} - V(y) - V_{T1})$$

$$Q_2(y) = C_{ox}(V_{GS}^{'} - V(y) - V_{T2})$$

where V_{T1} and V_{T2} are the threshold voltages for each inversion layer (the layers have different threshold voltages),

V_{GS} is the gate voltage that the first inversion layer feels,

V_{GS}' is the gate voltage that the second inversion layer feels

(V_{GS}' might be different from V_{GS} due to screening effects of one layer by the other layer as an example).

The current becomes

$$I = WC_{ox}(V_{GS} - V(y) - V_{T1})\mu_1 \frac{dV(y)}{dy} + WC_{ox}(V_{GS}' - V(y) - V_{T2})\mu_2 \frac{dV(y)}{dy}$$

Solving the above equation further, we get:

$$I\int_0^L dy = \int_S^D WC_{ox}\mu_1(V_{GS} - V(y) - V_{T1})dV(y) + \int_S^D WC_{ox}\mu_2(V_{GS}' - V(y) - V_{T2})dV(y) =$$

$$= WC_{ox}\mu_1\left[(V_{GS} - V_{T1})V_{DS} - \frac{V_{DS}^2}{2}\right] + WC_{ox}\mu_2\left[(V_{GS}' - V_{T2})V_{DS} - \frac{V_{DS}^2}{2}\right]$$

$$IL = WC_{ox}\mu_1\left[(V_{GS} - V_{T1})V_{DS}\right] + WC_{ox}\mu_2\left[(V_{GS}' - V_{T2})V_{DS}\right]$$

This gives the value of I to be

$$I = \frac{W}{L}C_{ox}\mu(V_{GS} - V_{T1})V_{DS} + \frac{W}{L}C_{ox}\mu_2(V_{GS}' - V_{T2})V_{DS}$$

If we replace the total inversion charges and the geometry factor in the above equation with:

$$Q_{i1} = C_{ox}(V_{GS} - V_{T1})$$

$$Q_{i2} = C_{ox}(V_{GS}' - V_{T2})$$

$$\frac{W}{L} = \frac{1}{G}$$

We get

$$I = \frac{1}{G}(\mu_1 Q_{i1} + \mu_2 Q_{i2})V_{DS}$$

Hence,

$$\mu_1 Q_{i1} + \mu_2 Q_{i2} = \frac{GI}{V_{DS}}$$

3.10 SIMULATIONS AND EXTRACTION OF INDIVIDUAL LAYER MOBILITY IN Si/SiGe STRAINED-LAYERS

3.10.1 Medici Fitting of C-V Characteristics

The wafers studied in this part of the work are:

Wafer1: PMOS device, 40 $\mathring{A}$ strained Si on relaxed $Si_{0.7}Ge_{0.3}$

Wafer2: PMOS device, 120 $\mathring{A}$ strained Si on relaxed $Si_{0.7}Ge_{0.3}$

Wafer3: PMOS device, 85 $\mathring{A}$ strained Si/ 85 $\mathring{A}$ strained $Si_{0.4}Ge_{0.6}$ / relaxed $Si_{0.7}Ge_{0.3}$.

The full C-V curves of each of the 3 wafers are fit in Medici by simulating the MOS capacitor. The parameters to be fit are substrate doping, density of interface traps Dit, and fixed oxide charge.

The C-V of wafer 1 was fit with the following parameters:

- Dit=9.5e11
- Threshold voltage shift due to fixed oxide charges is 9.6V
- Substrate Doping is 3e14cm^{-3}

The C-V of wafer 2 was fit with the following parameters:

- Dit=9.7e11
- Threshold voltage shift due to fixed oxide charges is 10.3V

- Substrate Doping is 3e14cm^{-3}

The C-V of wafer 3 was fit with the following parameters:

- Dit=8.9e11
- Threshold voltage shift due to fixed oxide charges is 18V
- Substrate Doping is 1e15cm^{-3}

The experimental and simulated C-V's for each of these wafers can be found in Appendix B.

3.10.2 Medici Extraction of Inversion Charges

Fitting the C-V allows the extraction in Medici of inversion charges for each of the layers in the wafers.

Fig.3.22 shows the inversion charges in wafers 1 and 2, in the strained silicon and relaxed $Si_{0.7}Ge_{0.3}$ layers. The inversion charge in the surface channel screens the inversion charge in the relaxed channel at higher gate voltages.

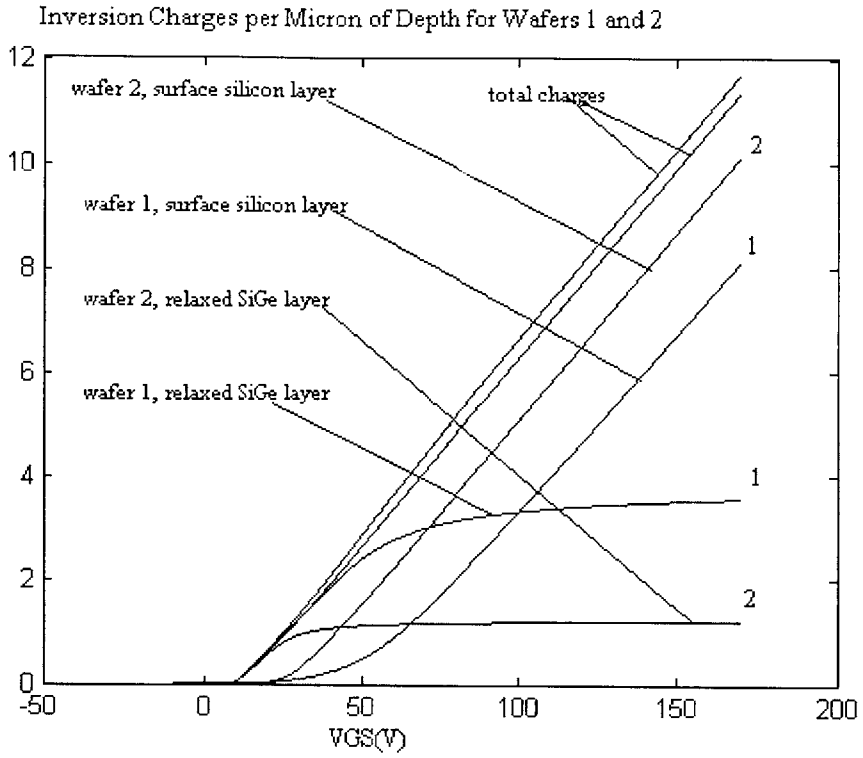

Fig.3.22. Inversion charges in wafers 1 and 2 strained silicon and relaxed $Si_{0.7}Ge_{0.3}$ layers.

Fig.3.23 shows the inversion charges in wafer 3, in the strained silicon, strained $Si_{0.4}Ge_{0.6}$ and relaxed $Si_{0.7}Ge_{0.3}$ layers. The inversion charge in the surface channel screens the inversion charge in the buried (strained $Si_{0.4}Ge_{0.6}$) and the relaxed channel at higher gate voltages.

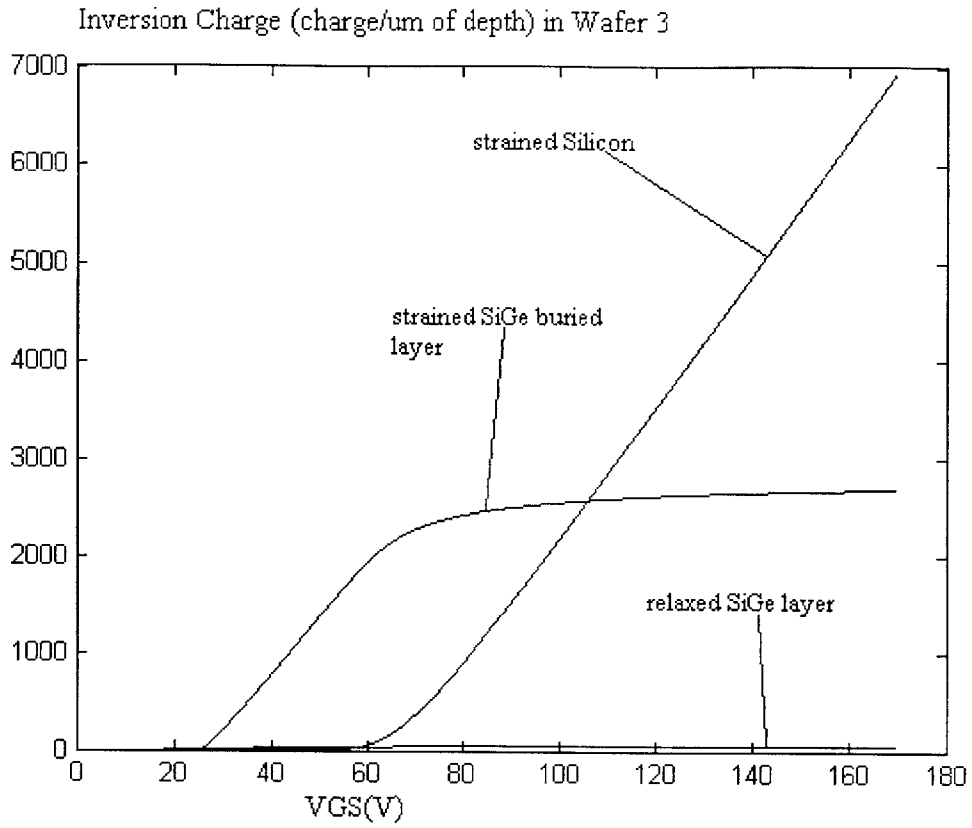

Fig.3.23. Inversion charges in wafer 3 strained silicon , strained $Si_{0.4}Ge_{0.6}$ and relaxed $Si_{0.7}Ge_{0.3}$ layers.

3.10.3 Effective Fields Calculation

Having the inversion charges allows the calculation of the effective fields to which each of the inversion layers is subjected, using the formulas derived in section 3. The effective fields of the buried layer and of the relaxed layer attain a constant value very soon due to the screening of these layers by the strained silicon inversion charge.

The figures below show the effective fields for the inversion layers in each of the wafers.

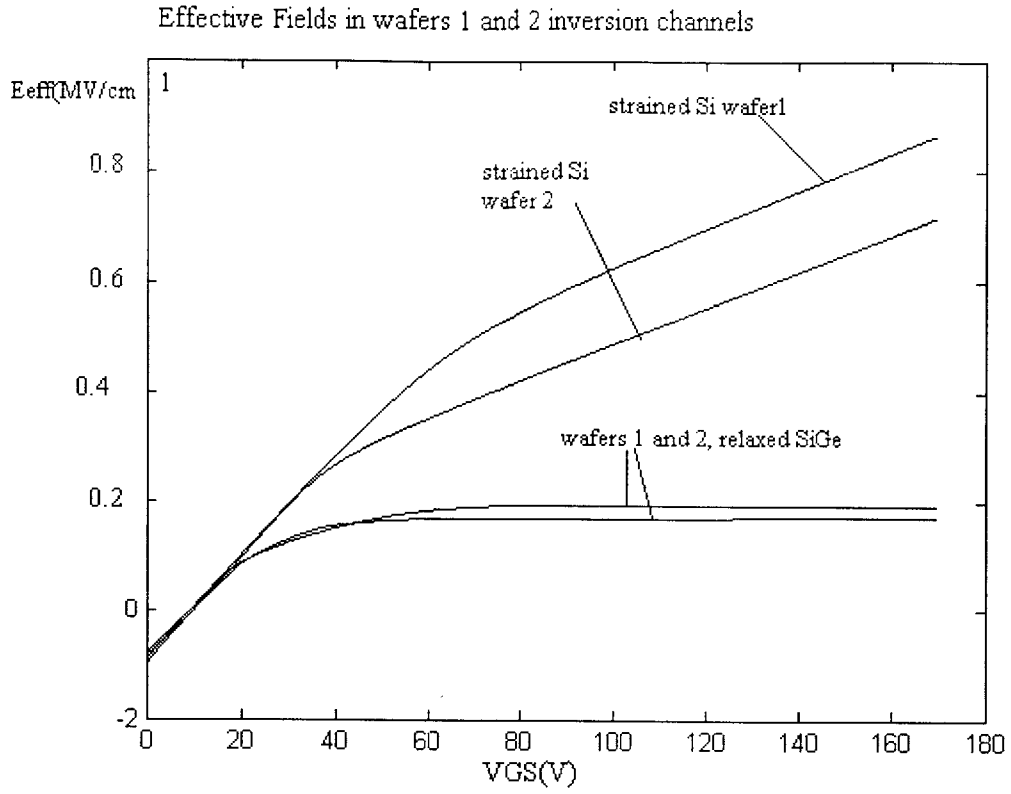

(a)

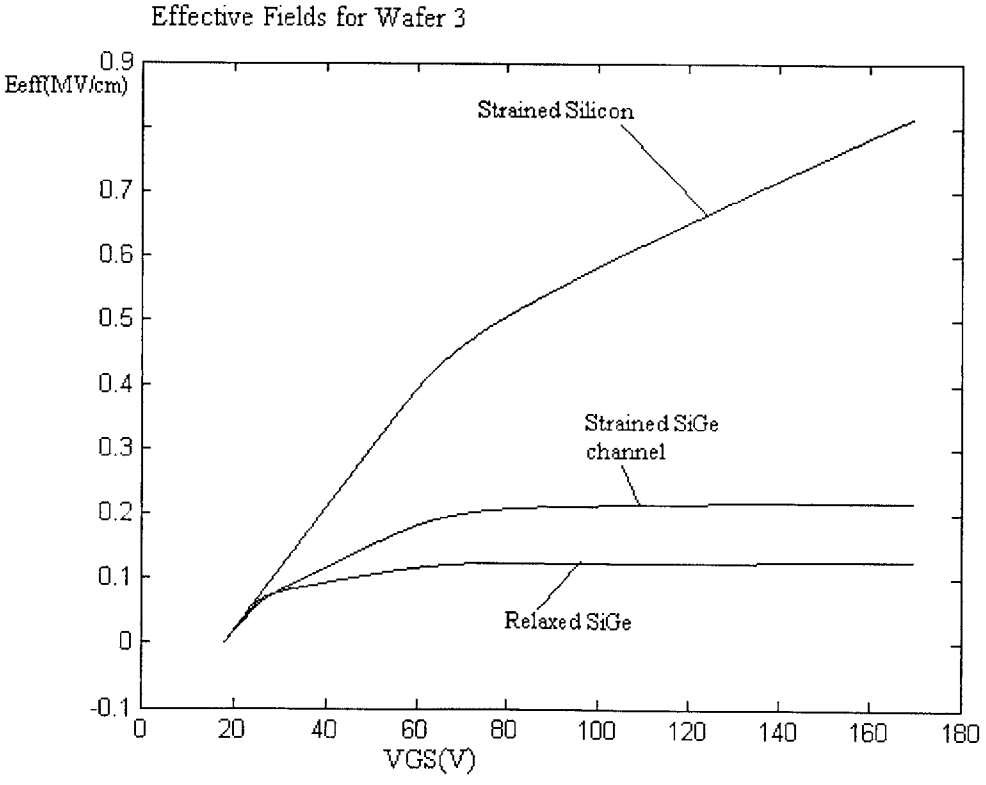

(b)

Fig.3.24. (a) Effective fields in wafers 1 and 2. (b) Effective fields in wafer 3.

3.10.4 Mathematical Method for Mobility Extraction and Results

In this part it will be shown how, with the simulated and experimental information available at this point, the effective mobility of holes in each of the layers can be extracted.

Considering first wafers 1 and 2 with strained silicon on relaxed SiGe, suppose a table of data like the one below is obtained. The effective fields and inversion charges are the ones obtained from Medici, while the I-V information comes from experimental I-V measurement.

In the table below, the subscript "*a*" refers to wafer 1 and "*b*" to wafer 2, while "*1*" refers to strained silicon layer and "*2*" to the relaxed $Si_{0.7}Ge_{0.3}$ layer. Thus, for example, E_{effa1} and E_{effa2} are the effective fields felt by the strained silicon inversion charge and relaxed $Si_{0.7}Ge_{0.3}$ inversion charge respectively, in wafer1. $Q_{i1,a}$ and $Q_{i2,a}$ are the inversion charges in the strained silicon layer and relaxed $Si_{0.7}Ge_{0.3}$ layer respectively.

Table 3.3.

V_{GS} (V)	E_{effa1} si	E_{effa2} sige	$Q_{i1,a}$ si	$Q_{i2,a}$ sige	GI_a/V_{DS}	E_{effb1} si	E_{effb2} sige	$Q_{i1,b}$ si	$Q_{i2,b}$ sige	GI_b/V_{DS}
30	0.31	0.20	9e2	1e3	2e-5	0.45	0.22	5e2	6e2	1e-4
40	0.36	0.21	9.3e2	1.2e3	4e-5	0.50	0.23	7e2	8e2	3e-4
50	0.42	0.22	9.5e2	1.3e3	5e-5	0.53	0.23	9e2	1e3	4e-4
60	0.48	0.22	1e3	1.4e3	8e-5	0.58	0.25	1e3	1.1e3	5.5e-4
70	0.50	0.23	1.4e3	1.5e3	1e-4	0.65	0.26	3e3	2e3	6e-4

80	**0.56**	**0.23**	**3e3**	**1.6e3**	**2e-4**	**0.70**	**0.27**	**5e3**	**2.5e3**	**7e-4**
90	**0.61**	**0.24**	**5e3**	**1.8e3**	**5e-4**	**0.75**	**0.27**	**6e3**	**3e3**	**7.4e-4**

It is possible to find in the table of data 2 pairs (E_{effa1} , E_{effa2}) and (E_{effb1} , E_{effb2}) such that

$$E_{effa1} \approx E_{effb1}$$

$$E_{effa2} \approx E_{effb2}$$

For the effective fields above then, we have one pair of mobilities (μ_1, μ_2), where μ_1 is the mobility of strained silicon inversion holes and μ_2 is the mobility of the relaxed $Si_{0.7}Ge_{0.3}$ inversion layer that correspond to the effective fields E_{effa1} (which is about equal to E_{effb1}), and E_{effa2} (which is about equal to E_{effb2}). These two mobilities will satisfy the following equations (which were derived in Section 3.9):

$$Q_{i1,a}\mu_1 + Q_{i2,a}\mu_2 = \frac{GI_a}{V_{DS}}$$

$$Q_{i1,b}\mu_1 + Q_{i2,b}\mu_2 = \frac{GI_b}{V_{DS}}$$

from which μ_1 and μ_2 can be found. Once they are found, the method is applied iteratively through the whole table, thus finding the mobilities μ_1 and μ_2 for all the effective fields in the table. The iteration method takes advantage of the fact that, for example, the effective field E_{effa2} or a value very close to it will be present in a number of other places in the table, and then once the mobility of the relaxed layer is known , the corresponding mobility of the strained layer can be found.

By this analysis, the mobility of relaxed $Si_{0.7}Ge_{0.3}$ holes was found to be about 124cm2/Vs, in the whole region where the effective field associated with the relaxed inversion layer is constant. The strained silicon hole mobility is then extracted. The results are shown below.

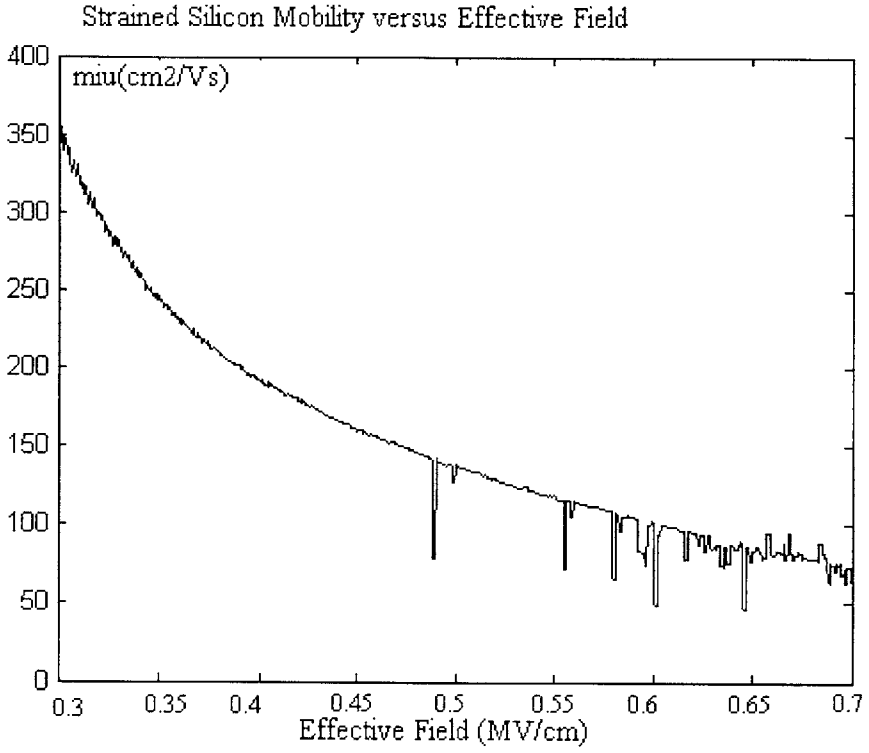

Fig.3.25. Strained Silicon Inversion Hole Mobility versus Effective Field.

Once the mobility dependence on effective field has been found for strained silicon and relaxed $Si_{0.7}Ge_{0.3}$, the results can be used for wafer 3 where the equation $Q_{i1}\mu_1 + Q_{i2}\mu_2 + Q_{i3}\mu_3 = \frac{GI}{V_{DS}}$ applies. Here, Q_{i1} and μ_1 refer to the strained silicon layer, Q_{i2} and μ_2 to the relaxed $Si_{0.7}Ge_{0.3}$, and Q_{i3} and μ_3 to the strained $Si_{0.4}Ge_{0.6}$ layer. With μ_1 and μ_2 determined from the study done on wafers 1 and 2, μ_3 can be determined. Below is the graph obtained.

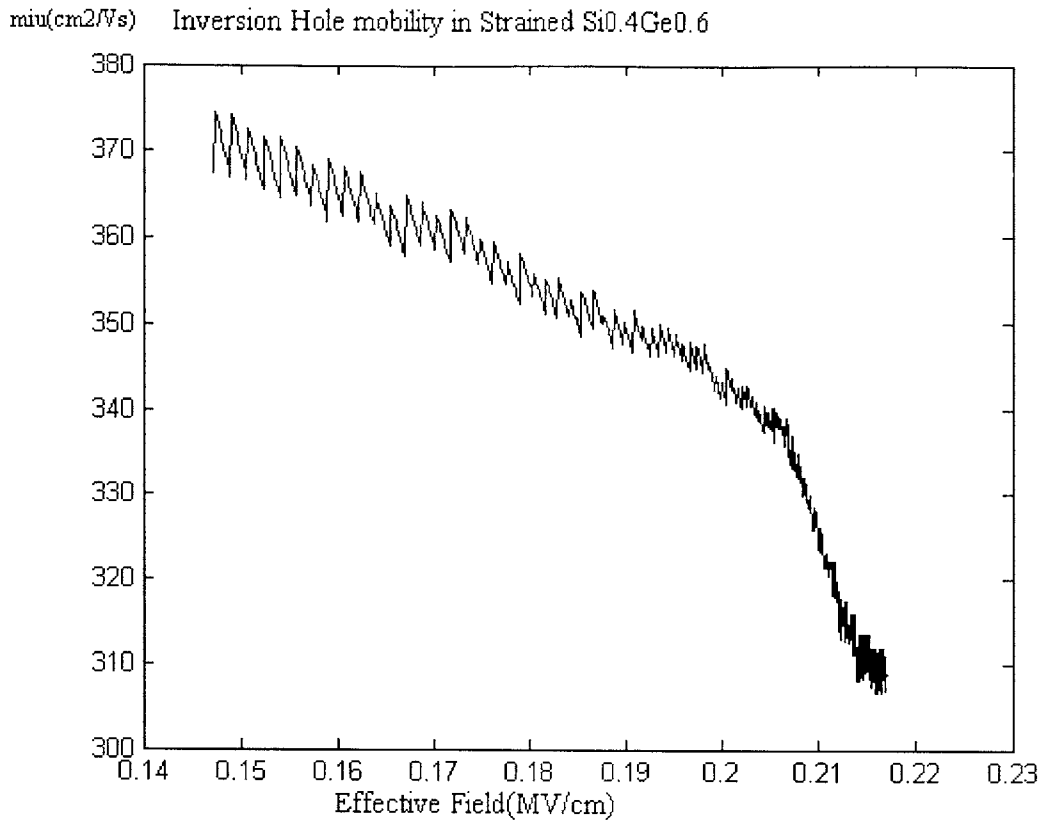

Fig.3.26. Strained $Si_{0.4}Ge_{0.6}$ Inversion Hole Mobility versus Effective Field. The jitters in the graph are due to Matlab meshing and limits in the mathematical processing.

One more observation is interesting to make here. Below is the graph of the hole mobilities of wafers 329 and 342 as extracted by Leitz[40] (by the Armstrong method). The mobility for each wafer is a mix of strained silicon and relaxed $Si_{0.7}Ge_{0.3}$ mobility.

Wafer# 329 40 $\mathring{A}$ strained Si on relaxed $Si_{0.7}Ge_{0.3}$

Wafer# 342 85 $\mathring{A}$ strained Si on relaxed $Si_{0.7}Ge_{0.3}$

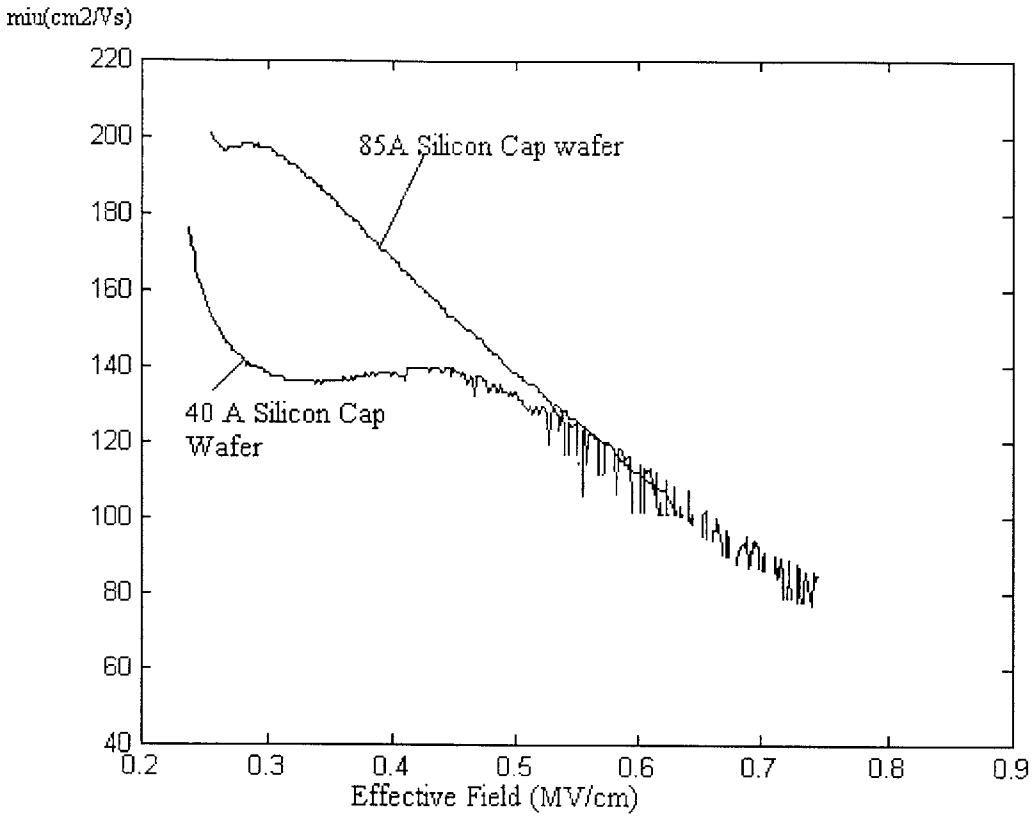

Fig.3.27 Composite Mobility of wafers 329 and 342.

It is clear that the thicker the strained silicon cap, the higher the mobility at low effective fields. In view of the study done on individual mobilities and effective fields in this chapter, the phenomenon can be explained in the following way. The percentage of inversion hole carriers in the silicon cap is larger for wafer 342 than for wafer 329. That is because the thicker the cap, the more inversion carriers there are in the cap. The more carriers there are in the cap, the fewer carriers there are in the relaxed layer because the cap screens the relaxed layer to some extent even at low effective fields. The fewer carriers there are in the relaxed layer, the smaller the effective field the cap carriers feel (because the inversion charges in the relaxed layer contribute to the effective field felt by the cap carriers, as shown in Section 8). Therefore, the mobility of holes in the cap will be higher in the wafer with a thicker cap (lower effective field). Also, the mobility of the

relaxed hole carriers is much smaller than that of strained hole carriers. Thus, with higher mobility of cap carriers and more percentage of cap carriers, the wafer with thicker cap will have higher composite mobility.

Chapter 4

Conclusion

4.1 SUMMARY

This thesis has examined several properties of SiGe alloys and SiGe PMOS. The contributions are summarized below.

- **Valence Band Structure and Effective Mass of Holes in SiGe Alloys**

The theoretical formalism for the calculation of effective mass of holes for any relaxed SiGe alloy, or strained SiGe alloy subjected to any vertical strain, has been described. Values for density of states and carrier concentration effective mass of holes in these alloys have been calculated for room temperature and low-temperature. Also, the energy spectra of the strained and relaxed SiGe alloys have been obtained, as well as the constant energy surfaces.

The values for effective masses of holes in SiGe alloys can now be used in simulations of SiGe MOSFETS at room and low temperature. The low-temperature values especially, have never been calculated before.

The influence of stress on the effective mass spectrum has been thoroughly investigated. Since effective mass and energy spectrum give drift mobility, this study can

shed new light on the mobility of holes in SiGe alloys and on the optimum composition of SiGe alloys that would give highest hole mobility.

- **Experimental Determination of Hole Mobility of Strained SiGe Buried-Channel PMOS at Low Temperatures**

The inversion mobility of holes in strained SiGe buried-channel PMOS at low temperatures has never been measured before. In this thesis this mobility has been measured for temperatures down to 100K, for a number of SiGe channels.

- **Inversion Hole Mobility Mechanisms in Strained Si and Strained SiGe**

Using the experimental data for hole mobility at room and low temperatures for buried-channel SiGe PMOS, mechanisms for mobility degradation have been discussed Theoretical effective field dependencies of mobility have been proposed as drawn from the experimental results.

- **Determination of Individual Strained Si , Strained SiGe and Relaxed SiGe Hole Inversion Mobilities**

Using the experimental data available for room-temperatures, as well as MEDICI simulations, the mobilities for inversion holes in each of the channels of the PMOS studied - the strained Si channel, the strained SiGe channel, and the relaxed SiGe channel- have been determined. Also, the number of the carriers in the three channels has been investigated and it was determined how these populations of carriers give rise to the earlier observed experimental composite mobility of buried-channel SiGe PMOS.

Bibliography

[1]F. Bassani, D. Brust, "Effect of alloying and pressure on the band structure of Germanium and Silicon", Phys. Rev. **131**, 1524 (1963)

[2]M. Cardona, F. Pollak, "Energy-band structure of Germanium and Silicon: the **kp** method", Phys. Rev. **142**, 530 (1965)

[3]G. Dresselhaus, A. F. Kip, C. Kittel, "Cyclotron resonance of electrons and holes in Silicon and Germanium Crystals", Phys. Rev. **98**, 368 (1954)

[4]M. V. Fischetti, S. E. Laux, "Band structure deformation potentials, and carrier mobility in strained Si, Ge and SiGe alloys", J. Appl. Phys. **80** (4), 2234 (1996)

[5]M. Gell, "Effective masses and sum rules in strained Si/Ge structures", Phys. Rev. B **41**, 7611 (1989)

[6]H. Hasegawa, "Theory of cyclotron resonance in strained Silicon crystals", Phys. Rev. **129**, 1029 (1962)

[7]J. C. Hensel, K. Suzuki, "Quantum resonances in the valence bands of germanium II. Cyclotron resonances in uniaxially stressed crystals", Phys. Rev. B **9**, 4219 (1974)

[8]J. C. Hensel, K. Suzuki, "Quantum resonances in the valence bands of germanium I. Theoretical considerations", Phys. Rev. B **9**, 4184 (1974)

[9]J. C. Hensel, G. Feher, "Cyclotron resonance experiments in uniaxially stressed Silicon: valence band inverse mass parameters and deformation potentials", Phys. Rev. **129**, 1041 (1963)

[10]E. O. Kane, "Energy band structure in p-type germanium and silicon", J. Phys. Chem. Solids **1**, 82 (1956)

[11]W. H. Kleiner, L. M. Roth, "Deformation potential in Germanium from optical absorption lines for exciton formation", Phys. Rev. Lett. **2**, 334 (1959)

[12]P. Lawaetz, "Valence-band parameters in cubic semiconductors", Phys. Rev. B **4**, 3460 (1971)

[13]F. L. Madarasz, J. E. Lang, P. M. Hemeger, "Effective masses for nonparabolic bands in p-type Silicon", J. Appl. Phys **52** (7), 4646 (1981)

[14]T. Manku, S. C. Jain, A. Nathan, "On the reduction of hole mobility in strained p-SiGe layers", J. Appl. Phys **71** (9), 4618 (1992)

[15]T. Manku, A. Nathan, "Energy-band structure for strained p-type SiGe", Phys. Rev. B **43**, 12634 (1990)

[16]A. Nathan, T. Manku, "Modeling of piezo-Hall effects in n-doped Silicon devices", Appl. Phys. Lett. **62** (23), 2947 (1993)

[17]T. Manku, A. Nathan, "Electrical properties of Silicon under nonuniform stress", J. Appl. Phys. **74** (3), 1832 (1993)

[18]T. Manku, A. Nathan, "Lattice mobility of holes in strained and unstrained SiGe alloys", IEEE Elec. Dev. Lett. **12** (12), 704 (1991)

[19]T. Manku, A. Nathan, "Valence energy-band structure for strained group-IV semiconductors", J. Appl. Phys. **73** (3), 1205 (1992)

[20]T. Manku, A. Nathan, "Effective mass for strained p-type SiGe", J. Appl. Phys. **69** (12), 8414 (1991)

[21]R. People, "Physics and applications of GeSi/Si strained layer heterostructures", IEEE J. Quantum Electronics **QE-22** (9), 1696 (1986)

[22]R. People, "Indirect band gap of coherently strained GeSi bulk alloys on <001> Silicon substrates", Phys. Rev. B **32** (2), 1405 (1985)

[23]G. E. Pikus, "On relationships among the various theories of scattering of carrier currents in semiconductors", Sov. Phys. Solid. State **2**, 3012 (1961)

[24]G. L. Bir, G. E. Pikus, "Theory of the deformation potential for semiconductors with a complex band structure", Sov. Phys. Solid State **2**, 2039 (1961)

[25]M. Rieger, P. Vogl, "Electronic-band parameters in strained SiGe alloys on SiGe substrates", Phys. Rev. B **48**, 14276 (1993)

[26]W. Shockley, "Energy band structures in semiconductors", Phys. Rev. **77**, 407 (1950)

[27]C. Smith, "Piezoresistance effect in Germanium and Silicon", Phys. Rev. **94**, 42 (1953)

[28]H. Zukotynski, H. Nakagawa, "The valence band structure and the hole mobility in Silicon", Can. J. Phys. **55**, 1485 (1977)

[29]E. Kasper, *Properties of Strained and Relaxed Silicon Germanium*, EMIS Datareviews Series No. 12, INSPEC, 1995

[30]T.Manku, J. McGregor, A.Nathan, D.Roulston, J.Noel, D.C Houghton, "Drift hole mobility in strained and unstrained doped SiGe alloys", IEEE Transactions on Electron Devices **40**, No. 11, 1990 (1993)

[31]C. R. Visvanathan, "Low-temperature CV dispersion in MOS devices", IEEE Transactions on Electron Devices, Vol. **12**, No. 9, 503 (1991)

[32]R. Divakaruni, V. Prabhakar, C. R. Visvanathan, "Activation energy determination from low-temperature CV dispersion", IEEE Transactions on Electron Devices, Vol. **41**, No. 8, 1405 (1994)

[33]C. R.Viswanathan, R. Divakaruni, V. Prabhakar, "Depletion region formation at low temperatures", VLSITSA, 1991

[34]R. Divakaruni, C. R. Visvanathan, "Quasi-static behavior of MOS devices in the freeze-out regime", IEEE Transactions on Electron Devices, Vol. **42**, No. 1, 87 (1995)

[35]A. Hairapetian, D, Gitlin, C. R. Visvanathan, "Low-temperature mobility measurements on CMOS devices", IEEE Transactions on Electron Devices, Vol. **36**, No. 8, 1448 (1989)

[36]C. R. Visvanathan, "Low temperature characterization of CMOS devices", Invited Talk, UCLA (1995)

[37]S. C. Jain, *Germanium-Silicon Strained Layers and Heterostructures*, Academic Press, 1994

[38]J. Singh, *Physics of Semiconductors and Their Heterostructures*, McGraw-Hill, Inc., 1993

[39]M. A.Armstrong, *Technology for SiGe Heterostructure-Based CMOS Devices*, Ph.D. thesis , Massachusetts Institute of Technology (1999)

[40]C.Leitz, Ph.D.thesis, Massachusetts Institute of Technology (2002)

[41]M.T.Currie, *SiGe Virtual Substrate Engineering for Integration of III-V Materials, Microelectromechanical Systems, and Strained Silicon MOSFETS with Silicon*, Ph.D. thesis, Massachusetts Institute of Technology (2001)

[42]S. Takagi, A. Toriumi, M. Iwase, "On the Universality of inversion layer mobility in Si MOSFET's: Part I- Effects of substrate impurity concentration", IEEE Transactions on Electron Devices, Vol. **41**, No. 12, 2357 (1994)

[43]S. Takagi, A. Toriumi, M. Iwase, H. Tango "On the Universality of inversion layer mobility in Si MOSFET's: Part II- Effects of surface orientation", IEEE Transactions on Electron Devices, Vol. **41**, No. 12, 2363 (1994)

[44]B. R. Cyca, K. G. Robins, N. G. Tarr, D. X. Xu, J. P. Noel, D. Landheer, M. Simard-Normandin, "Hole confinement and mobility in heterostructure Si/Ge/Si p-channel metal-oxide-semiconductor field effect transistors", J. Appl. Phys., **81**, No. 12, 8079 (1997)

[45]C.W.Leitz, M.T.Currie, M.L.Lee, Z.Y.Cheng, D.A.Antoniadis, E.A.Fitzgerald, "Hole mobility enhancements in strained Si/SiGe p-type MOSFET grown on relaxed SiGe virtual substrates", Appl. Phys. Lett. **79** , 4246 (2001)

[46]M.T.Currie, C.W.Leitz, T.A.Langdo,G.Taraschi, E.A.Fitzgerald and D.A. Antoniadis, "Carrier mobilities and process stability of strained Si n- and p-MOSFETs on SiGe virtual substrates", J.Vac.Sci.Technol.B **19**, 2268 (2001)

[47]Y.Tsividis, *Operation and Modeling of the MOS Transistor*, McGraw-Hill, 1999

Appendix A

A.1 Heavy Holes

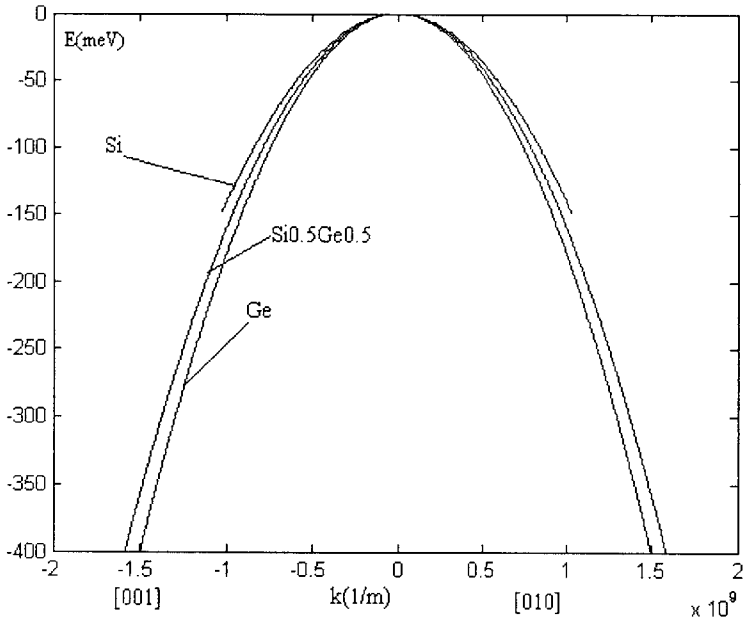

Fig.A.1. Heavy Hole Spectrum of relaxed Si, relaxed Si0.5Ge0.5 and relaxed Ge.

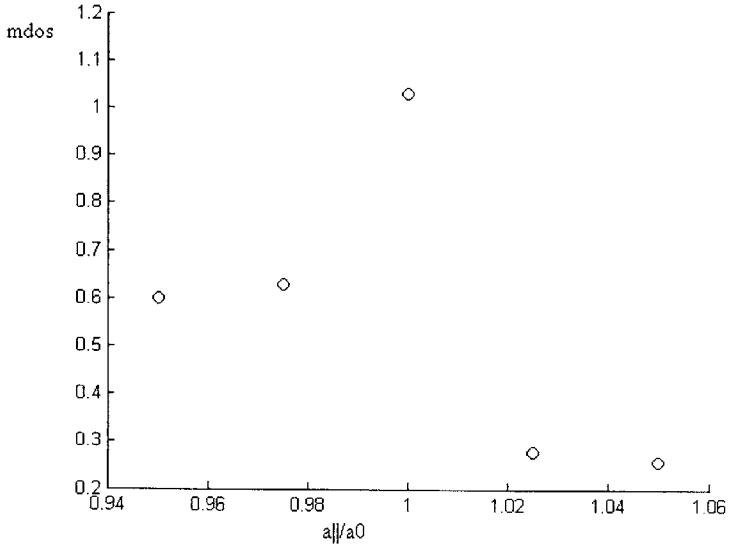

Fig.A.2. Heavy Hole Mass of Strained Si versus lattice strain (at E=-25meV from the top of the corresponding energy band). Here a|| is the strained Si lattice and a0 is the unstrained Si lattice. The 5 points are at a||/a0 of values 1.05, 1.025, 1 (unstrained), 0.975, 0.950. The values agree with the strained Si masses obtained by Fischetti and Laux [4] .

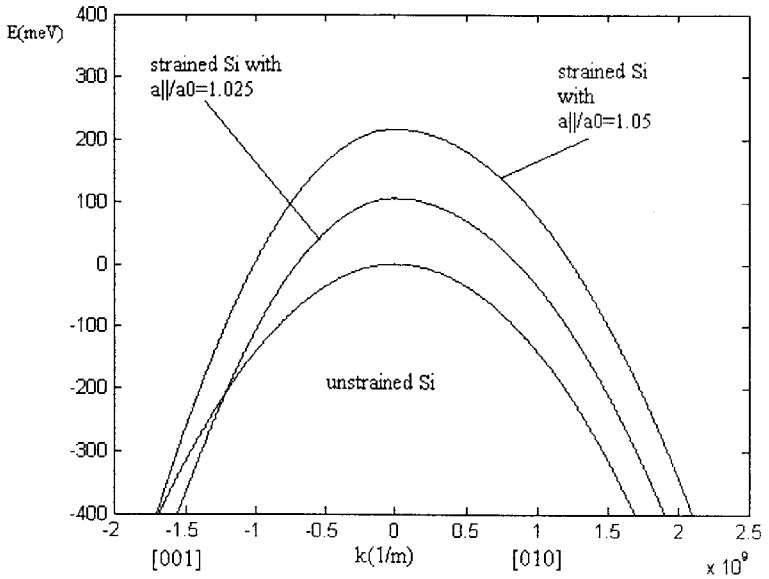

Fig.A.3. E(K) dependence (spectrum) of heavy hole valence band in relaxed Si, and in strained Si for 2 strains. The strained Si lattice is larger than the unstrained lattice. The strain is applied in the [001] direction.

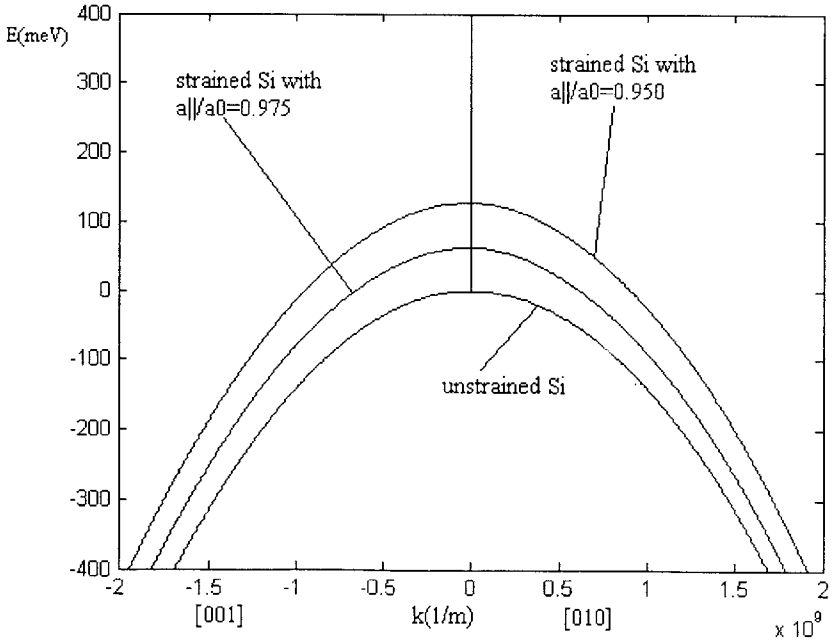

Fig.A.4. E(k) dependence (spectrum) of heavy hole valence band in relaxed Si, and in strained Si for 2 strains. The strained Si lattice is smaller than the unstrained lattice. The strain is applied in the [001] direction.

A.2 Light Holes

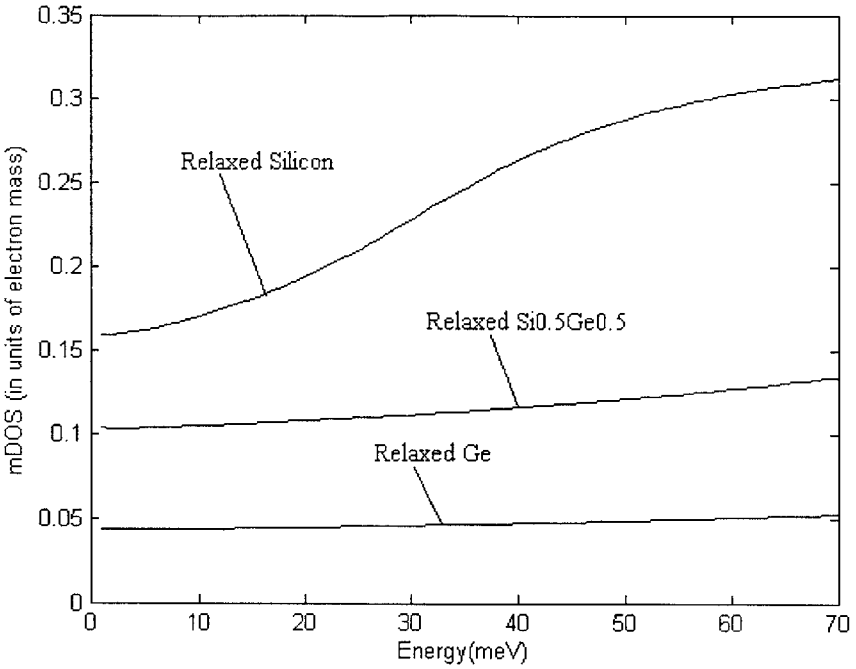

Fig.A.5. Light Hole *mdos*(E) for relaxed Si, relaxed Ge and relaxed Si0.5Ge0.5.

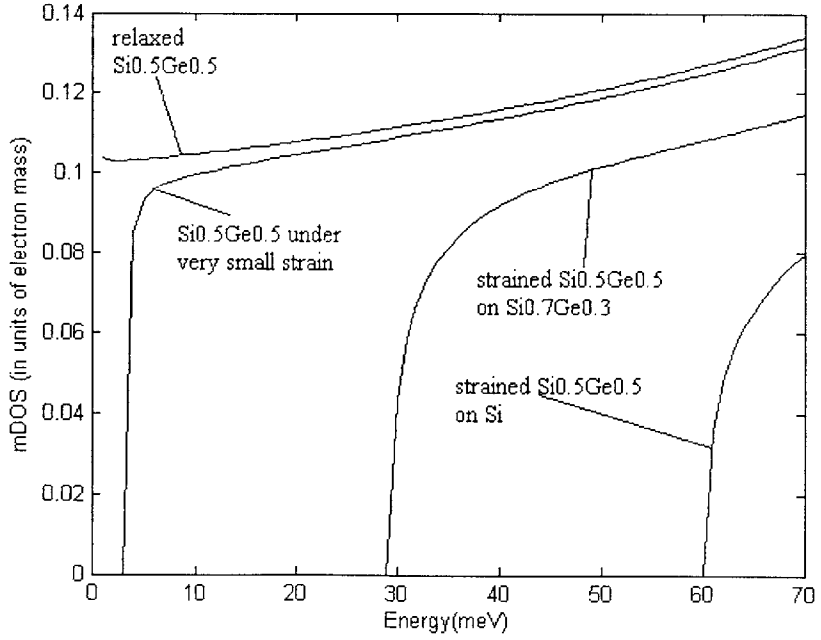

Fig. A.6. Light Hole *mdos*(E) for strained Si0.5Ge0.5 under various stresses. Relaxed Si0.5Ge0.5 light hole mass is also shown for comparison.

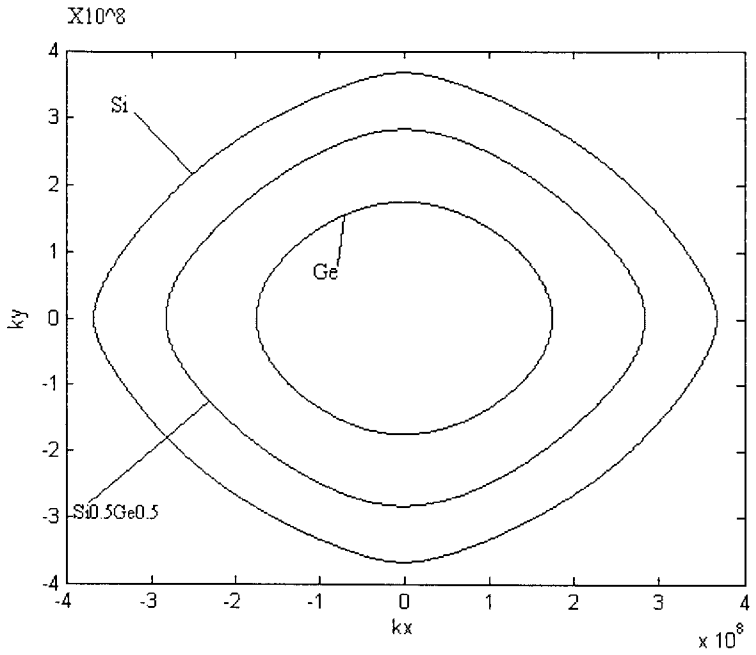

Fig.A.7. Constant Energy Surfaces (E=-25meV) for light hole relaxed Si, relaxed Ge and relaxed Si0.5Ge0.5.

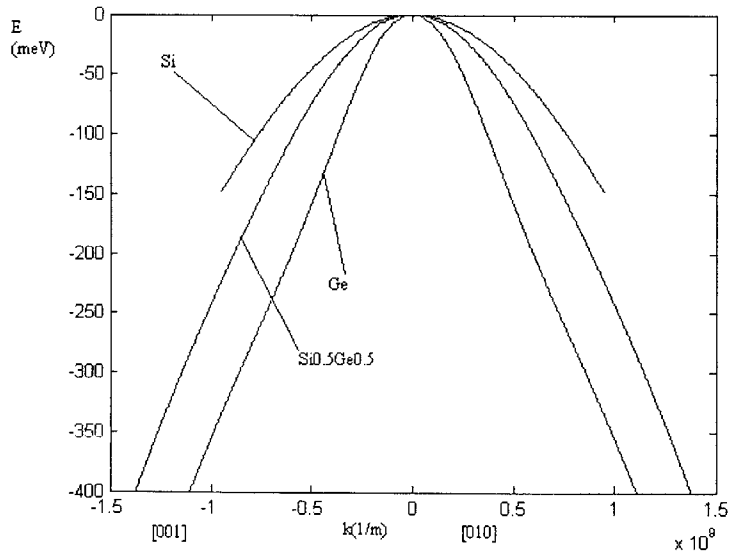

Fig.A.8. Light Hole Spectrum of relaxed Si, relaxed Si0.5Ge0.5 and relaxed Ge.

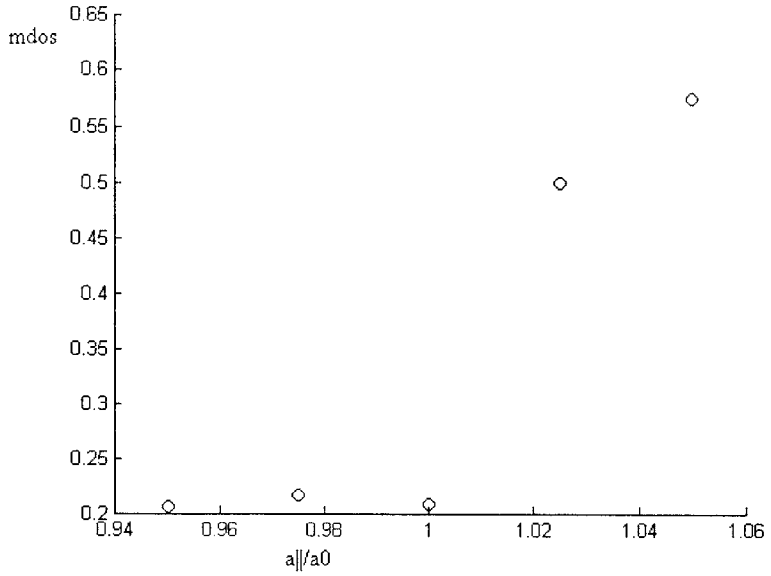

Fig.A.9. Light Hole Mass of Strained Si versus lattice strain (at E=-25meV from the top of the corresponding energy band). Here a|| is the strained Si lattice and a0 is the unstrained Si lattice. The 5 points are at a||/a0 of values 1.05, 1.025, 1 (unstrained), 0.975, 0.950. The values agree with the strained Si masses obtained by Fischetti and Laux [4] .

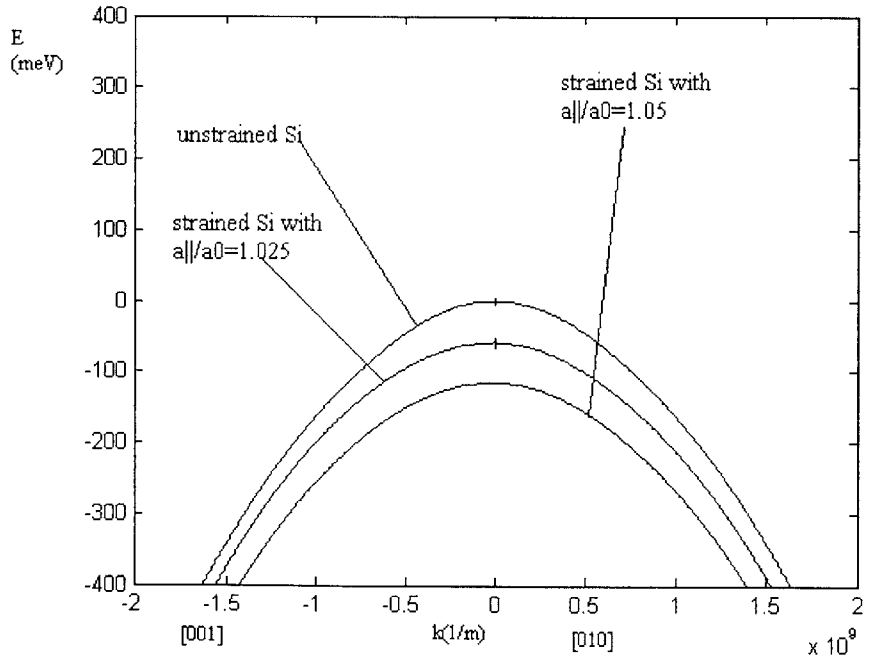

Fig.A.10. E(k) dependence (spectrum) of light hole valence band in relaxed Si, and in strained Si for 2 strains. The strained Si lattice is larger than the unstrained lattice. The strain is applied in the [001] direction.

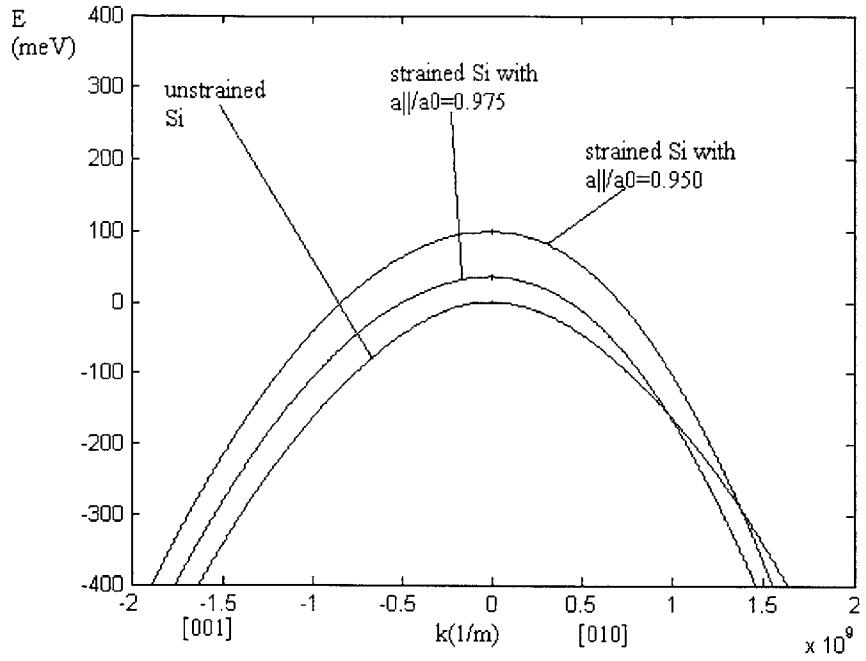

Fig.A.11. E(k) dependence (spectrum) of light hole valence band in relaxed Si, and in strained Si for 2 strains. The strained Si lattice is smaller than the unstrained lattice. The strain is applied in the [001] direction.

A.2 Spin-Off Holes

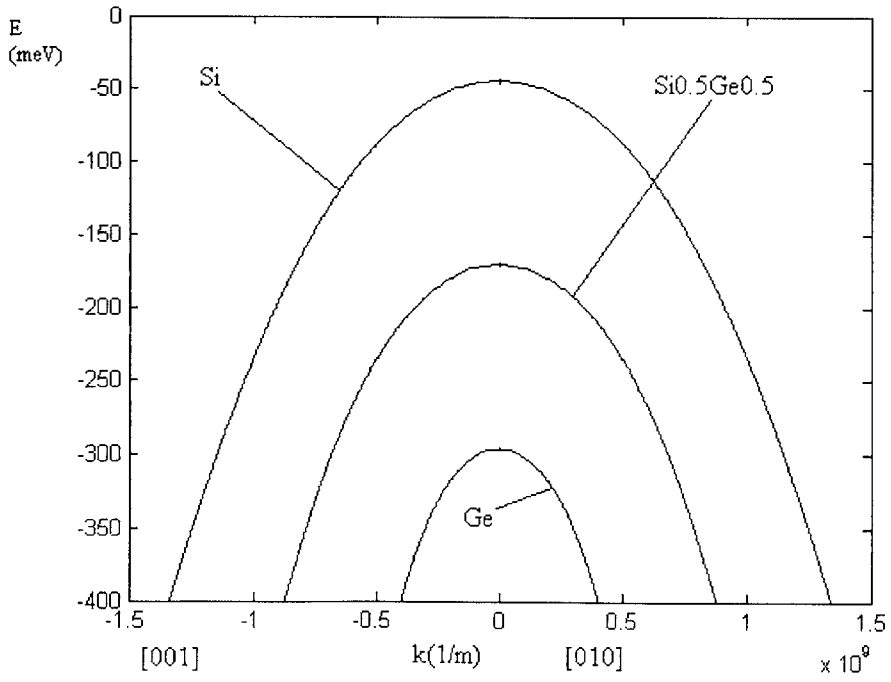

Fig.A.12. Spin-Off Hole Spectrum of relaxed Si, relaxed Si0.5Ge0.5 and relaxed Ge.

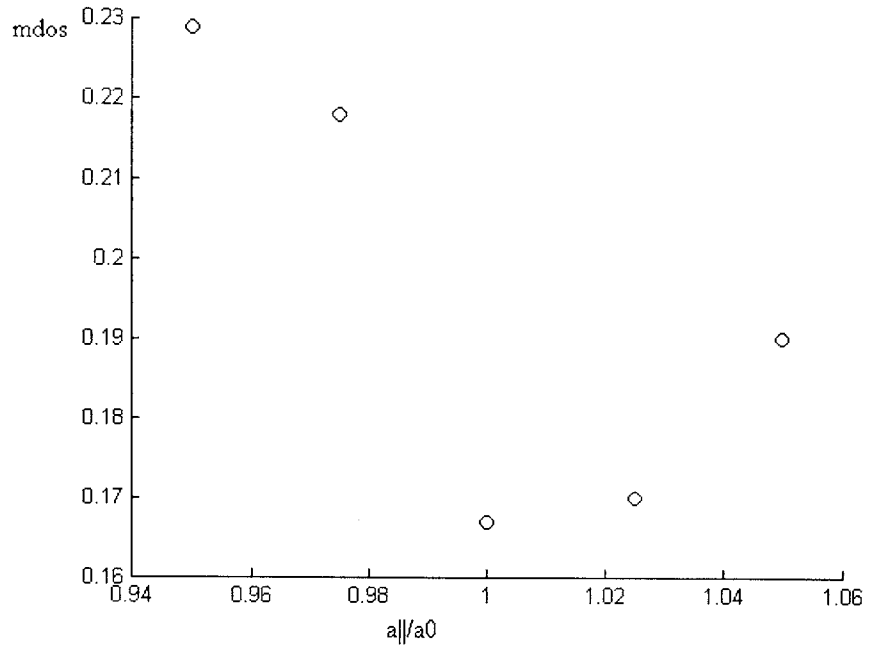

Fig.A.13. Spin-Off Hole Mass of Strained Si versus lattice strain (at E=-25meV from the top of the corresponding energy band). Here a|| is the strained Si lattice and a0 is the unstrained Si lattice. The 5 points are at a||/a0 of values 1.05, 1.025, 1 (unstrained), 0.975, 0.950. The values agree with the strained Si masses obtained by Fischetti and Laux [4] .

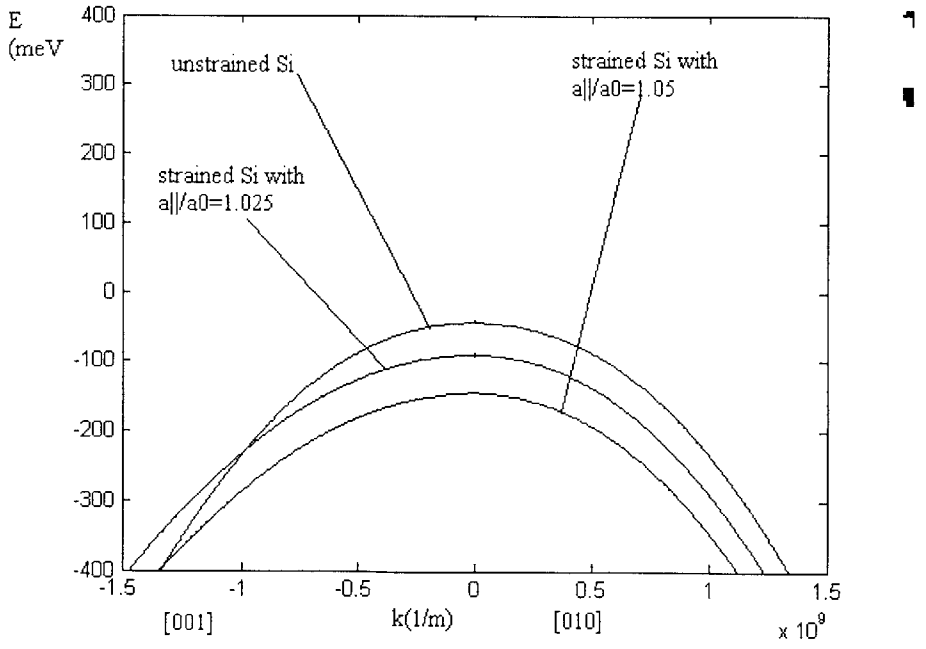

Fig.A.14. E(k) dependence (spectrum) of spin-off hole valence band in relaxed Si, and in strained Si for 2 strains. The strained Si lattice is larger than the unstrained lattice. The strain is applied in the [001] direction.

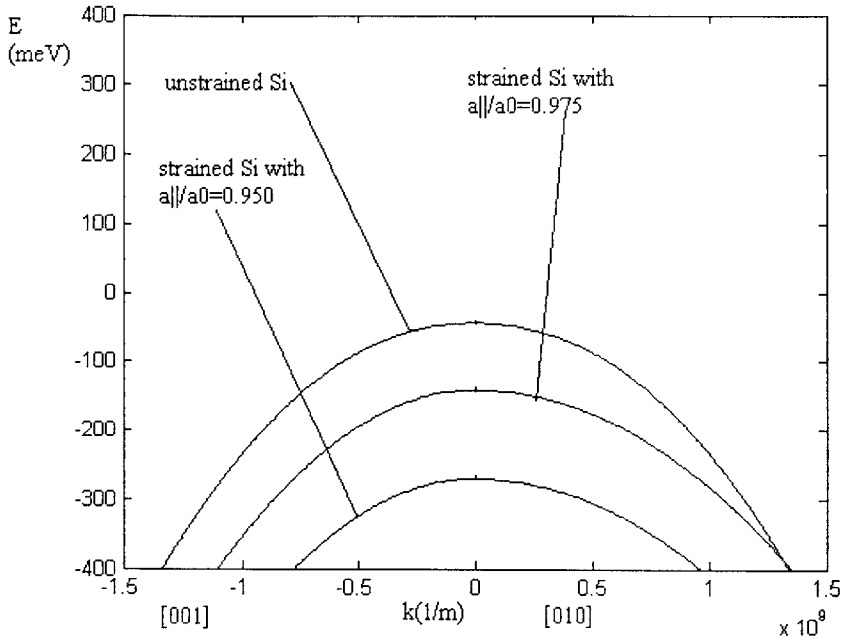

Fig.A.15. E(k) dependence (spectrum) of spin-off hole valence band in relaxed Si, and in strained Si for 2 strains. The strained Si lattice is smaller than the unstrained lattice. The strain is applied in the [001] direction.

Appendix B

Experimental Data: Hole Mobility of SiGe PMOS Devices for Section 3.6.3

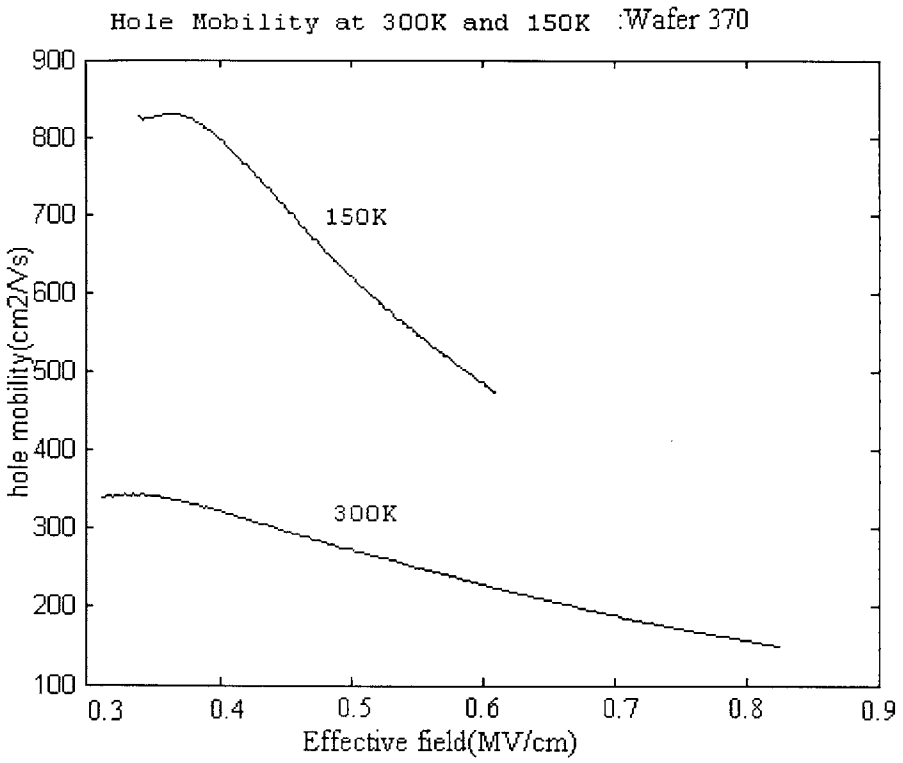

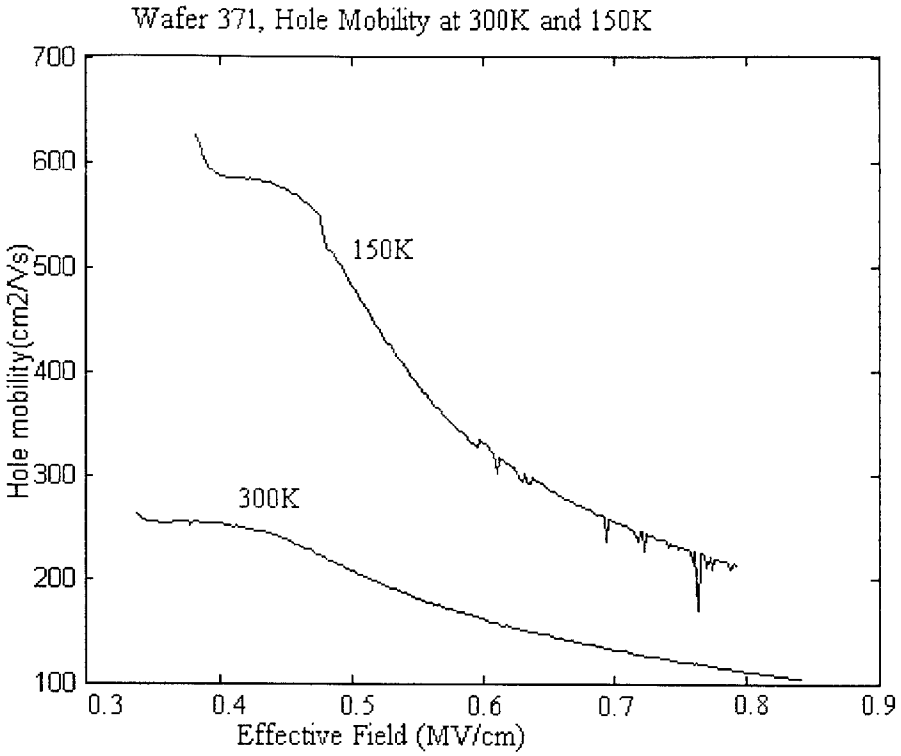
Wafer 371, Hole Mobility at 300K and 150K
Hole mobility(cm2/Vs)
Effective Field (MV/cm)
150K
300K
700
600
500
400
300
200
100
0.3
0.4
0.5
0.6
0.7
0.8
0.9

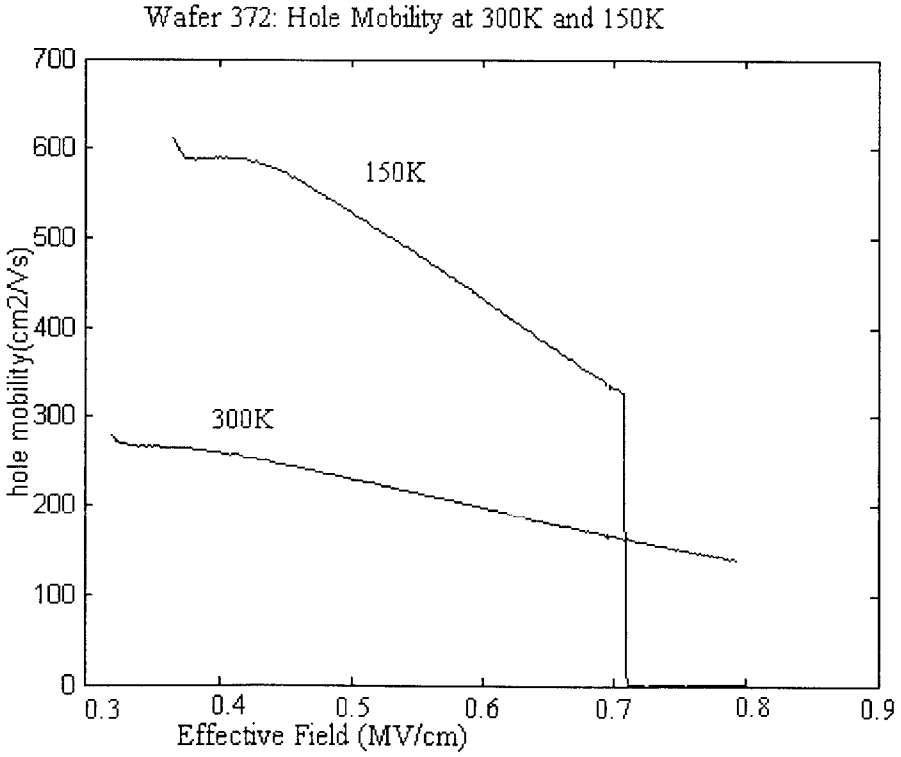
Wafer 372: Hole Mobility at 300K and 150K
hole mobility(cm2/Vs)
Effective Field (MV/cm)
150K
300K
700
600
500
400
300
200
100
0
0.3
0.4
0.5
0.6
0.7
0.8
0.9

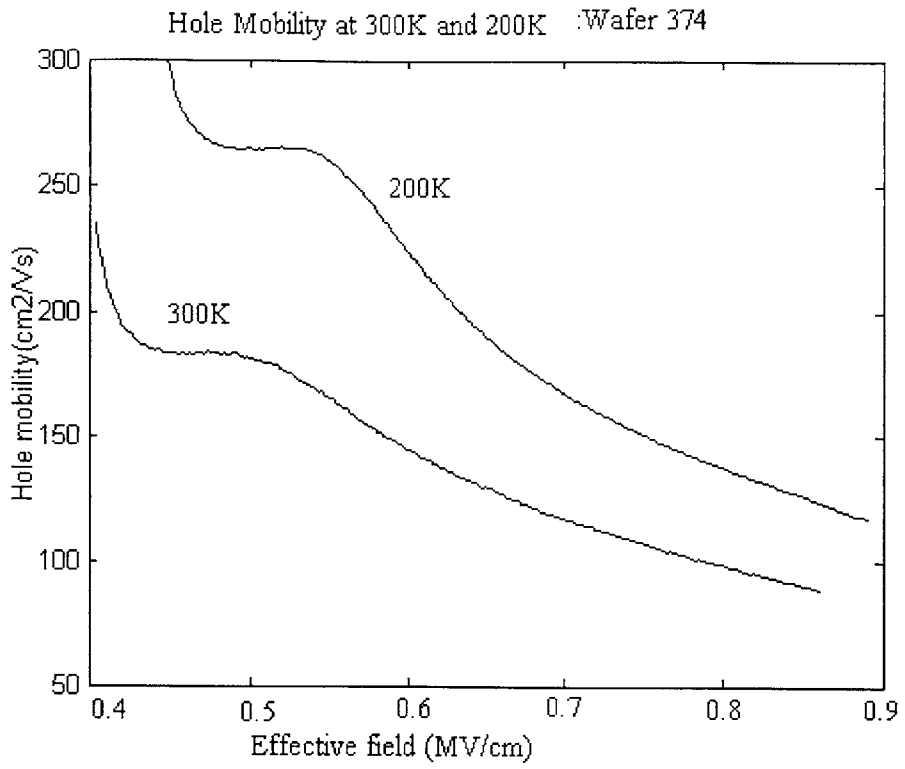
Hole Mobility at 300K and 200K :Wafer 374
300
250
200
150
100
50
Hole mobility(cm2/Vs)
200K
300K
0.4
0.5
0.6
0.7
0.8
0.9
Effective field (MV/cm)

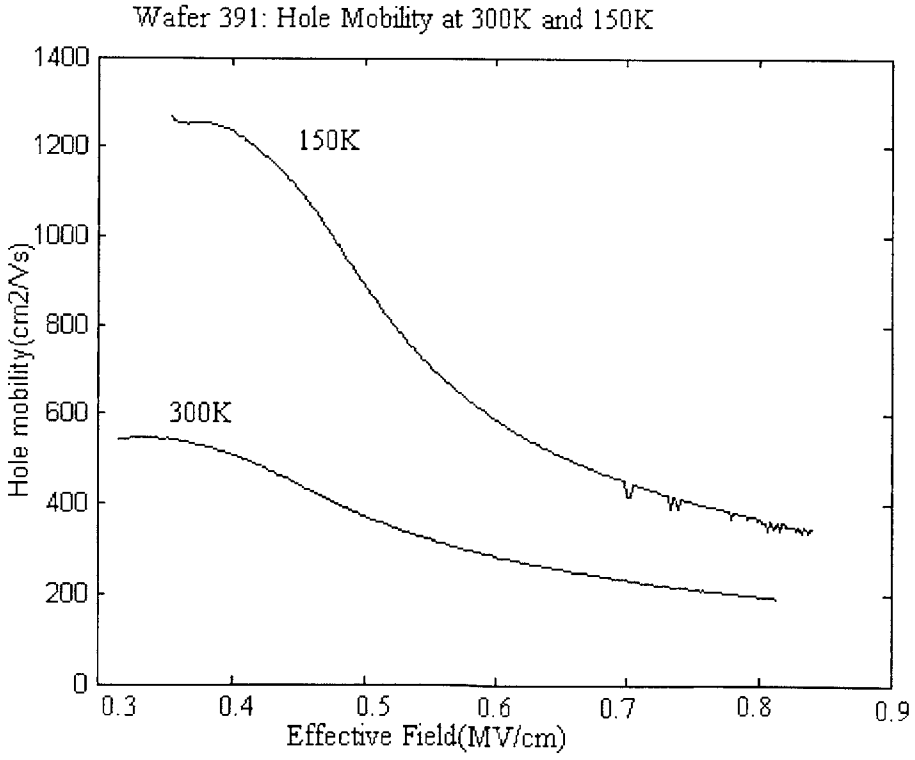
Wafer 391: Hole Mobility at 300K and 150K
1400
1200
1000
800
600
400
200
0
Hole mobility(cm2/Vs)
150K
300K
0.3
0.4
0.5
0.6
0.7
0.8
0.9
Effective Field(MV/cm)

Experimental Data: Slope of Hole Mobility in SiGe PMOS Devices for Section 3.6.5

Some of the graphs are presented below, in order to show the linear regions in the log-log graph of mobility vs. effective field.

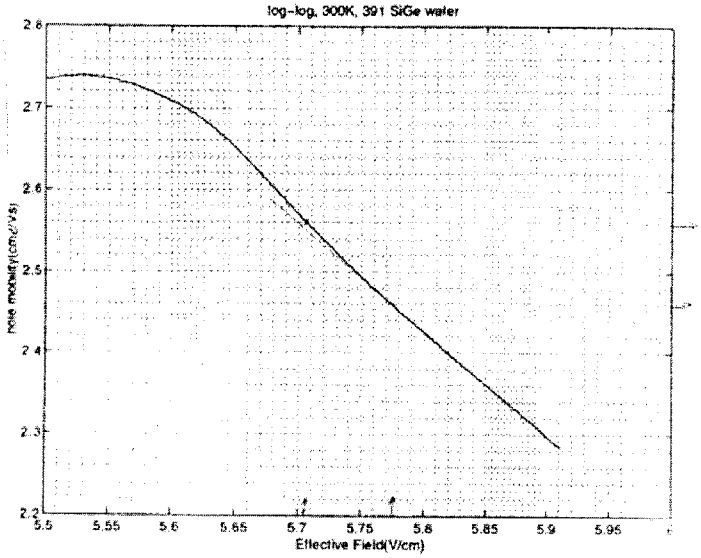

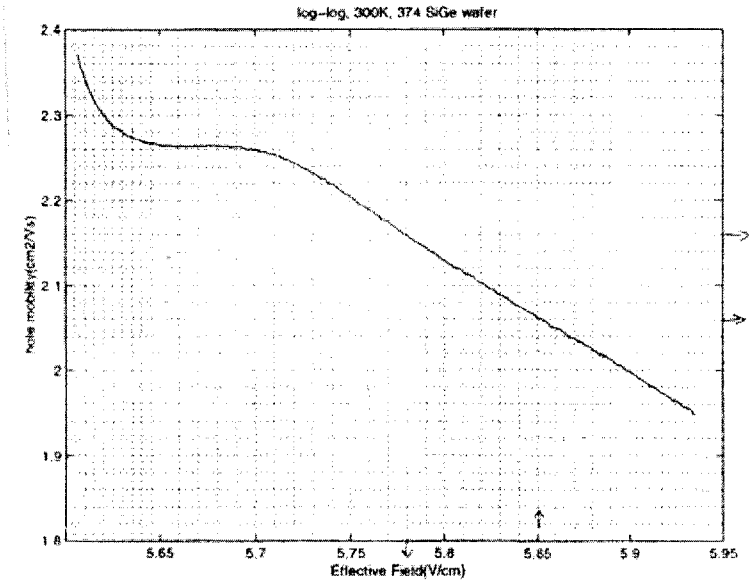

Simulated and Experimental C-V Characteristics of Wafers 1,2, and 3 for Section 3.10.1

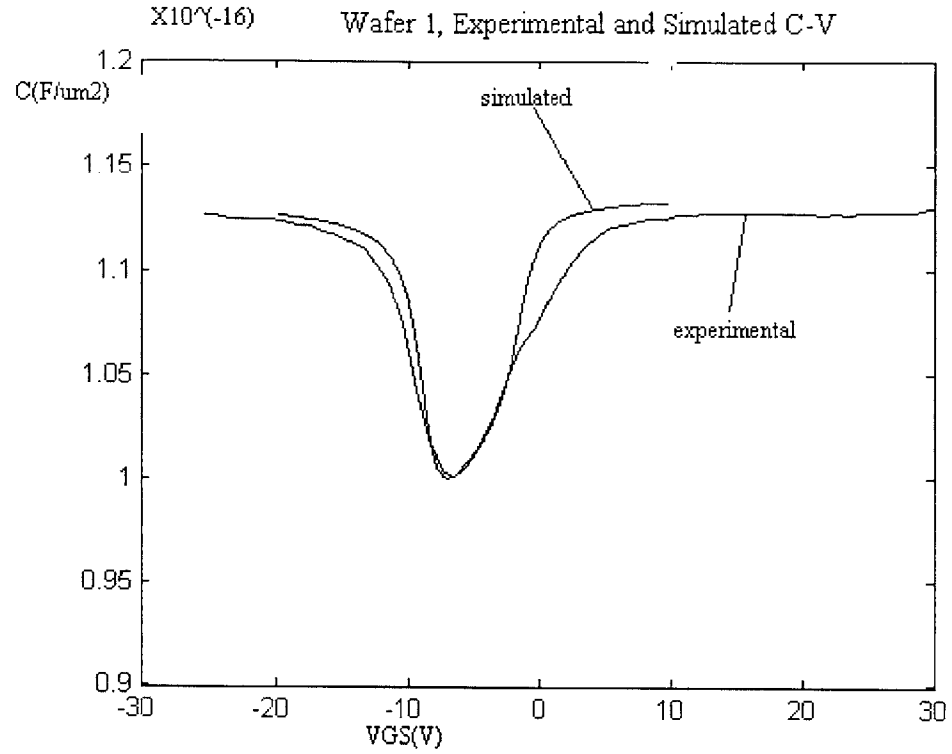
X10^(-16)
Wafer 1, Experimental and Simulated C-V
C(F/um2)
1.2
1.15
1.1
1.05
1
0.95
0.9
simulated
experimental
-30
-20
-10
0
10
20
30
VGS(V)

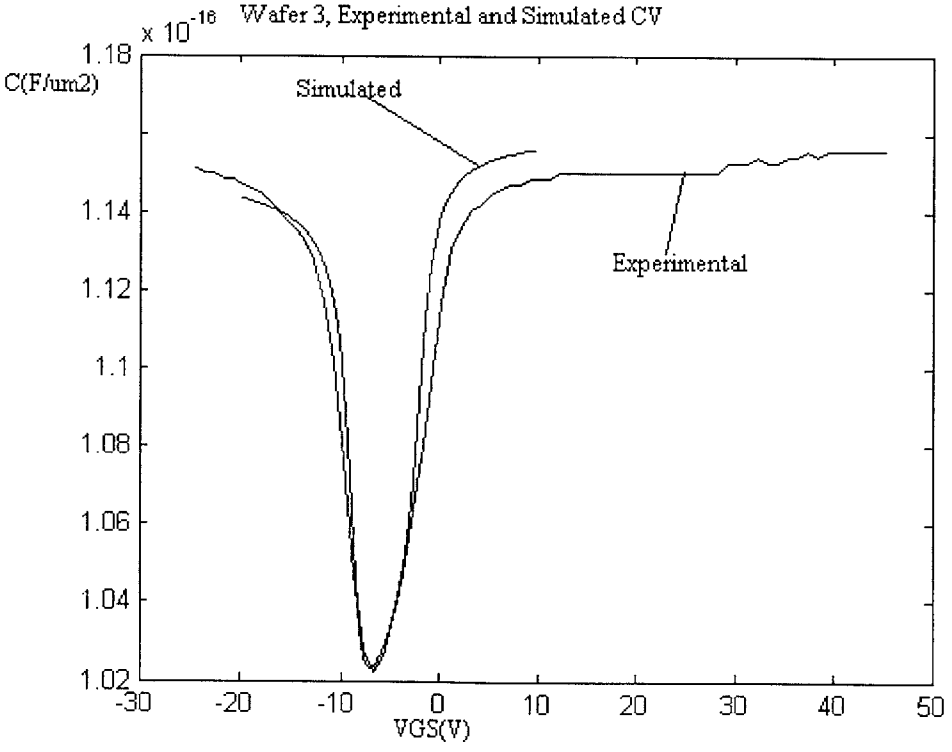
x 10^-16
Wafer 3, Experimental and Simulated CV
C(F/um2)
1.18
1.14
1.12
1.1
1.08
1.06
1.04
1.02
Simulated
Experimental
-30
-20
-10
0
10
20
30
40
50
VGS(V)

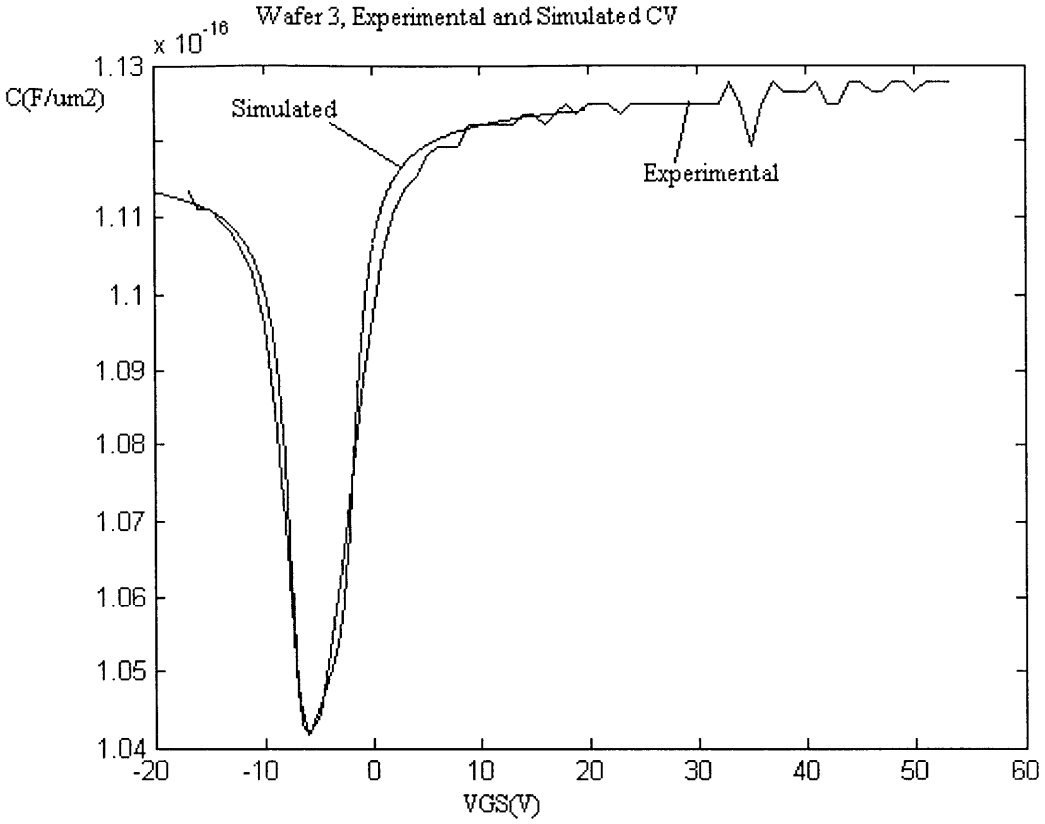
Wafer 3, Experimental and Simulated CV
x 10^-16
C(F/um2)
1.13
1.11
1.1
1.09
1.08
1.07
1.06
1.05
1.04
Simulated
Experimental
-20
-10
0
10
20
30
40
50
60
VGS(V)